AUTOMATIC TUNING OF SILICON PHOTONICS MILLIMETER-WAVE TRANSCEIVERS BUILDING BLOCKS

A Dissertation

by

GIHOON CHOO

Submitted to the Office of Graduate and Professional Studies of
Texas A&M University
in partial fulfillment of the requirements for the degree of

DOCTOR OF PHILOSOPHY

Chair of Committee,	Kamran Entesari
Committee Members,	Samuel Palermo
	Christi. K. Madsen
	Gerard Coté
Head of Department,	Miroslav M. Begovic

August 2018

Major Subject: Electrical Engineering

ABSTRACT

Today, continuosly growing wireless traffic have guided the progress in the wireless communication systems. Now, evolution towards next generation (5G) wireless communication systems are actively researched to accomodate expanding future data traffic. As one of the most promising candidates, integrating photonic devices in to the existing wireless system is considered to improve the performance of the systems. Emerging silicon photonic integrated circuits lead this integration more practically, and open new possibilities to the future communication systems.

In this dissertation, the development of the electrical wireless communication systems are briefly explained. Also, development of the microwave photonics and silicon photonics are describied to undearstand the possibility of the hybrid SiP integrated wireless communication systems. A limitation of the current electrical wireless systems are addressed, and hybrid integrated mm-wave silicon photonic receiver, and silicon photonic beamforming transmitter are proposed and analysed in system level.

In the proposed mm-wave silicon photonic receiver has 4th order pole-zero silicon photonic filter in the system. Photonic devices are vulnerable to the process and temperature variations. It requires manual calibration, which is expensive, time consuming, and prone to human errors. Therefore, precise automatic calibration solution with modified silicon photonic filter structure is proposed and demonstrated. This dissertaion demonstrates fully automatic tuning of silicon photonic all-pass filter (APF)-based pole/zero filters using a monitor-based tuning method that calibrates the initial response by controlling each pole and zero individually via micro-heaters. The proposed tuning approach calibrates severely degraded initial responses to the designed elliptic filter shapes and allows for automatic bandwidth and center frequency reconfiguration of these filters. This algorithm is demonstrated on 2nd- and 4th-order filters fabricated in a standard silicon photonics foundry process. After the initial calibration, only 300ms is required to reconfigure a filter to a different center frequency. Thermal crosstalk between the micro-heaters is investigated, with substrate thinning demonstrated to suppress this effect and reduce filter calibration to less

than half of the original thick substrate times. This fully automatic tuning approach opens the possibility of employing silicon photonic filters in real communication systems.

Also, in the proposed beamforming transmitter, true-time delay ring resonator based 1x4 beamforming network is embeded. A proposed monitor-based tuning method compensates fabrication variations and thermal crosstalk by controlling micro-heaters individually using electrical monitors. The proposed tuning approach successfully demonstrated calibration of OBFN from severely degrated initial responses to well-defined group delay response required for the targeted radiating angle with a range of 60°(-30° to 30°) in a linear beamforming antenna array. This algorithm is demonstrated on OBFN fabricatd in a standard silicon photonicsfoundry process. The calibrated OBFN operates at 30GHz and provide 2GHz bandwidth. This fully automatic tuning approach opens the possibility of employing silicon OBFN in real wideband mm-wave wireless communication systems by providing robust operating solutions.

All the proposed photonic circuits are implemented using the standard silicon photonic technologies, and resulted in several publications in IEEE/OSA Journals and Conferences.

DEDICATION

To my loving creator, without his love and protection, I can do nothing.

ACKNOWLEDGMENTS

First of all, I deeply appreciate my advisor, Dr.Kamran Entesari, for his endless advice, insight,and support. He guided me to approach a technical problem from various angles, encouraged me to voyage the unexplored research area, and gave me numerous opportunities to work with greatest minds in both academia and industry. My research would not have been possible without his vision and professional experiences. I would also like to express my gratitude to my advisory committee members: Dr. Samuel Palermo, Dr. Christi Madsen, and Dr. Gerard Coté for their constructive feedback on my research, proposal, and this final dissertation. I also thank to my colleagues at AMSC group (Texas A&M University), Shengchang Cai, Binhao Wang, Kunzhi Yu, and Ali Pourghorban Saghati. It was my great pleasure to work with you all. Finally, I would like to thank my family who has mentally, spiritually, and financially supported me during my Ph.D. program. I am very fortunate to have this lovely family in my life.

CONTRIBUTORS AND FUNDING SOURCES

Contributors

This work was supported by a dissertation committee consisting of Professor Kamran Entesari, Professor Samuel Palermo, and Professor Christi Madsen of the Department of Electrical and Computer Engineering and Professor Dr. Gerard Coté of the Department of Biomedical Engineering. Chapter III were collaborated with Shengchang Cai and Binhao Wang of the Department of Computer Science and Engineering.

All other work conducted for the dissertation was completed by the student independently.

Funding Sources

Graduate study was supported by the National Science Foundation under Grant EECS-1547432.

NOMENCLATURE

1G	First generation
2G	Second generation
3G	Third generation
4G	Fourth generation
5G	Fifth generation
APF	All-pass filter
OBFN	Optical beamforming network
HD	High definition
MIMO	Multiple-input-multiple-output
MWP	Microwave photonics
RoF	Radio-over-fibre
WDM	Wavelength-division-multiplexing
RAU	Remote antenna unit
PON	Passive optical network
OPLL	Optical phase-lock Loop
PAA	Phased array antenna
WDM	Wavelength-Division-Multiplexing
SiP	Silicon photonics
IC	Integrated circuit
SOI	Silicon-on-insulator
SiO_2	Silicon dioxide
CMOS	Complementary metalâĂŞoxideâĂŞsemiconductor

BW	Bandwidth
Q-factor	Quality factor
RF	Radio frequency
SAW	surface acoustic wave
LTCC	Low-temperature co0fired ceramic
MZM	Mach zehnder modulator
TIA	Transimpedance amplifier
DSP	Digital signal processing
BER	Bit error rate
NF	Noise figure
BB	Base band
PA	Power amplifier
LO	Local oscillator
IL	Insertion loss
IIP3	third0order intercept point
SNR	Signal to noise ratio
EVM	Error vector magnitude
QAM	Quadrature amplitude modulation
ACPR	adjacent channel power ratio
FDTD	Finite-difference time-domain
PIC	Photonic integrated circuit
MZI	Mach-Zehnder interferometer
PD	Photo-detector
RTL	Round trip loss
ORR	Optical ring resonator

ADC	Analog-to-digital converter
DAC	Digital-to-analog converter
FIR	Finite impulse response
IIR	Infinite impulse response
FSR	Free spectral range
CMP	Chemical mechanical planarization
SPI	Serial peripheral interface
OVNA	Optical vector network analyzer
CLIPP	contactless integrated photonic probe
TEC	Thermo electric cooler
μ-TEC	Micro thermo-electric cooler
TTD	True time delay
PCB	printed circuit board

TABLE OF CONTENTS

LIST OF FIGURES

LIST OF TABLES

TABLE Page

1. INTRODUCTION

1.1 Wireless communications

The past few decades have shown a great advancement in wireless communication systems. Also, this technology-driven development of the communication systems has influenced the lives of the people dramatically. And now explosive increase in data traffic demands a further improvement of the wireless communication systems toward next-generation platforms. Looking past, wireless communication systems have followed several important paths till now [3, 4] (Fig. 1.1). Initially, wireless communication was introduced with wireless telegraph, and first speech transmission is used for the military in the early 1920s. It evolved into the car based telephone for commercial use in the 1930s. When the car-based telephone was first introduced, it only showed limited ’push-to-talk’ voice call, which is a half-duplex system. A bidirectional full-duplex system is introduced in the 1960s.

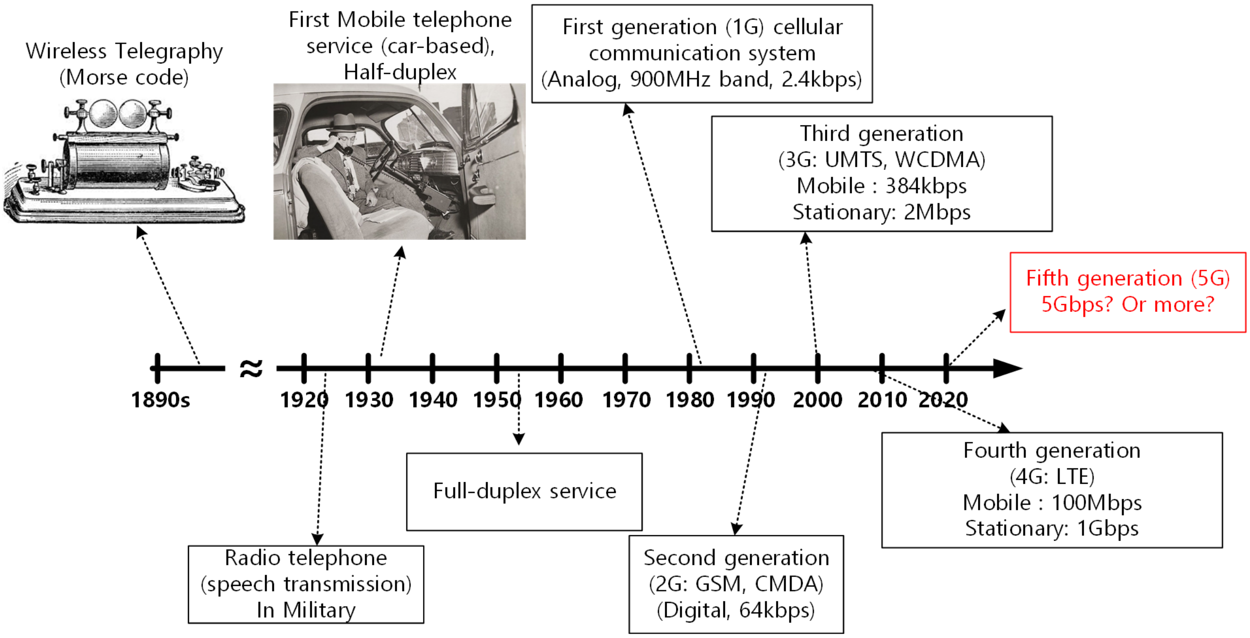

Figure 1.1: Development of wireless communication

The first-generation system, generally known as the 1G technology was introduced in the early 1980s, brought the very first cell phone. The 1G systems were based on analog systems and analog signals, which supported data bandwidth of up to 2.4kbps. This 1G technology-based services only provided analog voice services without any data services. The mobile communication systems evolved to the second-generation (2G) systems in 1991. The 2G has introduced a mobile system that was completely digital while providing capacity and coverage. The early 2G system supported data bandwidth up to 64kbps, and it supported both voice call and data transmission, such as MMS (multimedia messaging service) i.e. text messaging. The third-generation (3G) supported higher data transmission rates up to 144kbps for moving vehicles, up to 384kbps for pedestrians and up to 2Mbps for stationary users. This enabled mobile online access and multimedia applications, such as TV streaming, video conferencing, navigation, and so on. The fourth-generation (4G) provides mobile ultra-broadband internet access and also provides much faster data speed up to 1Gbps for stationary users, and up to 100Mbps for high mobility users. This wireless higher data rate access enabled high-end gaming, high definition (HD) video streaming, and high-performance imaging through the mobile communication.

Now fifth generation (5G) of the mobile technology is highly demanded to accommodate the ever-growing mobile traffic. To meet an orders-of-magnitude increase in data traffic demand, hardware-centric enabling technologies are required [5]. For example, incorporating cell sizes, increasing spectral efficiency and also acquiring mm-wave spectrum for the new wireless channel, realizing massive multiple-input-multiple-output (MIMO) at the base station, or remote antenna unit [6]. An excellent description of all the technologies required for potentially realizing a 5G network was provided in [1] and is reprinted in Fig 1.2.

Today's wireless networks are crammed on the same bands of the radio-frequency spectrum below 6GHz while increasing number of devices are consuming more data. Easy solution to solve this problem is utilizing mm-waves broadcasting at new frequencies ($30 \sim 300$GHz). mm-wave signals have one major drawback which cannot easily penetrate buildings or obstacles. This issue is being addressed with small cell concepts in 5G network. Small cells are portable miniature base

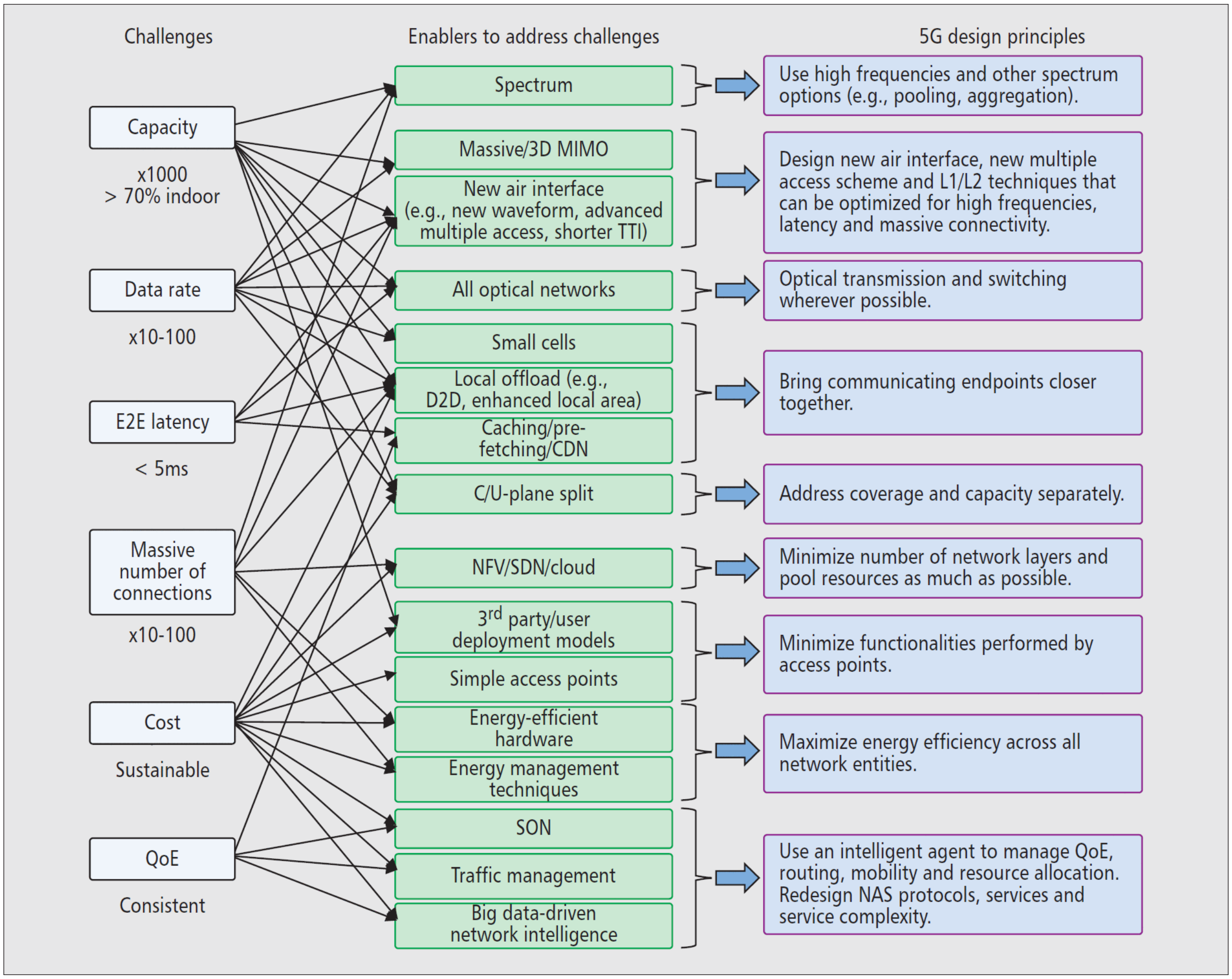

Figure 1.2: An overview of the 5G cellular networks challenges, potential enablers, and design principles [1].

stations that require minimal power to operate and can be placed every 250m or so throughout cities. Therefore, small cell principle in 5G network fit very well with the mm-wave frequencies. Also, small cells allow efficient use of spectrum. Spectrums that one station uses in one area can be reused by another station in another area [7].

MIMO describes wireless systems that use two or more transmitters and receivers to send and receive more data at once. Massive MIMO takes this concept to a new level by featuring dozens of antennas on a single array [7]. Multiple antennas at the transmitter and/or receiver can improve network throughput, capacity, and coverage without additional bandwidth or transmit power level.

MIMO is already utilized on some 4G base stations, but massive MIMO is still in development. Massive MIMO looks promising for the future of 5G, however; installing many antennas to handle cellular traffic faces more interference between those signals. Therefore beamforming, which confines signal power in a direction instead of transmitting in all directions, should be incorporated in the 5G stations.

None of these technologies is new to the community. However, implementing them in a 5G cellular network face a number of challenges to solve not only from an engineering angle but also in terms of cost.

1.2 Microwave photonics towards 5G networks

Microwave Photonics (MWP) is now a mature interdisciplinary engineering field that attempts to utilize the properties of photonic technologies to improve the performance of microwave/wireless systems, sensor networks, radar, satellite communications, instrumentation, and warfare systems [6, 8]. Research in the area of microwave photonics has been more than three decades, and many research findings are in photonic generation, photonic signal processing, control and distribution of microwave and mm-wave signals. Most of the MPW research are exploiting the inherent transmission properties of photonic technologies; low loss, large bandwidth, and immunity to electromagnetic interference) to enhance the performance of a microwave system.

As discussed earlier, small cells will play an important role in 5G networks by connecting mm-wave signals to users, enabling frequency reuse, potentially reducing energy and cost. To serve these small cell concepts in 5G networks, a backbone network implemented over a radio-over-fibre (RoF) based architecture can be an ideal solution [9]. RoF enables RF signals to be transported over fiber across kilometers with minimal loss over the links. Hence, it eases spectrum constraints, and it can replace multiple coax cables with a single fiber-optic cable. RoF also brings several advantages such as simpler RAUs (remote antenna units) since it does not require up-conversion, centralized frequency channel management, capable to support multiple wideband signals through wavelength-division multiplexing (WDM) [10]. A RoF architecture is a highly promising network solution to bridge the last-meter wireless connection with ultra-fast optical signals. Also, established fiber infrastructures are strengthening the RoF architecture as a candidate for 5G backbone network. For example, the deployment of passive optical networks (PONs) brings access points, supporting higher than Gbps, closer to end-users, and can be used as optical backhaul network for the next generation (5G) wireless broadband connections [11].

Utilizing mm-wave spectrum is essential in 5G networks to accommodate future data traffic. Conventionally, a microwave or mm-wave signal is generated using electronic circuitry with many stages of frequency doubling to achieve the desired frequency, which is complicated and costly [8]. In addition, the distribution of a generated microwave or mm-wave signal in the electrical domain is not practical due to the high loss electrical distribution lines. Whereas, broad bandwidth and low loss of the innate optical fiber properties make optical fiber as an ideal solution to distribute the signals. Therefore, the ability to generate a mm-wave signal in the optical domain is essential to utilize RoF. A mm-wave signal generation in optical domain have been studied and successfully demonstrated through numerous MWP techniques, such as optical injection locking [12, 13], optical phase-lock loop(OPLL) [14, 15, 16], microwave generation using external modulation [17, 18] and dual-wavelength laser source [19].

Massive MIMO is also a key technology in 5G networks. At mm-wave frequencies, higher path loss limits the coverage of the system therefore employing beamforming techniques to focus and steer the signal beam to the desired directions is considered as a promising solution. Instead of transmitting in all directions, antennas confine signal power in a particular direction of interest and allows effective power consumption at the transmitter. By focusing the signal beam in certain directions, the interference issue of the MIMO can be addressed. Because of their fast steering and compactness, phased array antennas (PAAs) seems to be the most attractive beam steering method in the mm-wave band. Traditionally, beamforming is realized in electronic circuits. However, electronic integrated circuits suffer from the high loss at the mm-wave signals. Also, PAAs based on phase shifters suffer from the beam-squint effect which results in frequency dependant beam-steering, and limits the bandwidth of the PAA. The emerging techniques in MWP are based on True Time Delay (TTD) and providing broadband beam steering as well as low loss properties

[20].

One of the interesting MWP areas, which can be incorporated with 5G networks is MWP filters. MWP filters are designed to perform equivalent tasks to those of conventional microwave filters, however; they show superior performance in mm-wave frequency bands due to its innate properties, such as low loss, high bandwidth, immunity to electromagnetic interference, and reconfigurability and tunability [21, 22, 20].

1.3 Silicon photonics

Silicon photonics (SiP) is the study and application of photonic systems which use silicon as an optical medium [23, 24]. Initial motivation of SiP is based on its compatibility with the mature silicon IC manufacturing. Silicon has been widely used as the substrate for most integrated circuits. Hence, silicon wafers have the lowest cost per unit area and the highest crystal quality compared to other semiconductor material. Fabricating low-cost high quality photonics by utilizing the IC fabrication infrastructure has been the major motivation for SiP research. However, it is not the only benefit for SiP. The high-quality silicon-on-insulator (SOI) wafers provide an ideal platform for planar waveguide circuits. The high index contrast between silicon and SiO_2 allows strong optical confinement and also make possible to scale photonic devices down to hundreds of nanometer level [24]. Also, silicon has excellent material properties that are important in photonic devices, such as high thermal conductivity, high optical damage threshold, and high third-order optical nonlinearities, and shows strong Kerr and Raman effect. For the last, compatibility with the silicon IC manufacturing allows monolithic integration of silicon photonic components with CMOS chips as shown in Fig. 1.3 (reprinted courtesy [2]). This opens up the new potential of photonic integration.

Based on these motivations, mainstream application of SiP has been targeted for optical interconnects for data communications [25]. Due to the large bandwidth and low loss properties of optical channels, optical interconnect technologies play an important role in scaling up the performance of various network segments that range from long-distance inter data-center connections to short-reach rack-to-rack communication and include onboard and chip-to-chip links [26].

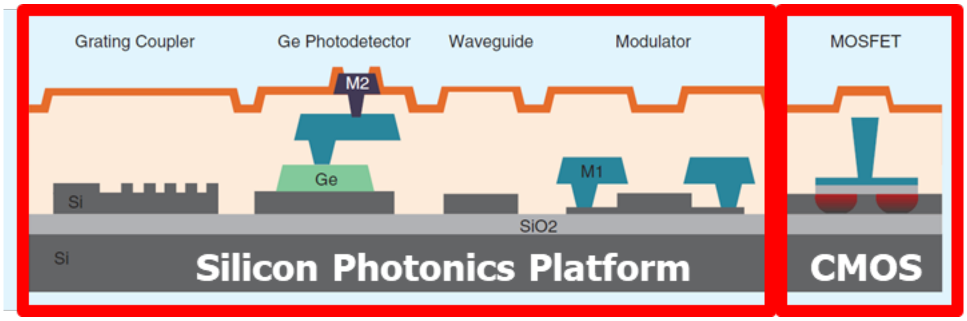

Figure 1.3: Silicon photnoic platform with photonic devices and MOSFETs on a SOI wafer. (reprinted courtesy [2]).

Not only the optical interconnects, silicon photonics is a promising technology for MWP. Increasing demands for 5G network solution, MWP is one of the promising candidates for the 5G networks. However, traditional MWP are suffering from reliability, cost, and power consumption issue even though its prominent functionalities over a large bandwidth. With silicon photonics, one can achieve a reliability, reduction in footprint, inter-element coupling losses, packaging cost as well as power dissipation [27]. And some of silicon photonic MPW application will be introduced in this work.

2. SILICON PHOTONIC INTEGRATED MM-WAVE SYSTEM

2.1 Silicon Photonic Receiver

Wideband mm-wave multifunction receivers (f >30GHz) that can cover a broad spectral range, be rapidly reconfigured, and supporting high frequencies are essential for a variety of applications, including wireless communications, radar, and sensing systems. However, ensuring robust operation in mm-wave wireless environments targeting 5G applications is challenging. A potential solution is to employ photonic devices into the conventional system, provided that high quality factor (Q) filters capable of highspeed reconfiguration and operation at mm-wave frequencies can be realized. While this is not feasible with conventional electronic filter technology, RF photonic technology has the potential to enable widely tunable mm-wave receivers which possess both wide instantaneous bandwidth (BW) 5GHz over a broad spectral range (f >30 GHz) [28]. Rapid dynamic filter reconfiguration (sub-ms) and blocker cancellation (-10dBm) with 40dB out-of-band rejection will be essential to effectively utilize a wideband spectrum [29]. Utilizing the innovative optical filter and CMOS circuit techniques discussed in this work will enable the efficient use of RF silicon photonic band-pass filters to fulfill these requirements.

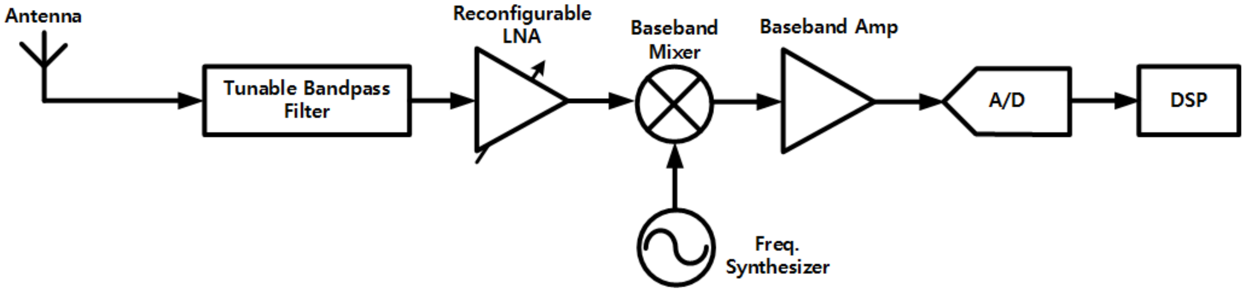

Figure 2.1: Wideband multi-function mm-wave receiver block diagram (f>30Ghz)

2.1.1 Electrical mm-wave receiver limitations

There are fundamental limitations to achieving the required level of frequency selectivity and tuning range and speed with conventional active or passive electrical filters within the size, weight, and power targets of radio systems with small form factors at mm-wave frequencies. Off-chip surface acoustic wave (SAW) filters have been widely adopted at the front end of many receivers in harsh RF environments [30]. However, in multi-band or highly-dynamic RF environments, a complex high-speed tunable filter is required which is not feasible with existing SAW filters. Other technologies, such as off-chip MEMS or low-temperature co-fired ceramic (LTCC) filters [31, 32], due to a limited Q-factor, are expected to have limited rejection for strong close-in jammers.

Existing on-chip or integrated front-end filtering solutions can be categorized into high frequency integrated RF/analog tunable filters [33, 34], and SAW-less reconfigurable front-ends. Currently, highfrequency integrated analog filters cannot achieve the high selectivity and wide tuning requirements necessary for tunable receivers with wide instantaneous bandwidth due to low/moderate on-chip inductor Q-factors. Also, due to the active nature of these filters, their linearity is limited. SAW-less receivers have gained attention for single/multi-band wireless systems to mitigate SAW filters by proving dynamic bandpass filtering based on a reciprocal passive mixing technique, but it is extremely difficult to push their frequency of operation into the mm-wave range, as they need a clock with a frequency at least 4X higher than the desired radio frequency [30, 35, 36]. Table. 2.1 shows out-of-band blocker rejection and input frequency range of recently reported CMOS SAW-less receivers. As can be seen, blocker rejection and frequency range are limited for wide instantaneous bandwidth receivers.

	[30]	[35]	[37]	[36]	[38]
Rejection [dB]	<20	<21	<20	<24	<15
Input RF signal [GHz]	0.9	1.96	0.4-0.9	0.9	2.4
CMOS technology [nm]	65	65	90	65	90

Table 2.1: Rejection and input RF signal frequency range of SAW-less CMOS receivers.

These limitations of electrical filters motivates the employment of RF photonic band-pass and notch filters, which can achieve higher Q, multi-GHz tuning ranges, and, with the innovative tuning schemes proposed in this work, sub-ms reconfiguration times. While RF photonic filters have traditionally been demonstrated with bulky, discrete optical test-bench implementations using array waveguide gratings, optical fiber Bragg gratings, and fiber Fabry-Perot filters [39], the emergence of silicon photonics has enabled the potential for these RF photonic filters to be implemented in the size, weight, and power requirements of radio systems with small form factors [40, 41]. Because of significant loss reduction and high waveguide refraction index, 200,000 Q factors and high integration density is achievable [42].

2.1.2 System Design

The targeted system is silicon photonic mm-wave receiver for 5G communications that utilizes high-performance band-pass photonic filtering. The photonic receiver is implemented in a 130nm SOI optical chip that is intelligently controlled by a 65nm CMOS chip to allow for automatic calibration and tuning of both photonic band-pass and notch filters with very high accuracy. Fig. 2.2 shows the system driver of hybrid integrated RF-photonic receiver, consisting of the two main parts.

Variable	Definition or Value [unit]
Laser Source Power ($P_{opt,in}$)	19.2 [dBm]
Coupler Loss (L_c)	0.4 [dB]
Detector Responsivity(R_{PD})	0.75 [A/W]
MZM Insertion Loss (L_{MZM})	6.5 [dB]
MZM V_π	3.1 [V]
MZM Bias Voltage (V_{bias})	$V_{pi}/2$ [V]
RF Input Power	-20 [dBm]
Temperature	293 [K]
Optical Wavelength	1550n [nm]
Modulator Input Load	50 [Ω]
TIA Input Impedance	200 [Ω]

Table 2.2: mm-Wave Silicon Photonic RX Parameters

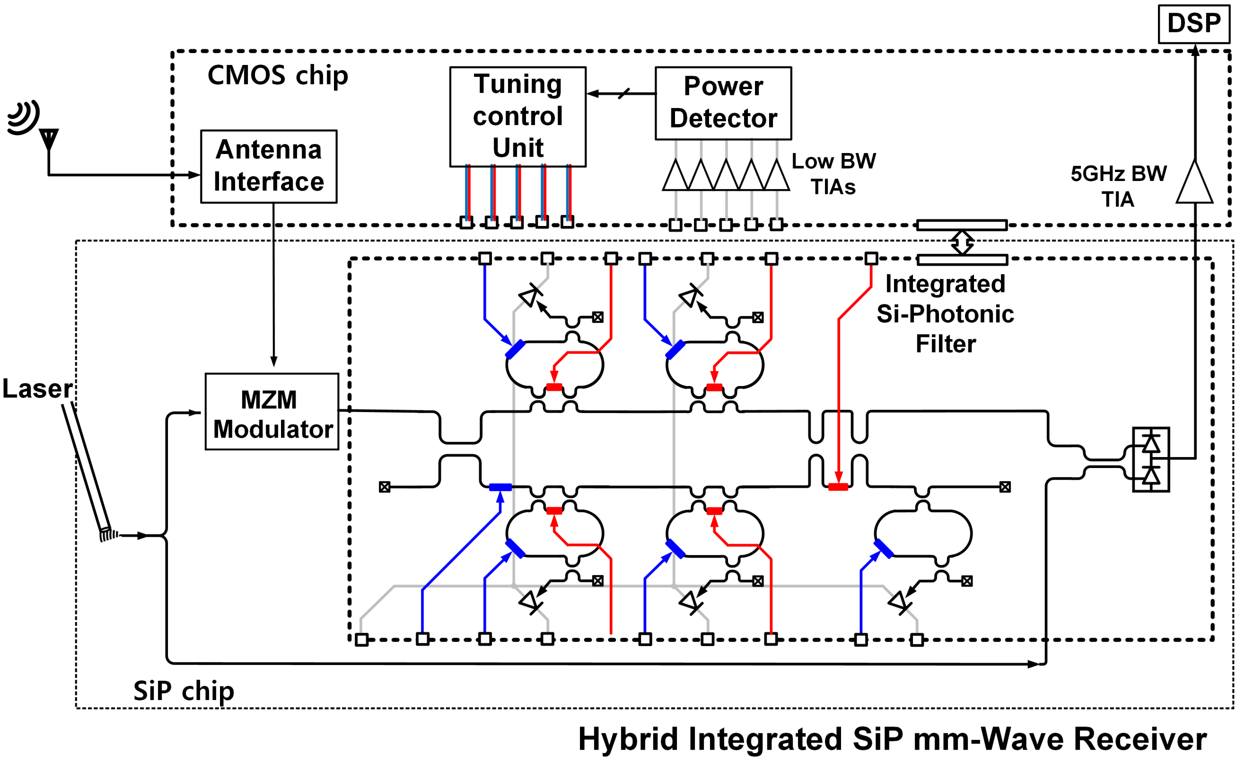

Figure 2.2: Hybrid integrated silicon photonic RF front-end.

The CMOS chip includes the antenna interface, MZM pre-distortion linearization stage, optical RF front-end (TIA), as well as the electrical circuitry for tuning the filter responses. The SOI SiP chip includes MZMs for E-O conversion, a 5GHz reconfigurable channel-select 4th-order BPF, and waveguide photodetectors for O-E down-conversion and filter monitoring. An external wideband frequency synthesizer is utilized for generation of different stimuli used in the calibration of the photonic filters. After O-E conversion by an adaptive bandwidth TIA, an external DSP module detects and de-spreads the 0-5GHz baseband spread spectrum signal to measure the system BER.

The system model of the mm-wave receiver has been constructed in order to quantify the key system parameters which are summarized in Table. 2.2. Key silicon photonic device data is taken from the IME foundry information, to estimate a 22.37dBm third order intermodulation point power (P_{IIP3}), 7.4dB noise figure (NF). An eq.(2.1) is used to estimate the signal power gain.

$$
\begin{aligned}
P_{rx,out} = 10log_{10}(\frac{\pi V_{rf}}{2V_{\pi}}) + 10log_{10}(R_{TIA}) + 20log_{10}(R_{pd}) \\
+P_{opt,input} - L_{filter,4th} - L_{grating} - 2 \times L_c
\end{aligned}
\tag{2.1}
$$

2.2 Silicon Photonic Beamforming Transmitter

Beamforming with wideband instantaneous bandwidth and high-resolution is essential for many applications including fifth-generation (5G) wireless communications with carrier frequency of 30 GHz and multi-Gbps data rates requiring multi-GHz instantaneous beamforming bandwidth [43, 44, 45, 46, 47, 48], and radar and satellite communications such as airborne satellite radios providing in-flight connectivity for flight crew information and wideband streaming of live TV and high-speed internet for the passengers with beam angles as low as 2 degrees [49, 50, 10]. Fig. 2.3 shows the block diagram of a mm-wave beamforming transmitter array including the up-converter to transfer the baseband (BB) signal to mm-wave range (f > 20 GHz), beamforming network to generate the required delay for each path to direct the radiated beam in a particular angle, and a mm-wave power amplifiers (PA) and antenna for each signal path. A potential solution is to employ wideband mm-wave PAs and antennas along with wideband, high resolution mm-wave beamforming networks. While it is extremely challenging with conventional electronic beamforming network technology, RF photonics technology has the potential to provide mm-wave beamforming transmitters with wide instantaneous bandwidth ($\sim$ 5 GHz) with high beam steering resolution (< 2 ° Utilizing the photonic beamforming network and CMOS electronics discussed in this proposal will allow the use of RF silicon photonics delay units to fulfill these requirements.

2.2.1 Electrical mm-wave beamforming transmitter limitaions

There are significant limitations to achieve the required instantaneous bandwidth and beam steering accuracy at mm-wave frequencies with conventional electronic beam forming arrays. Electronic beamforming can be performed in either the RF, LO or BB path [51, 52, 53, 54, 55, 56, 57]. RF beamforming is the most widespread method since it provides RF spatial filtering and it has less power consumption compared to two other approaches [51, 52, 53, 54, 55]. RF beam-

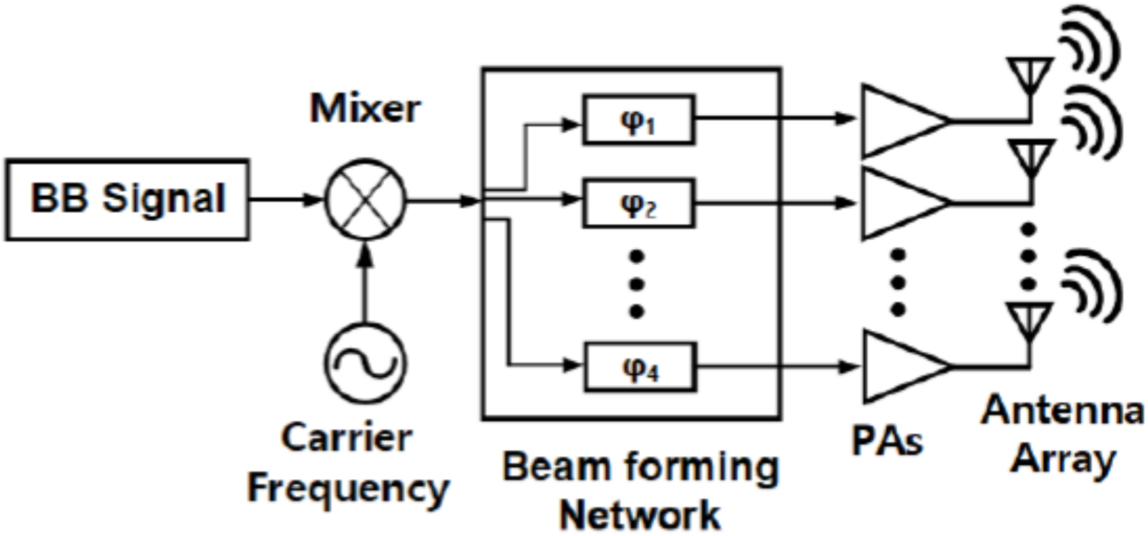

Figure 2.3: Blcok diagram of a beamforming mm-wave transmitter array.

forming is either performed using phased arrays or timed arrays [51, 52, 53, 54] Phased arrays employ phase shifters in their RF path mostly for wireless communications applications. They have several major drawbacks. They are inherently narrowband, therefore, beam radiation angle is dependent on the RF wavelength (Beam squint effect) and the robust ones have discrete phase tuning states with limited phase resolution (> 5.6 °). Passive phase shifters consume a small amount of power and are highly linear, but they are very lossy (IL > 5 dB), while active ones can have gain but their linearity is limited and they consume larger amount of power. They can be easily integrated using CMOS process with a small footprint. Timed arrays, on the other hand, employ delay units in their RF path to provide larger instantaneous bandwidth at RF frequencies mostly for ranging applications [55], so they do not suffer from beam squint effect, but they also have some drawbacks. Their robust delay units have discrete tuning states with limited resolution, also they are bulky and their integration into CMOS process is challenging, especially if high delay resolution is required. They typically include active components which increase their power consumption and limits their linearity. Therefore, realization of mm-wave beamforming arrays with large instantaneous bandwidth, high beam steering resolution and small foot-print for integration is extremely challenging using conventional electronic solutions.

These limitation of electrical timed/phased array at mm-wave motivates the employment of RF-photonic delay units that can achieve simultaneous wide bandwidth, and high beam steering resolution. While delay-based RF photonic beamformers have traditionally been realized using discrete optical test bench implementations such as Fourier optics [58], dispersive fibers [58], fiber gratings [59, 60], and switchable delay matrices [61], the emerging of silicon photonics has enabled the potential for these RF photonic delay units to be realized in the size, weight and power consumption of radio systems with small form factors [27, 50].

Major drawbacks of the reported silicon RF beamforming network include the difficulty of calibration due to fabrication and temperature variations and adjustment of the beamforming network with high accuracy for the precise beam steering. Since phased arrays with acceptable directivity at mm-wave are at least 8-element or larger, a significant number of photonic phase shifters inside the beamforming network structure need to be very precisely tuned to provide the desired group delay at the band of interest [27, 50]. A common procedure is to visually monitor the filter response using a spectrum analyzer and manually tune each phase shifter via trial-and-error to achieve the desired response. This is very time consuming, requires expensive lab equipment, and is also subject to human error for the required large number of array elements. All these issues demand a more elegant way of adjusting the beamforming network within the silicon photonic mm-wave transmitter.

2.2.2 System Design

Proposed system in this work is chip-scale wideband silicon photonic mm-wave beamforming transmitter array for applications such as 5G wireless communications and airborne satellite radios utilizing high-performance photonic beamforming network for array operation. The photonic transmitter is implemented in a SOI optical chip that is intelligently controlled by a CMOS chip to allow for automatic calibration and tuning of beamforming network with very high accuracy. Figure 2 shows the system driver hybrid mm-wave transmitter, consisting of the three main parts; the 28nm CMOS chip includes MZM pre-distortion linearization stage, optical RF front-end array

(TIAs and PAs), as well as the electrical circuitry for tuning the filter responses, the 256nm SOI silicon photonic chip includes DD-MZMs for E-O conversion, a 5GHz reconfigurable beamforming network, and waveguide photodetectors for O-E conversion and photonic monitoring, and the Rodgers duroid RT/5880 substrate including antenna array. An external wideband frequency synthesizer is utilized for generation of different stimuli used in the calibration of the beamforming network, and RF LO signal generation. After O-E conversion by ultra-wideband TIAs, wideband mm-wave PAs amplify the modulated mm-wave signal with sufficient linearity to stimulate the antenna array and transmit modulated signal to a desired direction.

Fig. 2.4 shows the proposed mm-wave transmitter array designed for wideband beam steering. Implementing the integrated beamformer in the optical domain provides many advantages to the RF system, including lower loss, larger instantaneous bandwidth, higher beam steering resolution and inherent immunity to electromagnetic interference. Note that it is very challenging to perform electrical beamforming over the proposed wideband operation range. The proposed system is capable of transmitting 5GHz modulated signal at 30GHz carrier frequency. A 16-QAM modulated signal is generated externally and used as the baseband input. This modulated signal is up-converted to the C-band (1550nm) optical carrier with a DD-MZM. Since MZM follows the cosine characteristic, MZM linearization circuits are implemented to linearize the optical modulation. An 8-element beam forming network splits the signal to each branch, and applies broadband group delays over the 5GHz range and also, equalizes the optical output power at each branch for the desired beamforming. Both O-E conversion and down-conversion to RF carrier frequency (30GHz) are achieved with a waveguide photodetector (PD) connected with a micro bump (μ-bump), to a high-sensitivity/bandwidth TIA through flip-chip bonding. Output of TIAs are amplified further with wideband PAs to stimulate the antenna array. A preliminary system model of the proposed transmitter has been constructed with Simulink modeling in order to quantify the key system parameters of a single transmitter branch in the array, which are summarized in Table. 2.3. Key mm-wave system data taken from the papers for 5G applications [62], and silicon photonic device data tape-outs through the IME foundry, is utilized to estimate the required RF output power, laser

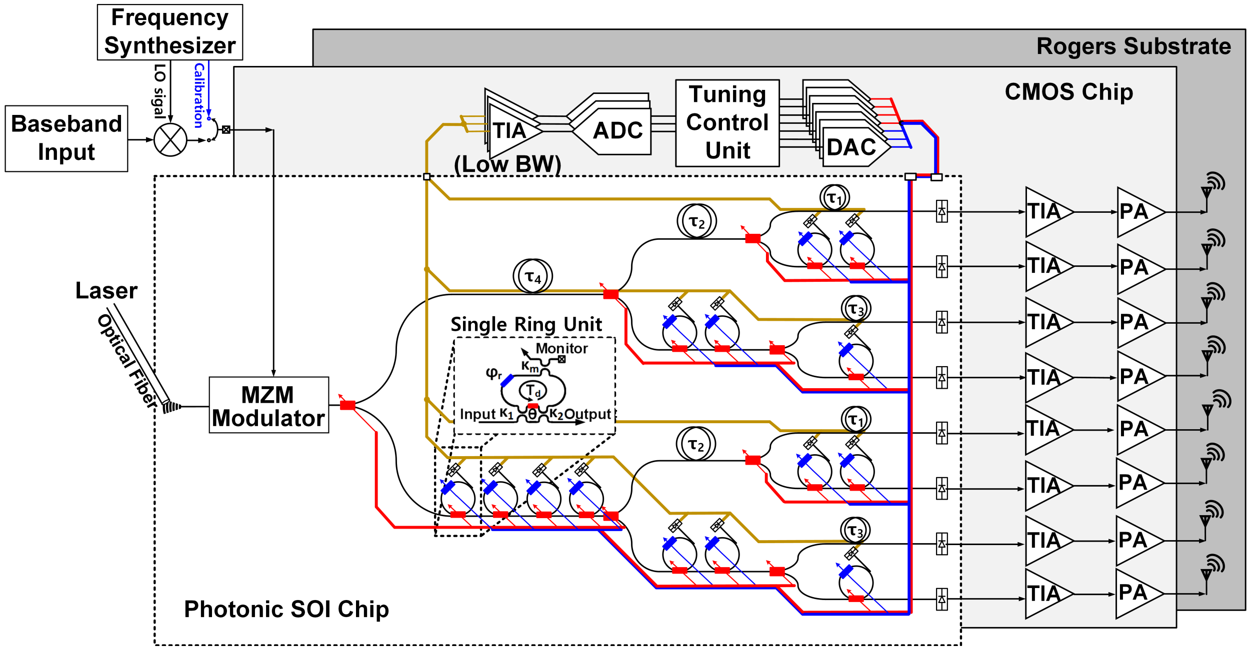

Figure 2.4: Hybrid integrated silicon photonic mm-wave transmitter.

power, and PA third-order intercept point (IIP3). The proposed mm-wave photonic transmitter is designed to operate with a 5 GHz 16-QAM modulated signal (10 GBPs), and 40m link range. In order to achieve reliable detection at the receiver side, the total RF output power ($P_{Tx,rf}(fc)$) of the transmit array in dBm is estimated by to be 10.8 dBm using eq. (2.2) and information provided in Table. 2.3. Also, the required laser power to satisfy the estimated RF output power is found to be 12.7 dBm using the link budget calculation including the O-E modulation, optical loss, E-O conversion, and electrical gain for the proposed hybrid system using eq. (2.3).

$$\begin{aligned} P_{Tx,rf}(f_c) = 10log_{10}(kT \times 10^3 \times BW_{sig}) + NF_{sig} + SNR_{sig} + L_{path}(f_c) + L_{misc} \\ + L_{fe,Tx}(f_c) + L_{fe,Rx}(f_c) - G_{array,Tx}(f_c) + G_{array,Rx}(f_c)) \end{aligned} \tag{2.2}$$

$$\begin{aligned}P_{Tx,out} = G_{PA} - 10log_{10}(R_{TIA}) - L_{MZM} - L_{beamforming} - L_{grating} - L_{misc} \\ +20log_{10}(R_{PD} \cdot \pi \cdot \frac{V_{rf}}{2V_{\pi}} + P_{opt} + L_{fe,Tx}(f_c) + L_{fe,Rx}(f_c) \\ -G_{array,Tx}(f_c) + G_{array,Rx}(f_c)\end{aligned} \tag{2.3}$$

Variable	Definition or Value [unit]
SNR_{sig} (16-QAM)	SNR at digital Rx output for 10^{-3} BER = 18 [dB]
EVM_{req}	$-(SNR_{sig} + 3dB)$
BW_{sig}	5 [GHz] (16-QAM RF bandwidth)
D	40 [m]
$\alpha_{atm}(f_c)$	0.0002 [dB/m]
$\lambda_{eff}(f_c)$	$\lambda_0\sqrt{\varepsilon_e}$
$L_{path}(f_c)$	$10log_{10}\lvert(4\pi Df_c/c_0)^2\rvert + \alpha_{atm}(f_c) \times D$ [dB]
G_{array}	$10log_{10}(N_x \times N_y) + G_{elem}$ [dBi])
G_{elem}	4.5 [dBi]
$N_{X,Y}$	$floor[d_{x,y} - 1.2\lambda_{eff}(f_c)]/[0.5\lambda_0(f_c)]$
$d_{x,y}$	43.6 × 12.5 $[mm^2]$
NF_{Rx}	8 [dB]
$L_{feed}(f_c)$	1.9 [dB]
L_{misc}	15 [dB]
$P_{Tx,rf}(f_c)$	10.8 [dBm]
PA_{IIP3}	5 [dBm]
EVM_{sim}	-21.5 [dB]
$ACPR$	-26.82 [dBc]
G_{PA}	15 [dB] (Assumed)
R_{TIA}	200 [Ω] (∼ 23.4 [dB])
$L_{MZM,grating}$	5 [Ω]
L_{OBFN}	9.2 [Ω]
L_{misc}	2.5 $[dB]$
R_{PD}	0.75 [A/W]
$MZM_{V[pi]}$	2 [V]
MZM_{IIP3}	23 [dBm]
λ_{opt}	1550 [nm]
P_{opt}	12.7 [dBm]

Table 2.3: Summary of system specifications and variable definitions and variable definitions

System-level simulations are performed to demonstrate the capabilities of the proposed single-path mm-wave photonic transmitter architecture. The simulated transmitter output constellation for 16-QAM modulation is illustrated in Figure 3 showing an EVM of -21.5 dBm, which satisfies required transmitter EVM (SNRsig+3dB margin) for the assumed operation environment. To satisfy this value of EVM, the PA requires an IIP3 of at least + 5 dBm. Also, the output spectrum of the transmitter in Fig. 2.5, shows the high selectivity to the adjacent channel and shows adjacent channel power ratio (ACPR) of 26.82 dBc.

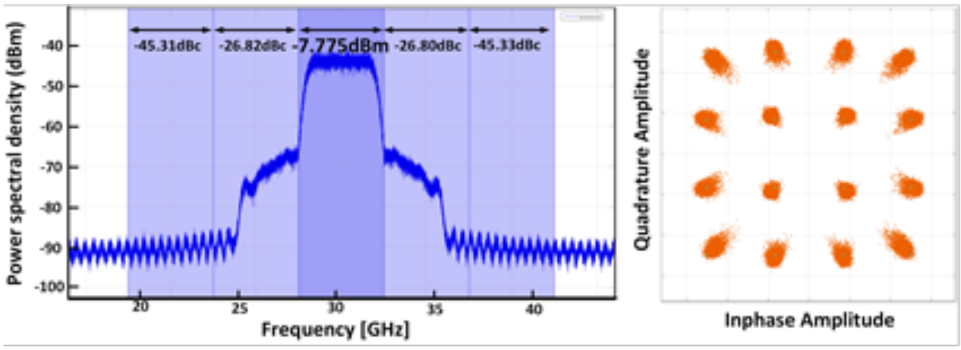

Figure 2.5: System simulation results for output spectrum, adjacent channel power ratio (ACPR), and constellation (16-QAM) with EVM < -21.5 dB

3. RING RESONATOR BASED OPTICAL CIRCUIT DESIGN

3.1 Fundamentals of optical circuits

Silicon photonic circuits are consist of various optical components. In this chapter, major components for building silicon photonic filter and OBFN are introduced. Also, the procedure of the photonic circuit design is addressed in the last section.

3.1.1 Waveguides

There are three types of commonly used rectangular waveguide structures compatible with SiP; raised strip waveguide, strip waveguide, and rib (ridge) waveguide (Fig. 3.1) [63]. The raised strip waveguide has the high index core (Si) on the substrate (SiO_2), and cladding can be formed by air or another dielectric material which has lower dielectric constant than that of the core. The strip waveguide has the core (Si) completely surrounded by a cladding (SiO_2). Generally, 0.5um (width) X 220nm (height) core slab waveguide is used for the single mode waveguide in SiP standard. For the last, rib waveguide has the core (Si) consists of the strip and thin slab (90nm) on the substrate, and cladding(SiO_2) covers the core. Strip waveguides show small bending radius and require simpler fabrication steps however, rib waveguides show lower propagation loss, coupling losses. In photonic filter and OBFN design, rib waveguide is used for the better SiP chip performance. In our measurement fabricated rib waveguide through IME showed 0.4dB/cm.

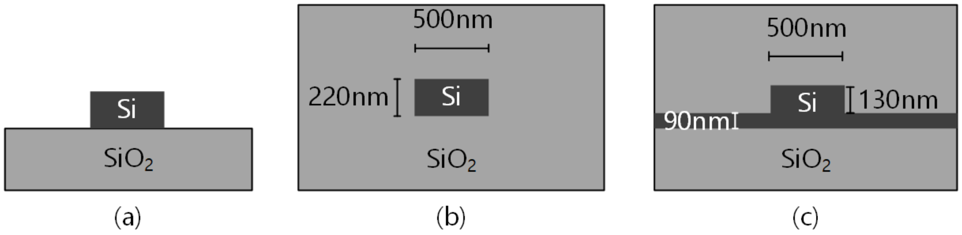

Figure 3.1: Rectangular waveguide structures. (a) raised strip waveguide, (b) strip waveguide, and (c) rib (ridge) waveguide.

Losses in the waveguides are originated from several factors. When the sidewall of the waveguide is rough, it introduces reflections and phase perturbations along the waveguide and it exacerbates the sidewall scattering. If there is a defect in the core, due to the doping, it also induces a loss in the waveguide. Also, metal near the waveguide can absorb the propagating light. And for the last, rounding of the waveguide also induces loss that radius of the rounding should be kept large enough (>25μm). Power intensity attenuation of the light in the waveguide can be described by eq. (3.1).

$$I(z) = I_0 e^{(-\alpha_{prop} z + \alpha_{misc})} \tag{3.1}$$

Since loss is one of the most important factors in SiP chip performance, these factors should be considered carefully in SiP chip design.

3.1.2 Couplers

Couplers are fundamental components for optical circuit design. A directional coupler, tunable MZI couplers will be treated briefly in this section.

3.1.2.1 Directional couplers

A directional coupler has a simple structure which has two waveguides in close. When the waveguides are placed close, evanescent field of one waveguide and the core of the other waveguide overlaps and it results in coupling between two waveguides. The coupling coefficient depends exponentially on the waveguide spacing between two waveguides because the evanescent field tails decrease exponentially. Directional couplers can have two configurations as shown in Fig. 3.2; asymmetric (one straight waveguide and one curved waveguide) or symmetric (symmetrically curved two waveguides) directional coupler. A symmetric directional coupler have shorter transition region at the beginning and end of the coupling region. Also, symmetric design shows more uniform loss characteristic at the different port of the coupler. Therefore symmetric directional couplers are used for PIC design in this work. To determine the coupling length of the directional coupler for the desired coupling ratio, Lumerical FDTD simulation is performed (Fig. 3.3) and

$L_{coupling} = 3.2\mu m$ for 50% coupler, and $L_{coupling} = 28.2\mu m$ for 5% coupler is used.

(a) (b)

Figure 3.2: Directional coupler configurations. an (a) asymmetric, and a (b) symmetric directional coupler.

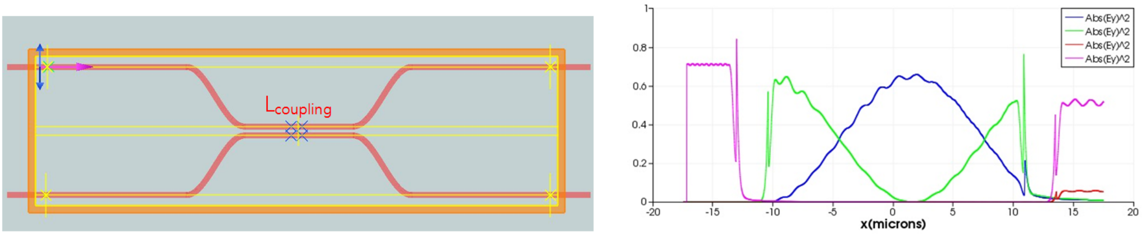

(a) (b)

Figure 3.3: Simulated directional coupler with Lumerical FDTD. (a) Simulation setup, and (b) coupling length ($L_{coupling}$) vs coupling ratio (κ) for 200nm gap (L_{gap}) directional coupler.

PIC components can be described in terms of the Z-transform [63]. PICs are assumed to be linear and time-invariant. The basic directional coupler is described in Z-transforms using waveguide delays and splitting and combining the signals. A power coupling ratio, κ is associated with each directional coupler. A directional coupler has two input/output ports. For an input on one port, the power coupled to the cross-port is κ times the input power. The length of the region where the waveguides are coupled determines the coupling ratio. And the relationships are expressed in terms of the fields as a 2×2 transfer matrix, $\Phi_{cplr}(\kappa)$ as shown in eq. (3.2).

$$\begin{bmatrix} E_{output1} \\ E_{output2} \end{bmatrix} = \begin{bmatrix} c & -js \\ -js & c \end{bmatrix} \begin{bmatrix} E_{input1} \\ E_{input2} \end{bmatrix} = \Phi_{cprl}(\kappa) \begin{bmatrix} E_{input1} \\ E_{input2} \end{bmatrix} \tag{3.2}$$

where κ is the coupling ratio, $E_{input,output}$ are coupler input and output field amplitudes, $c = \sqrt{1-\kappa}$ is through-port transmission and $-js = -j\sqrt{\kappa}$ is cross-port transmission. The transfer matrix assumes no excess loss, so the sum of the output powers equals the sum of the input powers. In addition, a directional coupler is assumed to be a narrowband operation, the coupling ratio is wavelength independent.

3.1.2.2 MZI couplers

Directional couplers' coupling ratio is highly dependent on the geometry of the directional coupler ($L_{coupling}, L_{gap}$). This results in high process variations of the directional couplers. To compensate the variations, Mach-Zehnder interferometer (MZI) is used as a tunable coupler in PIC design. This tunability also provides, reconfigurability of the PICs. The MZI coupler has two inputs and two outputs same as the directional coupler. The basic structure of MZI coupler is consist of two directional couplers in front and the end, and a phase shifter in one arm as shown in Fig. 3.4. Coupling ratios of the directional couplers (κ_1, κ_2) are 0.5 typically. The transfer matrix for the MZI can be described as eq. (3.3).

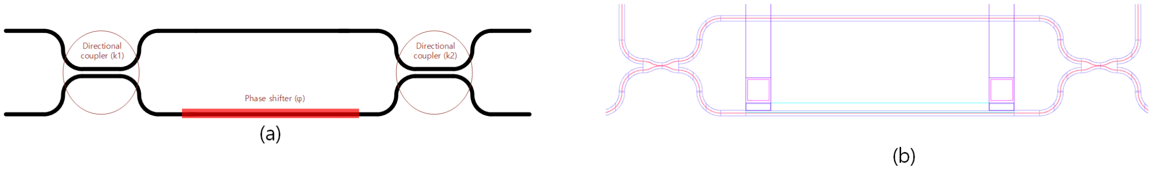

(a)

(b)

Figure 3.4: An MZI coupler (a) schematic, and (b) layout.

$$\begin{aligned}\begin{bmatrix} E_{output1} \\ E_{output2} \end{bmatrix} &= \gamma \begin{bmatrix} c_2 & -js_2 \\ -js_2 & c_2 \end{bmatrix} \begin{bmatrix} 1 & 0 \\ 0 & e^{-j\phi} \end{bmatrix} \begin{bmatrix} c_1 & -js_1 \\ -js_1 & c_1 \end{bmatrix} \begin{bmatrix} E_{input1} \\ E_{input2} \end{bmatrix} \\ &= \Phi_{loss}\Phi_{cprl2}(\kappa)\Phi_{phaseshifter}\Phi_{cprl1}(\kappa) \begin{bmatrix} E_{input1} \\ E_{input2} \end{bmatrix}\end{aligned} \tag{3.3}$$

Where, $\kappa_{1,2}$ = 0.5, ϕ is phase shift in MZI coupler and γ is the loss of the MZI coupler. Loss of the MZI coupler, γ follows eq (3.4).

$$-20log_{10}(\gamma) = \alpha L + Loss_{insertion} \tag{3.4}$$

Where, α is the loss in dB/cm for propagation through the wavegudide. L is the length of the waveguide in cm. Also, directional couplers typically have insertion loss of 0.4dB/each.

3.1.3 Grating coupler

Coupling light between PIC and a single-mode fiber is an important problem. The waveguide core layer is only about 220nm, whereas single-mode fiber has about $9\mu m$ diameter, so that there is a large mismatch between the waveguide mode and single-mode fiber mode. To solve this mismatch edge couplers or grating couplers are used to couple the light into the PIC. Edge couplers require accurate alignment and lensed fibers are often used to couple the light into the PIC. Also coupler should be placed at the edge, so dice and polish the chip needs to be done carefully. Whereas, grating coupler shows relatively easy coupling, and since it is vertically coupled coupler can be placed anywhere on the chip. This provides freedom on PIC design. Also, wafer-scale testing of PIC is possible with grating couplers.

The basic grating structure has a periodic rectangular grating teeth. The grating period is $\Lambda = \lambda / n_{eff}$ ($\Lambda = 630nm$ for 1550nm), where λ is light wavelength, and n_{eff} is effective refraction index. To avoid diffraction of the light, fiber is coupled at a small angle with respect to the surface normal. In Fig. 3.5 (a), the 1-D grating coupler has a long taper ($\sim 500\mu m$) to guide the light from the single-mode fiber mode to waveguide mode with the minimal loss. To reduce the taper length, focused 2-D grating coupler can be used (Fig. 3.5 (a)). However, in this work, 1-D grating coupler is used for the PIC design. The average grating coupler insertion loss at 1550nm is 4.5dB.

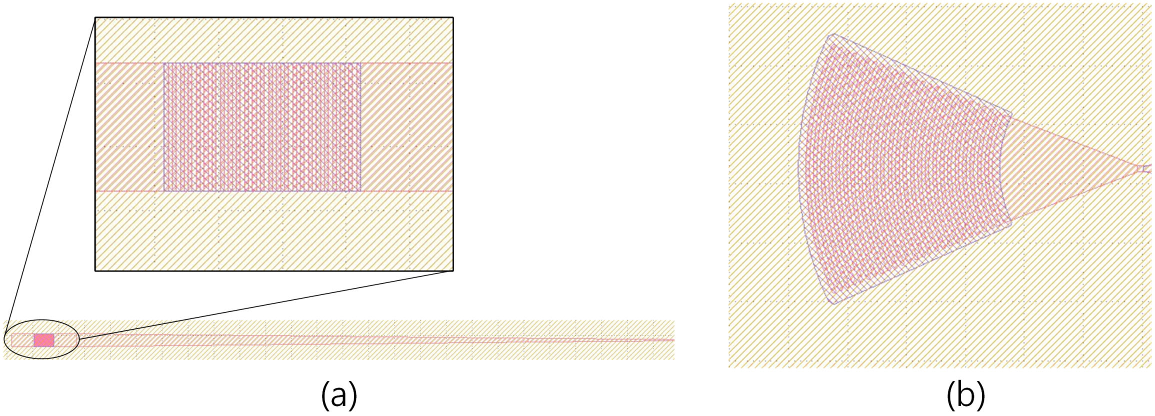

Figure 3.5: Layout of an (a) 1-D grating coupler , and a (b) 2-D focused grating coupler

3.1.4 Waveguide Ge photodiode

SiP is an excellent platform for realizing low-loss passive components due to its transparency near 1310 and 1550nm wavelength band. However, it makes hard to build sources or detectors on SiP. Therefore, it requires the integration of III/V materials or germanium(Ge) to build high speed active components. Germanium is favored in SiP due to the easy growth on silicon compared to another interface. There are design trade-offs between quantum efficiency, operating bandwidth, and output power [64]. Small PDs are preferred for the high bandwidth PDs due to their low capacitance. However, small PDs have limited absorption region, so high quantum efficiency and abrupt absorption profiles are required. For the high output power PDs, large devices with dilute absorption profiles are preferred. Most of the SiP integrated PDs have PIN diode structures. There are two common structures for a PIN waveguide PDs: Butt-coupling and vertical coupling. A butt-coupled PD has the absorbing region at the end of the input waveguide (3.6). Vertically-coupled PDs have an absorbing region on top of the waveguides. Typically butt-coupled PDs are more complex to fabricate however, they provide compact size, high efficiency, and low capacitances which is favored for high speed PDs. In this work, waveguide Ge pin PD is used for the PIC design.

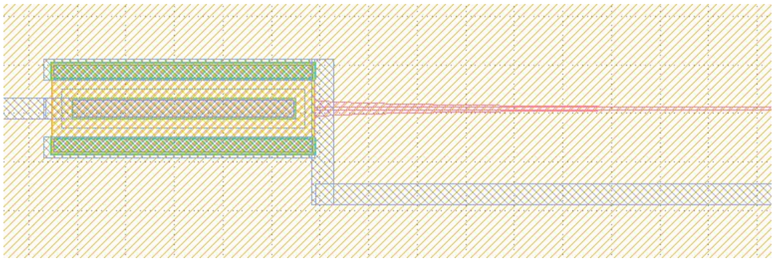

Figure 3.6: Layout of an waveguide Ge photodiode.

3.1.5 Optical Ring resonator

An optical ring resonator (ORR) is one of the simplest photonic circuits. By utilizing this basic structure, complex high-order filter [65, 66, 67, 68, 63, 40] or beamforming network [10] can be designed. In the ORR, the unit delay is the circumference of the ring. This unit delay can be expressed as z^{-1} in a transfer function of the ORR. Then basic ring resonator with one directional coupler (Fig. 3.7(a))can be described as eq. (3.5)

$$\begin{aligned} H(z) &= c - s^2(\gamma z^{-1}e^{j\phi}) + -s^2(c\gamma z^{-1}e^{j\phi})^2 + -s^2(c\gamma z^{-1}e^{j\phi})^3 + \cdots \\ &= c + \frac{-s^2\gamma z^{-1}e^{j\phi}}{(1 - c\gamma z^{-1}e^{j\phi})} = \frac{c - \gamma z^{-1}e^{j\phi}}{(1 - c\gamma z^{-1}e^{j\phi})} \end{aligned} \tag{3.5}$$

where $\gamma(= 10^{\frac{-\alpha L}{20}})$ is round trip loss (RTL), and ϕ is phase shift. The infinite sum with common term $c\gamma z^{-1}e^{j\phi}$ simplifies to the ring's transfer function. The location of the pole is determined by the coupling ratio, RTL, and phase shift. The single ORR transfer function is always stable since $c\gamma e^{-j\phi}$ is always less than unity. This simple ORR is vulnerable to the process variation that tunable MZI coupler (Fig. 3.4) is implemented to compensate it (Fig. 3.7 (b)). Then the transfer function is modified to the eq. (3.6)

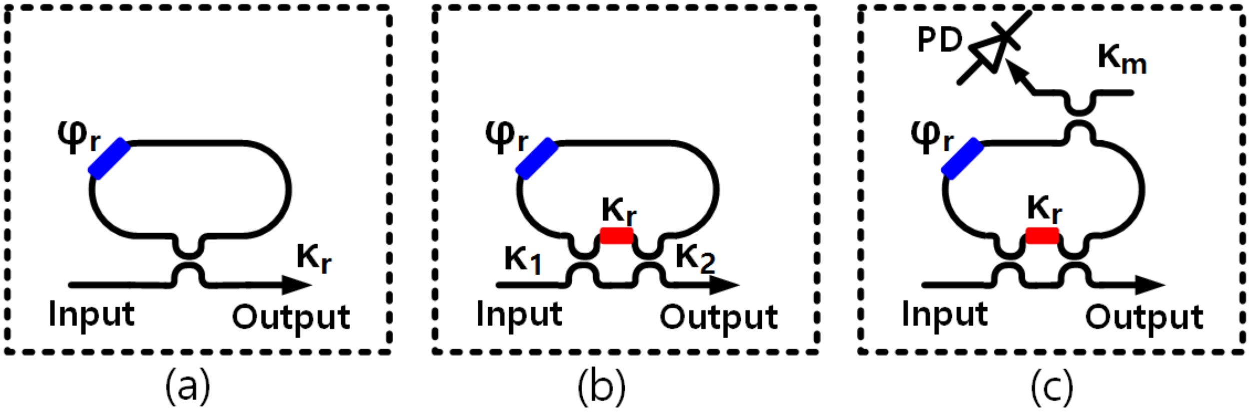

Figure 3.7: Single ORR schematics. A (a) basic ORR, an (b) ORR with MZI coupler, and an (c) ORR with MZI coupler, and drop port.

$$\begin{aligned} H(z) &= \frac{(c_1c_2 - s_1s_2e^{j\theta}) - \gamma z^{-1}e^{j(\phi+\theta)}}{1 + (s_1s_2 - c_1c_2e^{j\theta})\gamma z^{-1}e^{-j\phi}} \\ &= \frac{0.5(1 - e^{j\theta}) - \gamma z^{-1}e^{j(\phi+\theta)}}{1 + 0.5(1 - e^{j\theta})\gamma z^{-1}e^{-j\phi}} \end{aligned} \tag{3.6}$$

where $c1, s1, c2, s2$ (=$\sqrt{0.5}$ ideal) are directional coupling ratios of MZI coupler, and θ is phase shift in MZI coupler. By adding another port in the ring resonator (Fig. 3.7 (b)), the transfer function of the single ORR increases the loss by the factor of the coupling ratio of the monitor (c_m, s_m). However, the transfer function of the added port has both zero and pole as shown in eq. (3.7). In this structure, through port response and monitor response are in a complimentary relationship, and this relation will be used to place pole and zero at the desired position in Chapter. 4.

$$\begin{aligned} H_{through}(z) &= \frac{(c_1c_2 - s_1s_2e^{j\theta}) - c_m\gamma z^{-1}e^{j(\phi+\theta)}}{1 + (s_1s_2 - c_1c_2e^{j\theta})c_m\gamma z^{-1}e^{-j\phi}} \\ H_{monitor}(z) &= \frac{(s_1c_2 - c_1s_2e^{j\theta})s_m\gamma z^{-1}e^{j\phi}}{1 + (s_1s_2 - c_1c_2e^{j\theta})c_m\gamma z^{-1}e^{-j\phi}} \end{aligned} \tag{3.7}$$

3.2 Optical circuit design

By using the basic components introduced earlier, complex PICs can be designed to perform complex functions. Most of the optical simulation solves electromagnetic problems by using finite-difference time-domain method (FDTD) for the accurate modeling of the photonic devices. However, it requires massive calculation, so that it is not suitable for large PIC design.

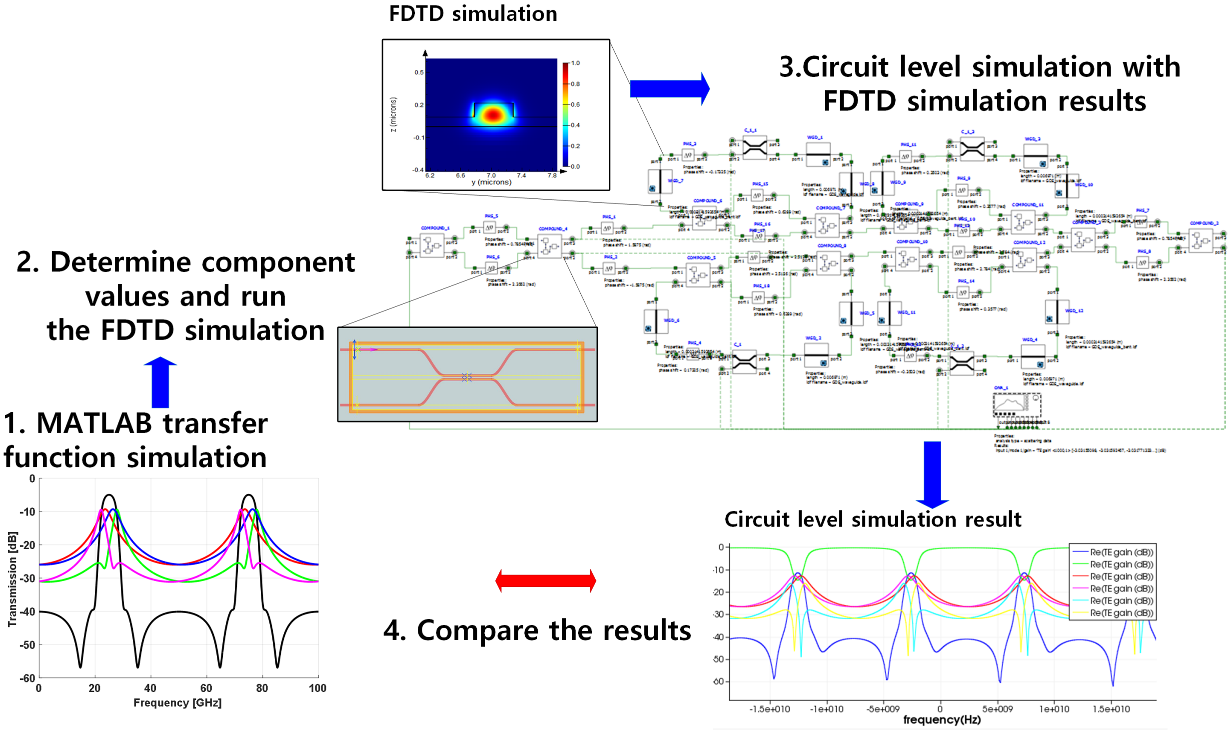

Figure 3.8: PIC design procedure.

To solve this issue, large size PICs are designed through this steps 3.8. Firstly, based on the transfer function approach, design the whole PIC. PIC transfer functions can be simulated through the MATLAB. This determines the desired coupling ratios of the MZIs, size of the ring resonator circumference, and PIC structure. Also, output response can be predicted with this steps. The next step is simulating each component through the FDTD. In this work, the Lumerical simulator is used to simulate the components. This allows determining details of each component. For example, the gap , and the coupling length of the directional coupler can be set accurately through this simulation steps. The last step is circuit level simulation. After the second step, parameters of each component are extracted and applied to the compact model of the PIC circuit level simulator (Interconnect). The PIC simulator solves scattering matrix of a component and provides frequency domain analysis. By comparing the MATLAB simulation result in the first step and the PIC circuit simulation result, PIC design can be validated. In fabricated PICs, they show sensitivity to the process variations that design with the margin or adding the tunability should be also considered during the design procedure.

4. AUTOMATIC MONITOR-BASED TUNING OF RECONFIGURABLE SILICON PHOTONIC APF-BASED POLE/ZERO FILTERS

4.1 Introduction

Wireless data traffic is projected to increase by 1000-fold in the near future [5] . An evolution of wireless networks is required to accommodate this explosion in future data traffic, such as shifting to higher frequency bands to utilize a wider amount of spectrum, reducing cell size, and realizing massive multiple-input/multiple-output (MIMO) systems at the base transceiver stations [21, 6] . Agile and reconfigurable integrated microwave photonic chips are promising candidates to meet these requirements due to their broadband operation, as well as being compact, lightweight, and power efficient [6, 69].

In these future wireless systems, receiver front-end filtering plays the critical role of guaranteeing the necessary RF performance and also relaxing subsequent analog-to-digital conversion (ADC) and digital signal processing (DSP) requirements [22]. Such filters should have pass-band bandwidth tunability, multi-GHz center frequency tunability, and high out-of-band rejection in order to work with different channel and frequency requirements [70]. These filter requirements are difficult to meet with conventional electrical filtering implementations [68]. Therefore, photonic filters are considered possible alternatives due to their innate high bandwidth, low loss, and wide tuning range properties. In addition, silicon photonic platforms compatible with conventional CMOS fabrication processes can enable chip-level realizations of these photonic filters in a conceptual highly-integrated mm-wave receiver front-end (Fig. 4.1).

Many different integrated photonic filter structures have been proposed [63, 71, 72, 40, 73, 74, 75, 76, 77, 41, 78, 79, 80, 67] with various challenges and trade-offs in achieving bandwidth and center frequency tunability while maintaining high frequency selectivity. Most of these filters can be described using digital filter concepts [63]. Structures with delay lines and no feedback paths are finite impulse response filters (FIR), since their impulse responses have finite duration

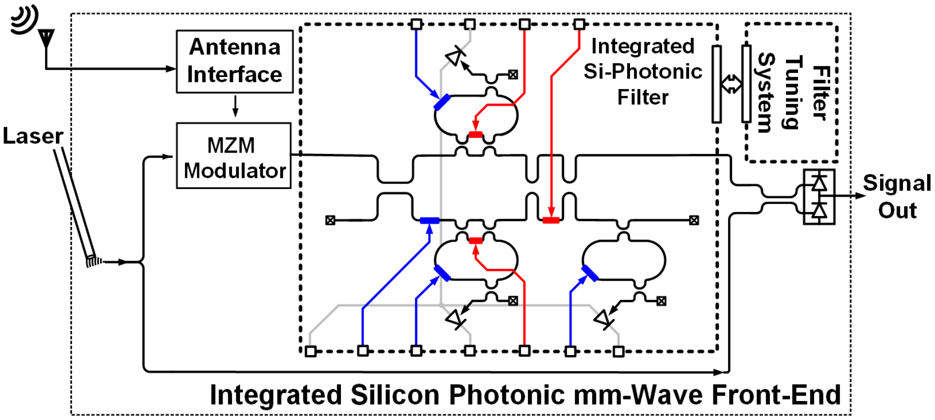

Figure 4.1: Conceptual integrated silicon photnoic mm-wave receiver front end

[71]. Photonic filters with feedback paths, often implemented with resonator structures such as Bragg gratings [72], thin films [63], ring resonators [40, 73, 74, 75, 76] or disk resonators [77], are infinite impulse response (IIR) filters. Among them, Bragg gratings and thin film-based filters show limited tunability due to physical limitations and disk resonator-based filters have high complexity due to their multi-mode operation. In contrast, ring resonator-based structures with tunable couplers are simpler and widely used for tunable IIR optical filters. An important issue is that FIR- or IIR-only structures show limited performance since they are zero- or pole-only systems. For example, cascaded ring resonators with tunable coupler structures are designed as frequency and bandwidth tunable filters, but the structure's flexibility is limited due to the dependency of the filter's bandwidth and out-of-band rejection [75, 76]. Therefore, lattice structure with both a delay line and ring resonator in each cell [71, 41, 78] and all-pass filter (APF)-based pole/zero structures are proposed for arbitrary bandpass filter synthesis [79, 80, 67, 66] by combining FIR and IIR filters together. However, the lattice filter structure requires a large number of couplers (2N+1) and phase shifters (2N) to tune an Nth-order filter response. On the other hand, an APF-based pole/zero filter architecture provides similar performance and flexibility in filter synthesis while demanding a reduced number of couplers (N+2) and phase shifters(N+2) for filter tuning. Additionally, tuning of the lattice filter is more challenging due to the feedforward paths [41]. This is not an issue in the APF-based structures that allow independent control of the filters poles and

zeros. The independent pole/zero control and the reduced number of tuning elements translates into simpler filter tuning algorithms and reduced power consumption for the APF-based structures. While APF-based filters have the flexibility to tune to an arbitrary filter response, they are sensitive to process and temperature variations. This necessitates precise control of the tuning phase shifters to calibrate and reconfigure the filter response. Most existing approaches involve manual tuning by visually monitoring the filter response using an optical network analyzer [74], which is time consuming, prone to human errors, requires expensive lab equipment, and generally not feasible in realistic operating environments with thermal variations. This motivates the development of automatic photonic filter calibration schemes. An interesting approach to automatically tune a filter response by monitoring a fraction of the output power has been demonstrated with high-order stacked ring filters [75]. While effective at center frequency tuning, this method does not provide bandwidth tunability. Programmable bandwidth tuning has been demonstrated with a 2^{nd}-order stacked ring structure [76], but this demonstration relies on a calibrated data set with different coupler settings, limiting the automatic and adaptive tuning capability.

This paper presents a monitor-based tuning algorithm suitable for APF-based pole/zero filter structures that allows for fully-automated bandwidth and center frequency tunability, while maintaining the targeted out-of-band rejection. Building upon the scheme described in [67] for a 2^{nd}-order structure, this work demonstrated faster calibration speed and successful filter calibration and reconfiguration for a 4^{th}-order structure. Section II details the pole/zero filter design and introduces the automatic monitor-based tuning algorithm. Photonic device design and fabrication details are discussed in Section III. Section IV presents experimental calibration and reconfiguration of 2^{nd}- and 4^{th}-order pole/zero filters and also discusses the key issue of thermal crosstalk between the heater-tuned phase shifters. A discussion of chip substrate thinning, which dramatically improves the filter calibration speed, and a general comparison with other silicon photonic filter demonstrations is given in Section V. Finally, Section VI concludes this work.

4.2 APF-Based Pole/Zero Filters

4.2.1 Filter Design

Fig. 4.2 shows the schematics of the designed APF-based pole/zero filters. As a single ring resonator produces a pole/zero pair, an Nth-order filter has N ring resonators in the main filter structure. These main rings are split equally between the upper and lower arms, which are connected with 50% couplers at the beginning/end. Several modifications are made to the basic filter structure to enable automatic filter tuning that both compensates for process variations and allows for filter reconfiguration. Each main ring cell includes a ring phase shifter ($\phi_{r1...N}$) for resonance tuning and an MZI coupler ($\kappa_{r1...N}$) for filter bandwidth tunability. An additional ring (Ring 3 and Ring 5 in the 2^{nd}- and 4^{th}-order structures, respectively), an MZI coupler (κ_{fe}), and front phase shifters ($\phi_{fe,up/dn}$) are employed to provide tunability for filter out-of-band rejection. Electrical monitoring is achieved via 5% coupled drop ports ($\kappa_{m1...N}$) with Germanium waveguide photodetectors (PD) are added to every ring resonator. The photonic filters Z-domain transfer functions are described in (4.1) and (4.2), with the ring round trip loss ($r_{1...N}$) considered.

$$H_{2nd}(z) = -\frac{j}{\sqrt{2}}[c_{fe}e^{j\phi_{fe,up}}\frac{c_{r1} - c_{m1}r_1e^{j\phi_{r1}}z^{-1}}{1 - c_{r1}c_m r_1 e^{j\phi_{r1}}z^{-1}} + s_{fe}e^{j\phi_{fe,dn}}\frac{c_{r2} - c_{m2}r_2e^{j\phi_{r2}}z^{-1}}{1 - c_{r2}c_m r_2 e^{j\phi_{r2}}z^{-1}}] \tag{4.1}$$

$$\begin{aligned} H_{4th}(z) = -\frac{j}{\sqrt{2}}[c_{fe}e^{j\phi_{fe,up}} & \frac{(c_{r1} - c_{m1}r_1e^{j\phi_{r1}}z^{-1})(c_{r2} - c_{m2}r_2e^{j\phi_{r2}}z^{-1})}{(1 - c_{r1}c_m r_1e^{j\phi_{r1}}z^{-1})(1 - c_{r2}c_m r_2e^{j\phi_{r2}}z^{-1})} \\ +s_{fe}e^{j\phi_{fe,dn}} & \frac{(c_{r3} - c_{m3}r_3e^{j\phi_{r3}}z^{-1})(c_{r4} - c_{m4}r_4e^{j\phi_{r4}}z^{-1})}{(1 - c_{r3}c_m r_3e^{j\phi_{r3}}z^{-1})(1 - c_{r4}c_m r_4e^{j\phi_{r4}}z^{-1})}] \end{aligned} \tag{4.2}$$

where $c_r = \sqrt{1 - k_r}$, $s_r = \sqrt{k_r}$, $c_m = \sqrt{1 - k_m}$, $c_{fe} = \sqrt{1 - kfe}$, and $s_{fe} = \sqrt{k_{fe}}$.

This APF-based pole/zero filter structure also offers flexibility in the specific filter response, as a single implementation can be dynamically tuned to synthesize Butterworth, Chebyshev, or elliptic responses [79, 80, 67, 67]. Since elliptic filter responses display a sharp cut-off and the narrowest transition width characteristic relative to other filters with the same order, 2^{nd}-order and

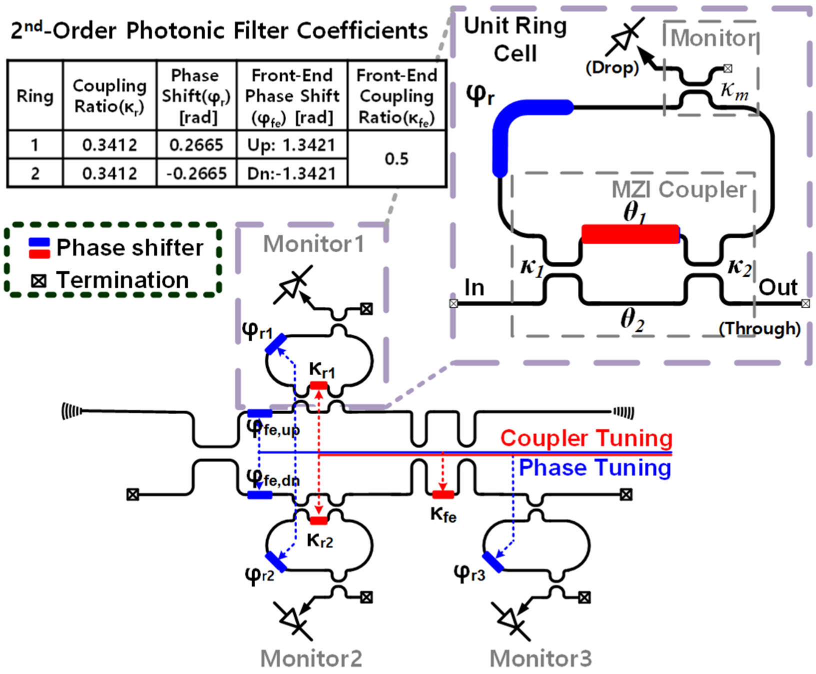

2^{nd}-Order Photonic Filter Coefficients

Ring	Coupling Ratio(κ_r)	Phase Shift(φ_r) [rad]	Front-End Phase Shift (φ_{fe}) [rad]	Front-End Coupling Ratio(κ_{fe})
1	0.3412	0.2665	Up: 1.3421	0.5
2	0.3412	-0.2665	Dn:-1.3421	

(a)

4^{th}-Order Photonic Filter Coefficients

Ring	Coupling Ratio(κ_r)	Phase Shift(φ_r) [rad]	Front-End Phase Shift (φ_{fe}) [rad]	Front-End Coupling Ratio (κ_{fe})
1	0.3461	-0.1732	Up: -1.3768	0.5
2	0.1223	0.3503		
3	0.3461	0.1732	Dn:1.3768	
4	0.1223	-0.3503		

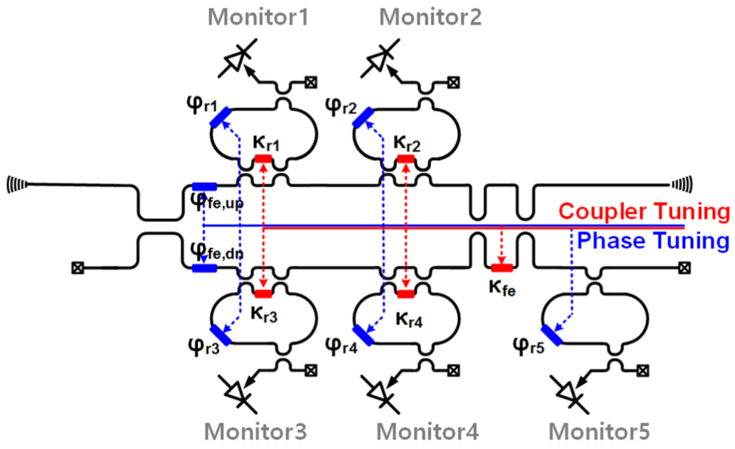

(b)

Figure 4.2: APF-based pole/zero photonic filter schematics and design parameters: (a) 2^{nd}-order structure with details of a unit ring cell and (b) 4^{th}-order structure.

4^{th}-order elliptic filters are designed to have 40dB out-of-band rejection and 0.1dB passband ripple. The elliptic filter transfer functions are mapped to the optical components based on an all-pass decomposition algorithm [63, 79], with the parameters summarized in Fig. 4.2 for 7GHz bandwidth 2^{nd}-order and 5GHz 4^{th}-order designs. Assuming 0.52dB ring round trip loss, Fig. 4.3 shows the photonic filters output and monitor responses centered at 25GHz with 50GHz free spectral range (FSR) relative to the 1550nm laser wavelength and the corresponding z-plane pole/zero positions.

4.2.2 Tuning Algorithm

4.2.2.1 Monitor-based Single Ring Cell Tuning Principle

Tuning of the photonic filters is achieved by individually adjusting the pole/zero position of each ring. In order to enable this, monitors are employed at each ring to acquire the ring response information. Referring to the zoomed-in single ring of Fig. 4.2 (a), each rings through-port response Z-domain transfer function can be expressed as (4.3)

$$H_{through}(z) = \frac{(c_1c_2e^{j\theta_1} - s_1s_2e^{j\theta_2}) - c_mre^{j(\theta_1+\theta_2+\phi_r)}z^{-1}}{1+(s_1s_2e^{j\theta_1} - c_1c_2e^{j\theta_2})c_mre^{j\phi_r}z^{-1}} \tag{4.3}$$

while the ring's drop-port response transfer function is (4.4)

$$H_{drop}(z) = \frac{(s_1c_2e^{j\theta_1} + c_1s_2e^{j\theta_2})s_mre^{j\phi_r}z^{-1}}{1+(s_1s_2e^{j\theta_1} - c_1c_2e^{j\theta_2})c_mre^{j\phi_r}z^{-1}} \tag{4.4}$$

Here c1, s1, c2, and s2 are the cross/through port coefficients for the fixed 50$\%$ couplers in the ring MZI couplers, θ_1 and θ_2 are the phase shift of the MZI coupler in each arm, and losses due to the couplers are considered in the round trip loss r. Based on (4.3) and (4.4), the rings through-port and drop-port responses share the same pole, and the through-port response has an additional zero. This results in a complementary relationship with the through-port notch frequency always aligned with the drop-port peak frequency. Therefore, the through-port response of the ring can be tuned by monitoring its drop-port response.

Monitoring the drop-port response provides information to tune the through-port response to achieve a desired resonance frequency and ring coupling factor. Resonance frequency tuning is

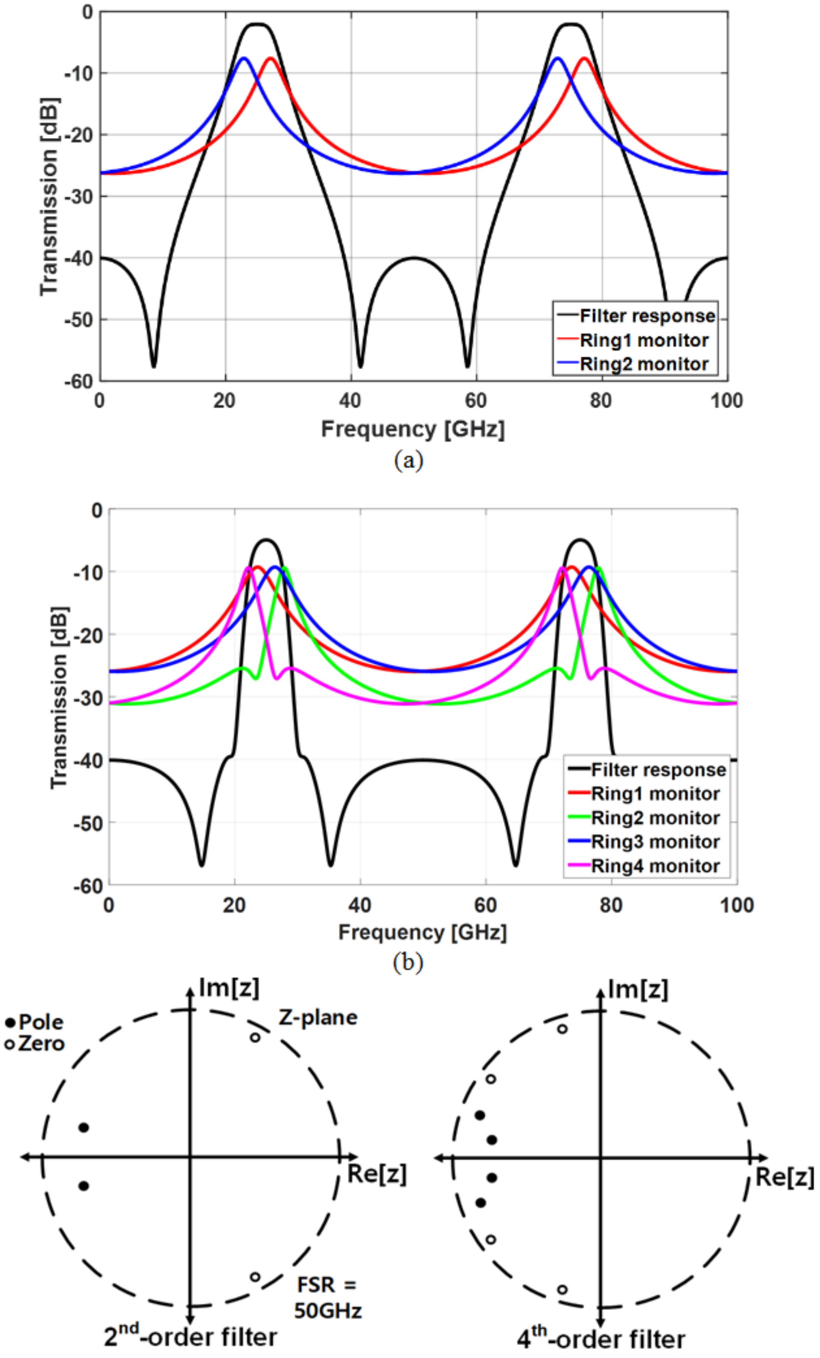

(a)

(b)

(c) (d)

Figure 4.3: Simulated APF-based pole/zero photonic elliptic filters centered at 25GHz with 50GHz FSR relative to the 1550nm laser wavelength. Output and monitor responses of the (a) 7GHz 2^{nd}-order filter and (b) 5GHz 4^{th}-order filter. Z-plane pole/zero plots of the (c) 2^{nd}-order filter and (d) 4^{th}-order filter.

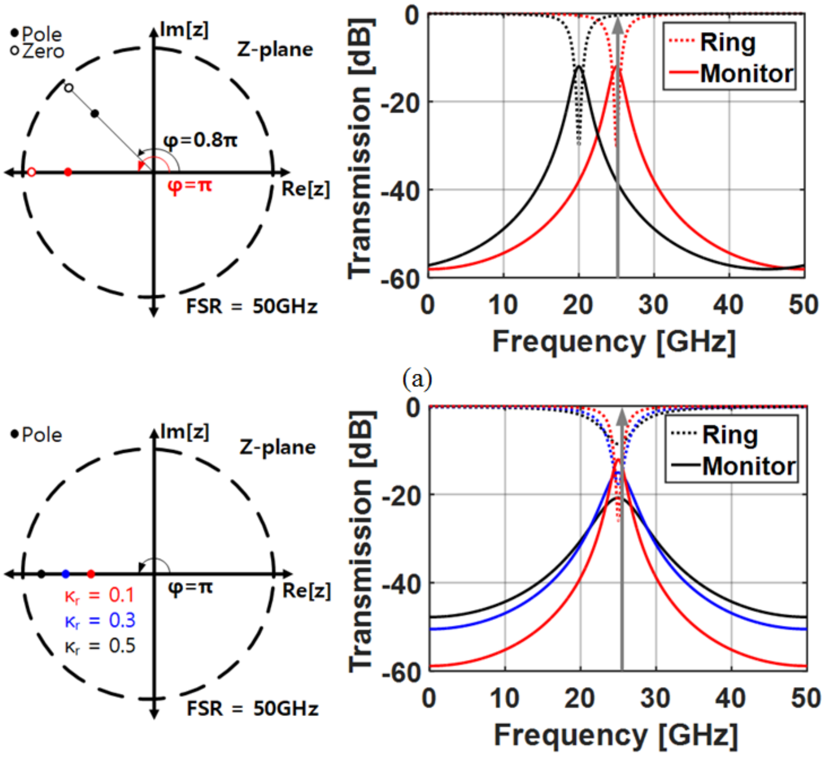

(a)

(b)

Figure 4.4: Monitor-based single ring cell tuning z-plane plot and corresponding frequency response for the ring through-port and monitor drop-port: (a) resonance tuning and (b) coupling ratio tuning.

achieved by adjusting the rings thermal phase shifter to change the angle of the pole position (Fig 4.4 (a)). Since the drop-port response shows the maximum output when the frequency of the ring resonator corresponds to the input laser frequency/wavelength, maximizing the drop-port signal allows tuning of the ring to the desired resonance frequency. Fig. 4.5 (a) shows how the drop-port monitor reading varies as the ring coupler ratio is tuned via the MZI coupler thermal phase shifter. Tuning this coupler changes the magnitude of the pole position, which affects the Q of the rings through-port response and its peak value (Fig. 4.4 (b)). Since the drop-port has a complimentary response compared to the through-port, the Q factor of the drop-port response also varies with different coupling ratios. Taking the maximum peak when the ring is critically coupled [28] as a reference, the MZI couplers characteristic sinusoidal response is used to tune to a desired coupling factor (Fig. 4.5 (b)). Through tuning both the rings phase shifter and MZI coupler, the angle and magnitude of each rings pole can be tuned as desired by monitoring the drop-port response with the appropriate laser stimulus. This individual pole position control allows reconstructing the desired filter response at the output. Any variations in the ring MZI couplers cross/through port coefficients due to fabrication tolerances is compensated by the proposed tuning algorithm [7], which is discussed in detail in the next subsection. This tuning procedure is valid for narrowband operation around a nominal (1550nm) center wavelength. Note that, due to the wavelength-dependent coupling ratio versus MZI coupler tuning power relationship, re-calibration is required if the filter operates at a different center wavelength.

4.2.2.2 Complete Filter Tuning Procedure

Based on the single ring cell tuning principle, a monitor-based automatic tuning algorithm is proposed to calibrate a complete filter response. Fig. 4.6 shows the algorithm flowchart for a 4^{th}-order filter, where the response is set by individually tuning the poles/zeros of a specific ring through monitoring its drop port response. There are three main steps: (1) coupler tuning, (2) filter resonance tuning, and (3) out-of-band rejection tuning. Fig. 7 shows the poles and zeros placement after each of these steps. This algorithm operation is verified in MATLAB utilizing models for the proposed fourth-order elliptic photonic filter [68, 81], with sub-steps included to address thermal crosstalk induced by the phase shifter heaters. Accurate automatic filter tuning results are obtained by utilizing the pre-characterized ring resonators V_π and round trip loss values.

Coupler tuning (κ_{r1-4}) of the filter, s ring resonators is performed first. Due to process variations, the initial ring resonator coupling ratios will deviate from the designed values shown in Fig. 4.2. To recover this, each ring, s coupling ratio is tuned to the critical coupling point with the input laser stimulus at the desired center frequency/wavelength. The drop-port peak response shows the maximum reading under this critical coupling ratio (Fig. 4.5 (a)). A coarse-to-fine search algorithm is used to rapidly find this monitor maximum point, with an initial 5-bit resolution sweep of the MZI coupler phase shifter across the full range that is followed by a fine 11-bit resolution sweep over the appropriate sub-range. This DAC resolution translates to a 0.002 coupler tuning accuracy. Fig. 4.5 (b) shows how this maximum critical coupling point [28] is utilized as a reference

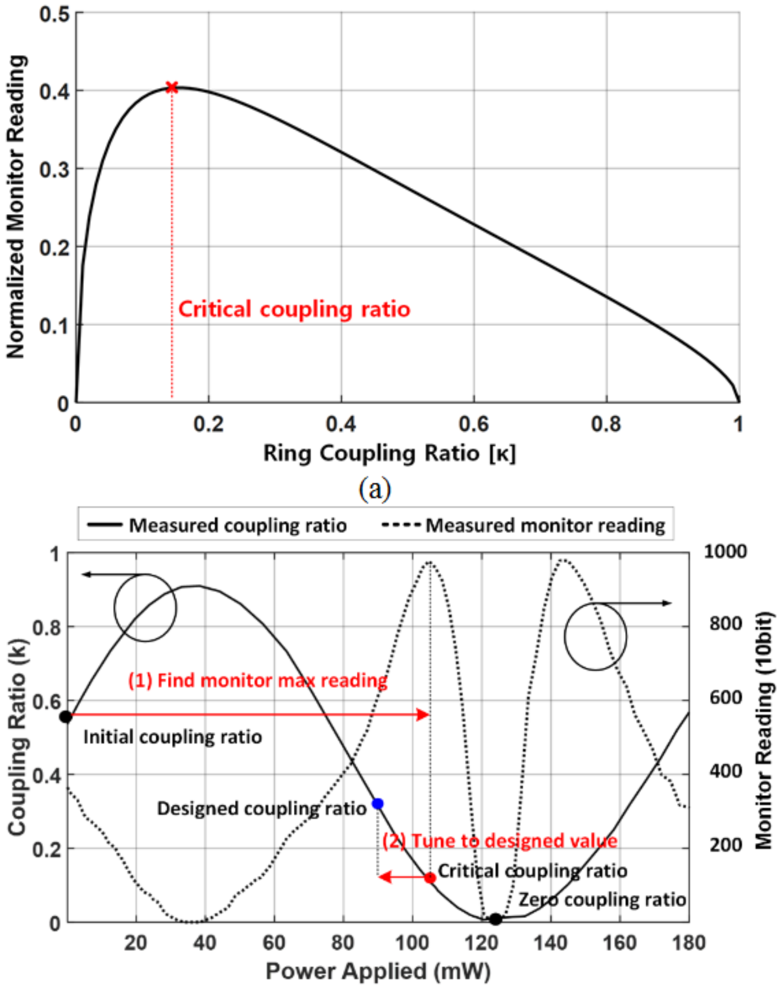

(a)

(b)

Figure 4.5: Simulated monitor peak response vs ring coupling ratio (utilizing measured 0.52dB round trip loss). (b) Coupler tuning procedure with measured MZI response vs thermal phase shifter heater power and corresponding measured monitor output. PD dark current is normalized out.

for tuning the coupling ratio to the designed value with the sinusoidal MZI coupler characteristic, which is relatively robust to the temperature variation induced by other heaters [76]. Since thermal crosstalk during the MZI coupler tuning also shifts the rings resonance point, the ring phase shifter is also adjusted in parallel to correct for this.

For the 4^{th}-order filter, the ring MZI couplers are tuned in order from Ring 1 to 4. Thus, the cascaded rings (Ring 2 and Ring 4) monitor responses are affected by the previous rings (Ring 1 and Ring 3) responses. In order to address this, the Ring 1 and Ring 3 coupling ratios are tuned

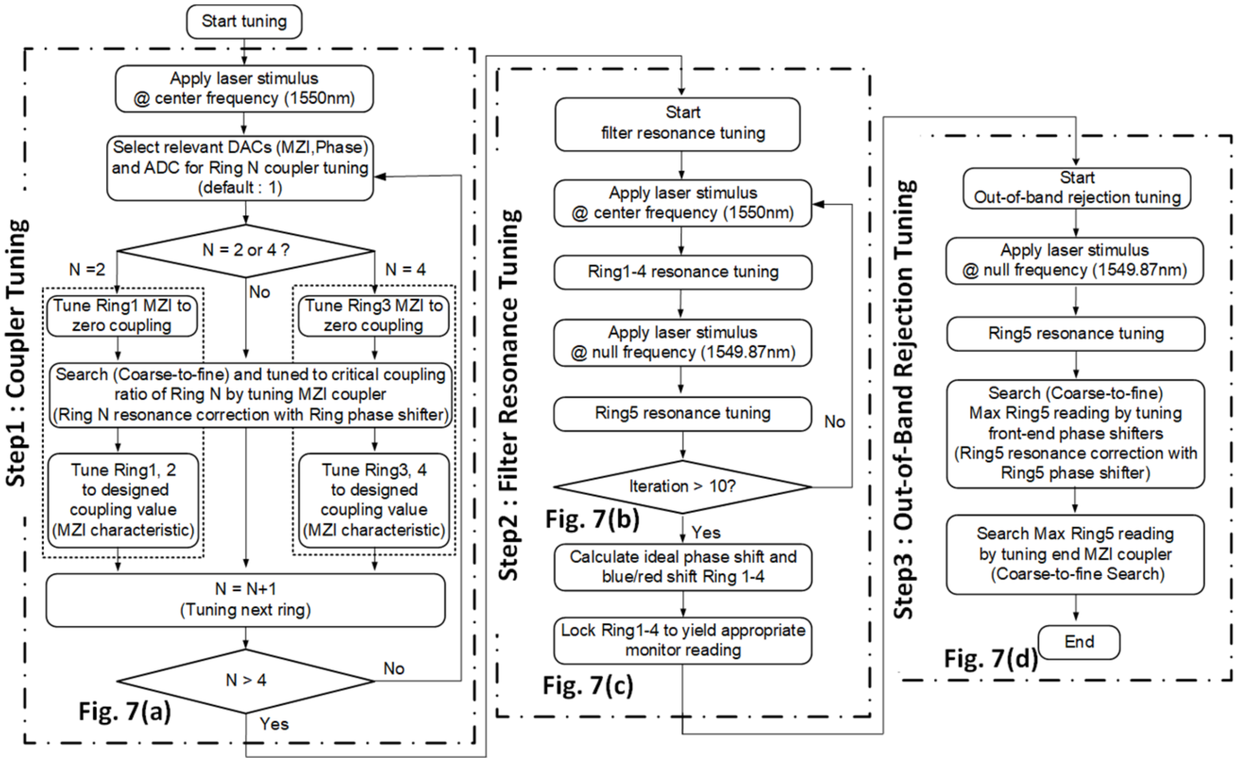

Figure 4.6: 4^{th}-order filter calibration algorithm flowchart.

to a zero coupling ratio to remove the influence of the previous rings on the Ring 2 and Ring 4 coupling ratios, respectively. First, the critical coupling ratios of the previous rings are found, stored, and the MZI sinusoidal characteristic is utilized to tune the previous ring coupling factors to zero. After tuning the cascaded ring, the coupling ratio of the previous ring is tuned back to the desired ratio to recover the desired filter shape at the output. A simulated filter response after the coupler tuning step is illustrated in Fig. 4.7 (a), with the filter response still highly distorted from process variations.

The second step in the tuning procedure is resonance tuning (ϕ_{r1-5}) to set the filter bandwidth and center frequency. By applying the laser input signal at the desired center frequency, Rings 1-4 (Ring 1 and 2 for a 2^{nd}-order filter) are resonance tuned in order by adjusting the ring phase shifter to maximize the monitor reading. Also, Ring 5 (Ring 3 for a 2^{nd}-order filter) is tuned to the filter out-of-band null frequency by switching the input laser to this frequency. Thermal crosstalk effects are addressed by including the Ring 5 tuning in this step and performing multiple iterations

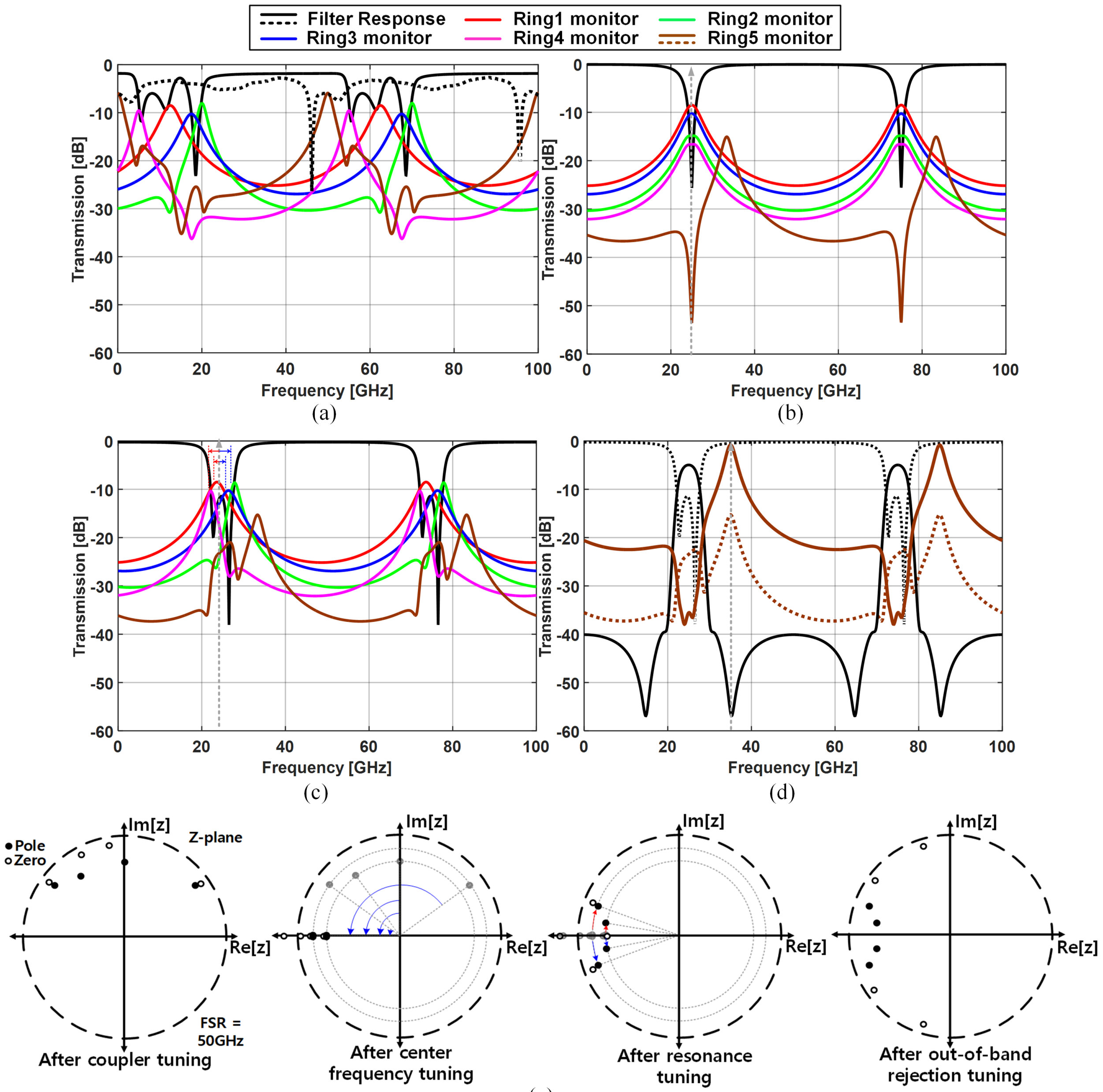

(a) (b)

(c) (d)

(e)

Figure 4.7: Simulated filter output and monitor responses: (a) after coupler tuning, (b) after center frequency tuning, (c) after resonance tuning, and (d) after out-of-band rejection tuning, with the dashed line representing the responses before tuning, (e) z-plane pole-zero position after each tuning step.

across the rings. Fig. 4.7 (b) shows the simulated filter response with the four main rings tuned to the center frequency and the filter output displaying a sharp resonance at this point. In order to form the bandpass filter shape while maintaining the input laser source at the center frequency, first

Rings 1 and 4 are red shifted while Rings 2 and 3 are blue shifted based on calculated ideal values. Then, further adjustment of the ring phase shifters lock the ring monitor readings to the appropriate percentage of the peak value corresponding to the individual rings desired resonance frequency. Fig. 4.7 (c) shows that the bandwidth of the filter is now formed after this step. However, the rejection band performance is still very poor. In order to improve the out-of-band rejection, the end MZI coupler (κ_{fe}) and front phase shifters ($\phi_{fe,up/dn}$) are tuned in the final step. Ring 5 (Ring 3 for a 2^{nd}-order filter), placed at the filters complementary port, allows for out-of-band rejection tuning by maximizing the rings monitor response with the input laser set to the filter null frequency. A similar coarse-to-fine procedure is used to first tune the front phase shifters and then tune the end MZI coupler. Fig. 4.7 (d) shows that after this final tuning step the photonic filter has a well-defined bandpass shape.

4.3 Device Design and Fabrication

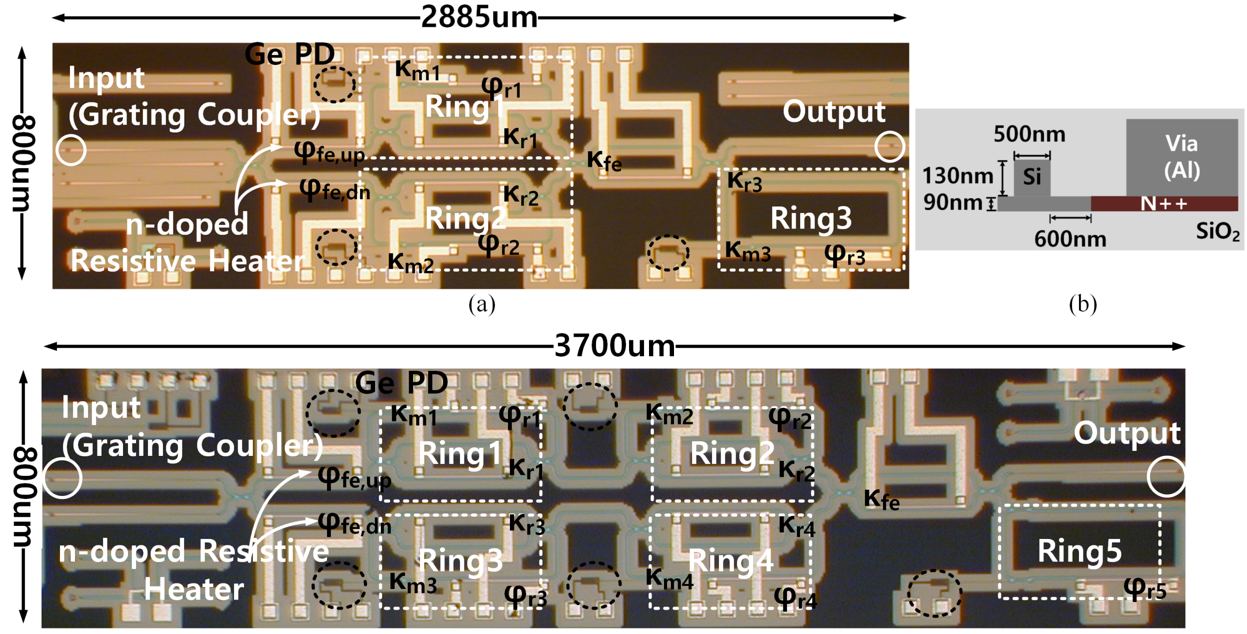

(a) (b)

(c)

Figure 4.8: (a) Chip micrograph of the 2^{nd}-order APF-based pole/zero filter. (b) Cross-section schematic of the rib waveguide with resistive heater. (c) Chip micrograph of the 4^{th}-order APF-based pole/zero filter.

The presented automatic photonic filter tuning algorithm is demonstrated using 2^{nd}-order and 4^{th}-order APF-based pole/zero filers fabricated in the IME A*STAR baseline SI photonics process that utilizes SOI wafers. As shown in the die micrographs of Fig. 8, the 2^{nd}-order filter structure occupies $2885\mu m \times 800\mu m$, and 4^{th}-order filter structure utilizes $3700\mu m \times 800\mu m.$

1-D grating couplers with a center wavelength around 1550nm are placed at the filters input and output ports. Rib waveguides are employed with a 220nm total slab height, 90nm thick partially-etched strip, and a 500nm width silicon core surrounded by a SiO_2 cladding. The filters rings are designed as rounded rectangles with $25\mu m$ radius corners to minimize area and waveguide loss. A 50GHz FSR is achieved by setting the ring circumference to $1554\mu m.$ Directional couplers with a 200nm gap are employed throughout the filter structure, with the couplers in the tunable MZI structures having a nominal 50% coupling ratio. The ring drop ports are designed for 5% coupling and have waveguide Ge p-i-n PDs. Thermo-optic phase shifters, which have lower tuning speed relative to electro-optic plasma dispersion phase shifters [82], are chosen due to their low loss characteristics. N-doped resistive heaters placed $0.6\mu m$ away from the sidewall of the waveguide slab realize the thermos-optic phase shifters with tunability over the full FSR range. This heater placement does not introduce any additional waveguide loss which is critical to the filter Q factor. Metal bondpads are present at the top and bottom of the filters to electrically control the phase shifter heaters and provide the bias and electrically monitoring of the drop-port PDs. One important fabrication parameter is the silicon substrate thickness, which has a default value of $750\mu m$ below the $2\mu m$ buried oxide layer. This large thickness relative to the buried oxide layer induces thermal crosstalk between the phase shifters and also results in long thermal time constants. To solve this issue, the silicon substrate is thinned to $75\mu m$ with an additional CMP process. The following section demonstrates the 2^{nd}-order filter with both the original thick and CMP processed substrate and the 4^{th}-order filter with the CMP processed substrate.

4.4 Experimental Results

4.4.1 Measurement Setup

Fig. 4.9(a) shows the automatic monitor-based tuning system block diagram for the 4th-order filter. The photonic integrated circuit (PIC) is wire-bonded to the custom-designed PCB board that includes low-bandwidth transimpedance amplifiers (TIAs) and 10-bit analog-to-digital converters (ADCs) to sense the average photocurrent from the filters monitor waveguide Ge PDs that are biased at -1V. These ADCs interface with a microcontroller (Arduino Due) that implements the filter tuning algorithm by controlling 16-bit digital-to-analog converters (DACs) through a serial peripheral interface (SPI). The DACs apply control voltages across the resistive heaters on the PIC to adjust the optical phase shifters. A free-space optical fiber coupling stage couples a tunable laser (Luna Phoenix 1400) into the PIC (Fig. 4.9(b)). This tunable laser generates the two wavelengths (center and null frequencies) required for the calibration and is also controlled by the same microcontroller to realize a fully automated tuning system. The PIC sits on a large metal footprint with thermal vias down to the bottom layer of the PCB where a thermoelectric cooler (TEC) is placed with thermal grease passivation to provide temperature stabilization. An optical vector network analyzer (OVNA) is coupled into the integrated photonic chip for device characterization and verification of the calibrated filter response. Each ring resonator is characterized independently by configuring zero coupling at the other rings and using the OVNA time domain response at the filter output. From the ring resonators Jones matrix [83] a 0.52dB (±0.1dB) round trip loss and 0.3963nm (49.64GHz) FSR is determined. The critical coupling values used in the automatic tuning algorithm are determined based on these characterized round trip loss measurements of each ring.

4.4.2 Second-Order Pole/Zero Filter Tuning

The proposed filter tuning algorithm is demonstrated first with the 2nd-order photonic pole/zero filter. Fig. 4.10 shows that the initial filter response of the fabricated device, and the response severely deviates from the desired bandpass shape and also varies between the shown 2 samples.

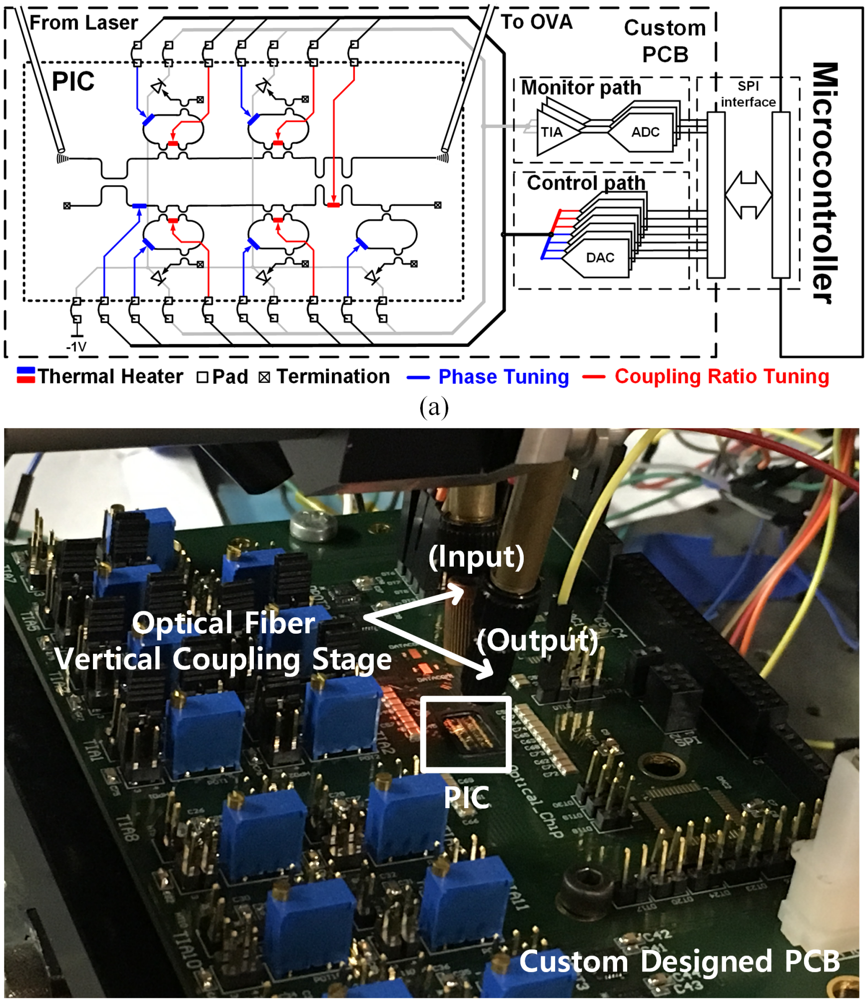

(a)

(b)

Figure 4.9: Automatic monitor-based tuning system: (a) block diagram with the 4^{th}-order filter and (b) photograph of the system with the optical fiber vertical coupling stage.

Utilizing center 1550.1nm and null 1549.9nm wavelengths from the tunable laser, the filter tuning algorithm is applied, and a well-defined bandwidth shape is recovered. However, as shown in Fig. 4.11(a), a long 1778s initial calibration time is required for the thick substrate sample. A primary reason for this is that the temperature sensitivity of the rings resonance necessitated multiple tuning iterations to compensate for thermal crosstalk, and these iterations where slowed due to the PIC heat capacity causing large thermal time constants [82, 84].

This effect is studied in the Fig. 4.12 COMSOL modeling results of the integrated resistive

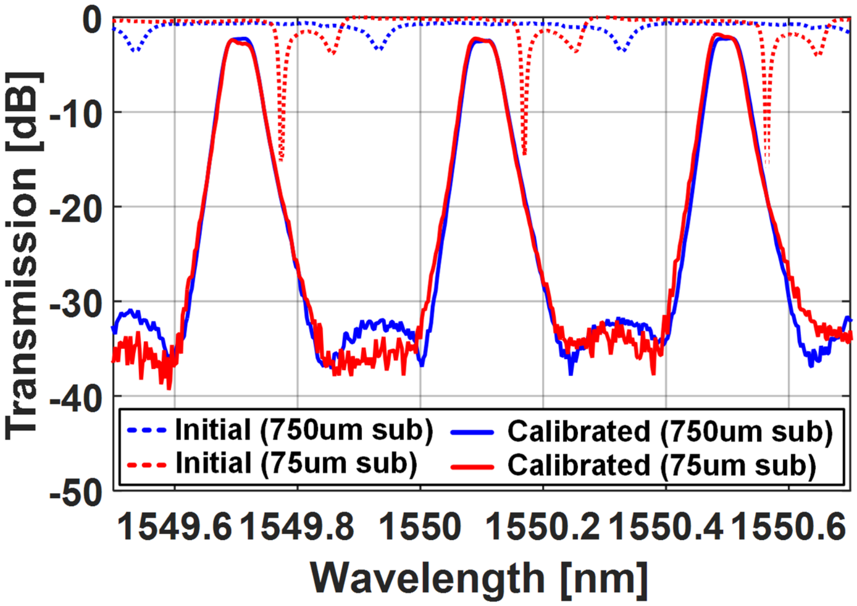

Figure 4.10: Measured 2^{nd}-order pole/zero filter output responses before/after calibration with original 750μm silicon substrate and thinned 75μm substrate.

heater used in the phase shifters. Referring to Fig. 4.8, the N-doped resistive heater is primarily surrounded by silicon dioxide, with the thick silicon substrate 2μm beneath the buried oxide layer. The top of the silicon dioxide boundary is interfaced with convection cooling, while the bottom of the silicon substrate is assumed to have a constant 300K temperature to emulate the interface with the TEC cooler. The simulated temperature distribution along the Fig. 4.12(a) cutline where the silicon waveguides are placed is shown in Fig. 4.12(b) for different silicon substrate thicknesses. At 100μm away from the heater, which is the minimum adjacent phase shifter separation, a 700μm substrate shows an elevated 320K temperature when the heater is near 405K. Thinning the substrate down to 100μm dramatically reduces this thermal crosstalk to only an additional 2.1K relative to the TEC reference. A thinner substrate also significantly reduces the heat capacity H due to the smaller mass. This reduces the thermal time constant (τ) which can be expressed as τ=$\Delta T_{\pi} H/P_{\pi}$) where ΔT_{π} is the temperature change and P_{π} is the power dissipation required to achieve π phase shift, respectively [82, 84].

Another issue is that dramatically different thermal time constants are observed for the heating

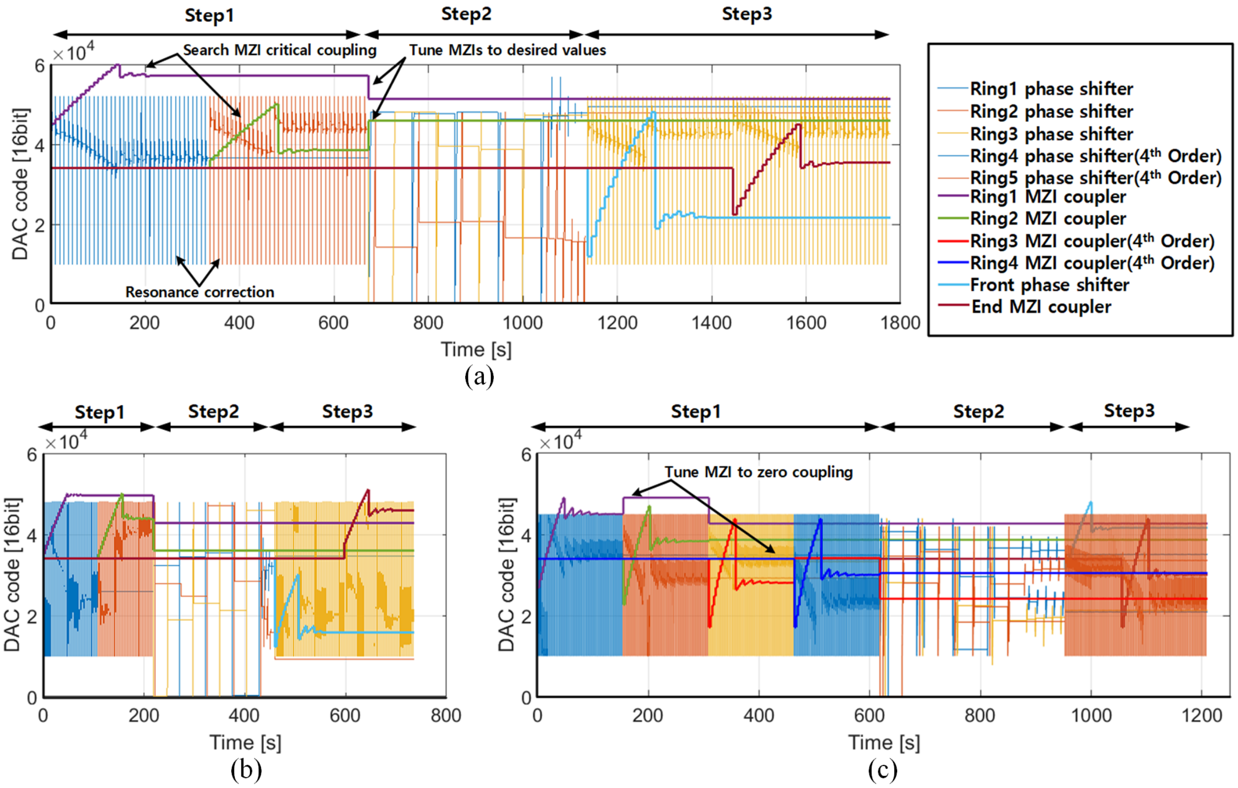

(a)

(b)

(c)

Figure 4.11: Tuning convergence: (a)2^{nd}-order filter w/ 750μm substrate, (b)2^{nd}-order filter w/ 75μm substrate, and (c)4^{th}-order filter w/ 75μm Si substrate.

and cooling processes [85]. This is because during the heating process the heater directly heats up the waveguide, whereas cooling relies on thermal diffusion and is sensitive to boundary conditions. For example, the original 750μm thick substrate PIC could support a minimum 200μs tuning time step during heating, but required a 300ms cooling time. Even with a conventional centimeter-scale TEC cooler, this solution is poorly suited to a relatively thick PIC substrate [86].

These thermal effects are dramatically reduced by thinning the PIC substrate to 75μm. This allowed support of a minimum 100μs tuning time step during heating and a 10ms cooling time. As shown in Fig. 4.11(b), this dramatically reduced the initial filter calibration time to 736s. These measurements utilize an ADC acquisition time of 4.5μs, with digital filtering over 100 samples applied for noise suppression. Overall, the smaller thermal time constants with the thinner substrate allowed a faster measured tuning speed and improved convergence behavior.

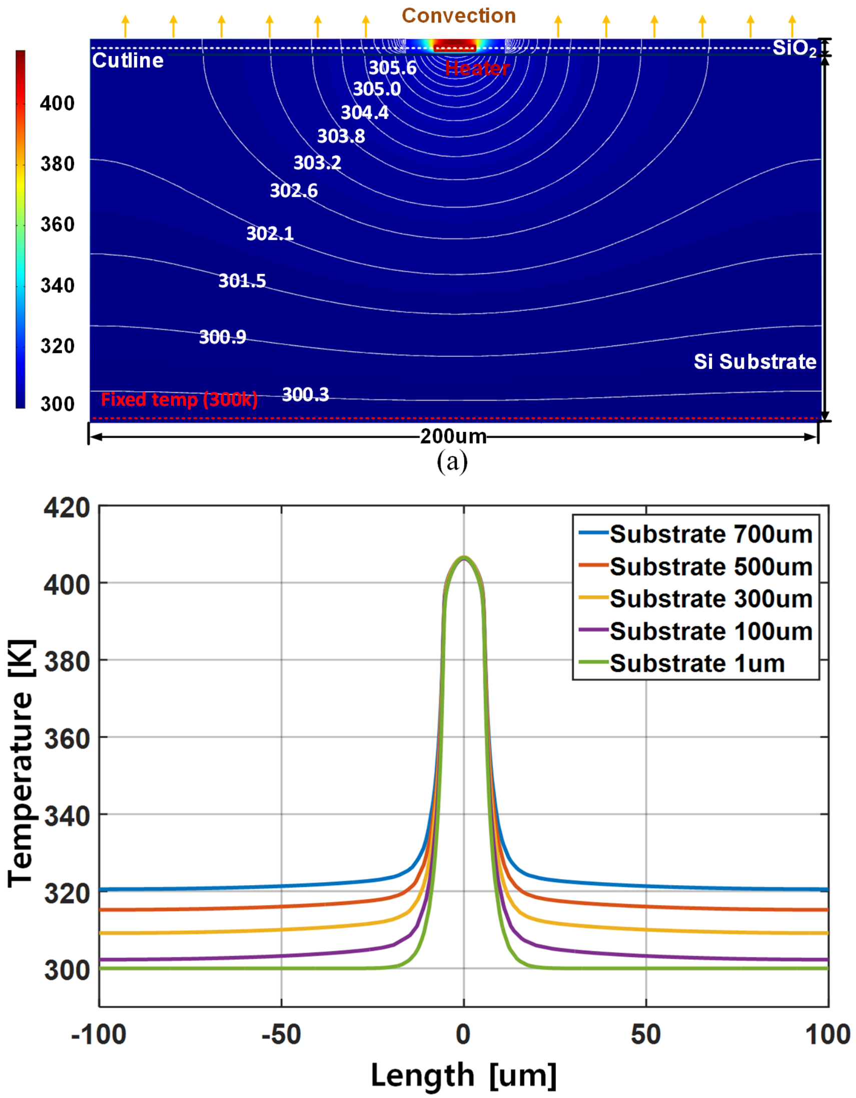

(a)

(b)

Figure 4.12: Integrated resistive heater thermal silulation: (a)temperature cross-section and (b)temperature distribution along waveguide-level cutline.

Fig. 4.13 shows the 2^{nd}-order filter measurement results after each tuning step. Due to process variations, the filter has a very poor initial response (Fig. 4.13(a)). After the Ring 1 and Ring 2 coupler values are recovered through the coupler tuning procedure with the 1550.1nm center wavelength (Fig. 4.13(b)), the filters center frequency and bandwidth still deviate significantly. The filter begins to come together after the resonance tuning step (Fig. 4.13(c)), with the center frequency and bandwidth well defined. By maximizing the monitor3 response through tuning front phase shifters and end MZI coupler with the 1549.9nm null wavelength, the filter response is recovered to the designed response (Fig. 4.13(d)). Fig. 4.10 shows the calibrated 2^{nd}-order filter responses with 6.89GHz 3dB pass bandwidth centered at 1550.1nm for both $750\mu m$ and $75\mu m$ silicon substrate thickness samples. Despite large differences between the two initial responses and substrate thickness, both the filter responses are automatically calibrated closely to the desired response. The minor deviations between the two responses is primarily due to slight variations in the coupling coefficients and loss differences.

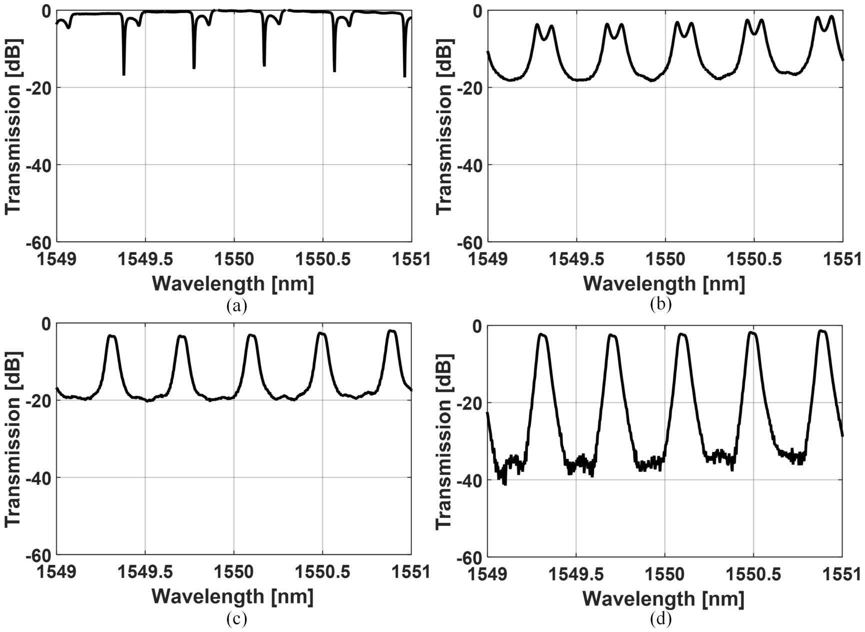

(a) (b) (c) (d)

Figure 4.13: Measured 2^{nd}-order filter output responses (a) before calibration, (b)after coupling ratio tuning, (c) after resonance tuning, and (d) after out-of-band rejection tuning.

4.4.3 Fourth-Order Pole/Zero Filter Tuning

Calibration of a 4th-order filter is also demonstrated utilizing the three main tuning steps. The 4th-order pole/zero structure has more heaters (11) to control and is more sensitive to thermal crosstalk than the 2^{nd}-order structure. Thus, in order to achieve a reasonable convergence time, the 4th-order filter calibration was demonstrated only with a thinned $75\mu m$ substrate sample that has reduced thermal crosstalk sensitivity.

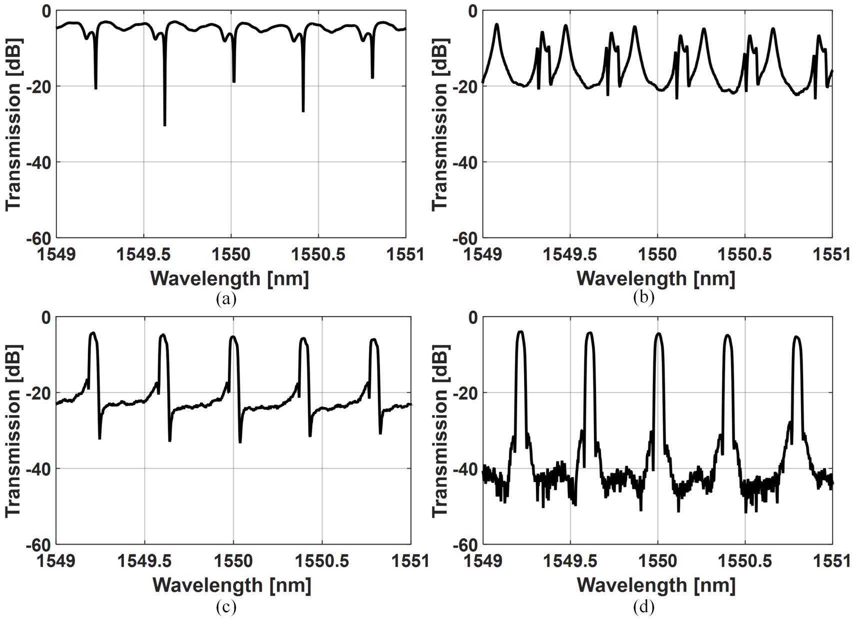

Figure 4.14: Measured 4^{th}-order filter output responses (a) before calibration, (b)after coupling ratio tuning, (c) after resonance tuning, and (d) after out-of-band rejection tuning.

Fig. 4.14 shows the 4^{th}-order filter output response after each tuning step, with the DAC convergence waveforms also shown in Fig. 4.11(c). Similar to the 2^{nd}-order filter, the original 4^{th}-order filter response is severely degraded from process variations (Fig. 4.14(a)). After the coupling ratio and resonance tuning, the filter bandwidth and center frequency is defined (Fig. 4.14(b) and (c)). This verifies that the cascaded ring coupling ratio can be tuned successfully by setting Ring 1 and 3 MZI to zero coupling during Ring 2 and 4 tuning and that the 5 ring resonance frequencies can be set in an iterative fashion. After maximizing the Ring 5 monitor response to optimize the out-of-band rejection, Fig. 4.14(d) shows that the calibrated 4^{th}-order filter response achieves the expected narrower passband and sharper roll off relative to the 2^{nd}-order filter response. The total initial calibration time was 1223s, which is slightly less than twice the 75μm substrate 2^{nd}-order filter time and also shorter than the 750μm substrate 2^{nd}-order filter time.

Ten calibration trials are performed with the same filter sample to verify the automatic tuning

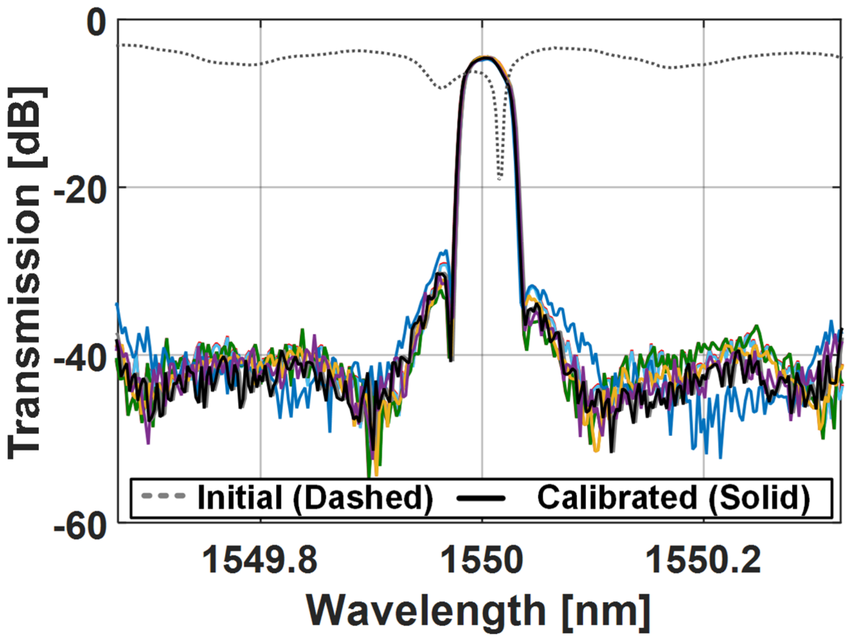

Figure 4.15: Measured 4^{th}-order filter calibrated responses for 10 trials with the same sample. The dashed line represents the initial response.

	Mean	Std. Dev.
Passband Loss [dB]	-4.67	0.04
Center Wavelength [nm]	1550.02	0.0083
3dB Bandwidth [GHz]	5.061	0.142

Table 4.1: Calibrated 4^{th}-order filter response variations.

procedure. The superposed 10 trials of Fig. 4.15 show the consistency of the automatic tuning scheme, with the variations quantified in Table. 4.1. Both the filter passband loss and center wavelength show very small variation, while the bandwidth has a standard deviation of less than 3%. These variations are mainly due to noise from the monitor photodetectors, TIAs, and finite ADC resolution.

4.4.4 Filter Reconfiguration

The information extracted during the initial calibration enables reconfiguration of bandwidth and center frequency, which can provide these silicon photonic filters with the flexibility to support

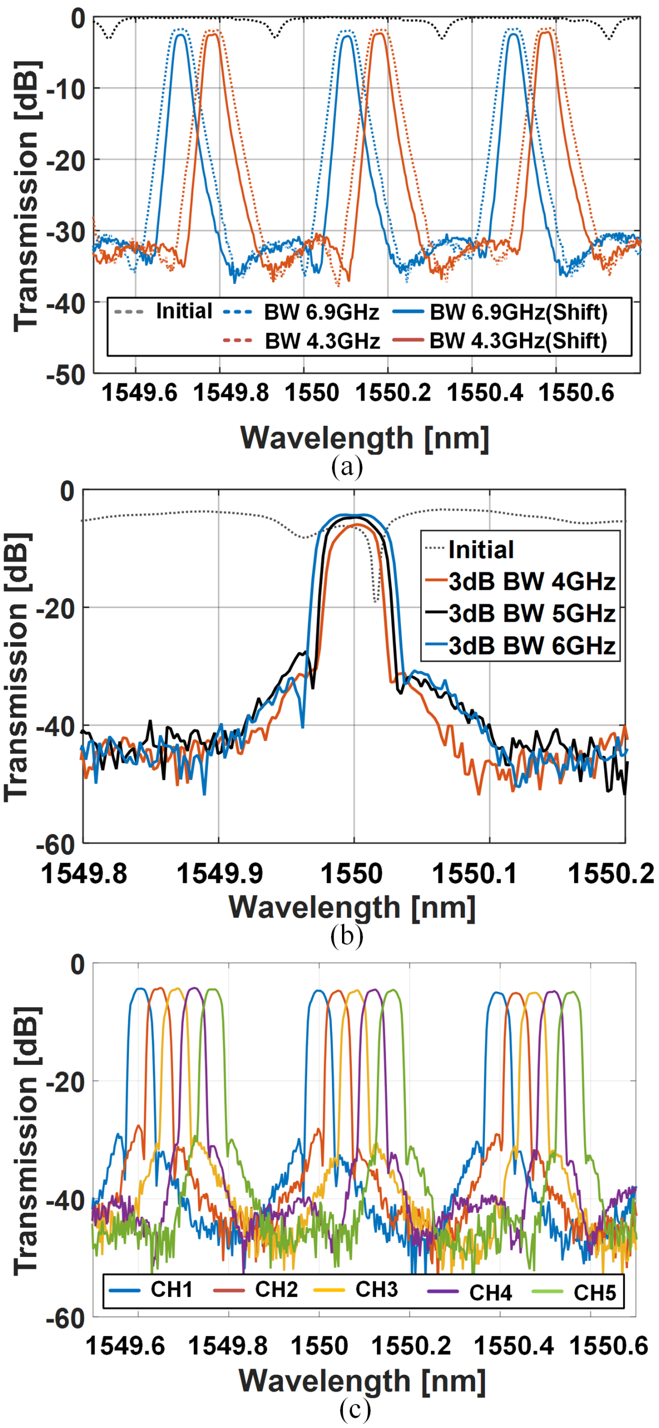

(a)

(b)

(c)

Figure 4.16: Reconfiguration of APF-based pole/zero photonic filters: (a) 2^{nd}-order filter, (b) 4^{th}-order filter with different 3-dB bandwidth, and (c) 4^{th}-order filter positioned at 5 different frequencies at 0.04nm spacing.

different communication systems. Fig. 4.16(a) shows the 2^{nd}-order filter ($750\mu m$ substrate) that is initially calibrated to 6.89GHz 3dB bandwidth with 32dB out-of-band rejection. A 9.8GHz frequency shift is shown by simply shifting Ring 1 and 2 phase shifters ($\phi_{r1,2}$) by the same amount. The switching between different responses is only limited by the cooling, with a measured 300ms time observed. It is also possible to reconfigure the 3dB bandwidth to 4.3GHz and maintain the same rejection by repeating the full calibration procedure.

Bandwidth reconfiguration of the 4^{th}-order filter is shown in Fig. 4.16(b). The filter is initially configured to have 5.02GHz 3dB bandwidth with better than 33dB rejection. By utilizing the proposed algorithm with different optical parameter sets, the filter is reconfigured to have 6.13GHz and 4.03GHz 3dB bandwidth. Note that, due to the ring round trip loss, the passband level reduces as the bandwidth decreases. Reconfiguration of the filter to 5 different center frequencies spaced by 0.04nm is shown in Fig. 4.16(c). While ideally this reconfiguration could be achieved simply by shifting the four main ring phase shifters, as in the 2^{nd}-order filter case, complex thermal crosstalk between the four main ring heaters prevents preservation of the relative phase and ruins the filter output bandwidth and shape. Therefore, a foreground calibration scheme with five tuning procedures with different laser input frequencies is performed and the individual DAC codes are stored. Recalling these stored DAC codes allows for rapid reconfiguration of the 4^{th}-order filter to the different center frequencies. The switching between different responses is only limited by the cooling, with a measured 300ms time observed.

4.5 Discussion

Table II shows the presented integrated silicon photonic filters performance summary and provides a comparison with 5^{th}-order stacked ring [75], 2nd-order stacked ring [76], 4^{th}-order APF-based lattice [41], 4^{th} -order pole/zero [80] and 4-tap FIR structures [87]. The presented approach is the only one to offer fully automatic calibration of the center frequency, bandwidth, and out-of-band rejection. This exceeds the automatic tuning capabilities of previous stacked ring structures that only offer center frequency and limited bandwidth calibration [75, 76]. Also, utilizing the same 4^{th}-order pole/zero filter structure, this work showed better out-of-band rejection performance and

	This work (2^{nd}-order)	This work (4^{th}-order)	[75]	[76]	[41]	[80]	[87]
Structure	2^{nd}-order Pole/zero APF-based	4^{th}-order Pole/zero APF-based	5^{th}-order Stacked ring	2^{nd}-order Stacked ring ring	4^{th}-order APF-based Lattice	4^{th}-order Pole/zero APF-based	4-tap FIR
Filter Performance							
FSR [nm]	0.396	0.396	2.32	2.1	0.0792	0.1307	0.8
3dB BW [nm]	0.055	0.039	0.247	0.265	0.0079	0.0079	0.247
(GHz)	6.89	5	31.2	33.4	1	1	31.2
Out-of-band rejection [dB]	32	33	45	25	30	26	30
Reconfiguration							
Center frequency	Y	Y	Y	Y	Y	Y	Y
Bandwidth	Y	Y	N	Y	Y	Y	Y
Automatic Calibration							
Center frequency	Y	Y	Y	Y	N	N	N
Bandwidth	Y	Y	N	Y*	N	N	N
Out-of-band rejection [dB]	Y	Y	N	N	N	N	N

* Showed bandwidth programmability after bandwidth calibration.

Table 4.2: Integrated silicon photonic filter performance summary and comparisons

agreement with the ideal filter response due to the precision of the automatic filter tuning approach relative to a manual tuning approach [80]. Note that the 5% coupled drop port monitors cause the round trip loss of each ring resonator to increase and results in an additional 1.2dB passband loss penalty in the filter response. This passband loss penalty can potentially be removed by implementing transparent detectors, such as a contactless integrated photonic probe (CLIPP) [88], instead of the 5% coupled drop port monitors.

A key observation in this work is that thermal crosstalk limited reduction in filter calibration time. This necessitated multiple iterations throughout the main steps of the tuning process. While PIC substrate thinning can reduce this effect, there are several other options to consider for further improvement. The first option is employing a more power efficient heater. This work placed resistive heaters next to the phase shifter waveguides in a manner that allowed for low waveguide loss. However, resistive heaters directly doped on the waveguide [75, 76] or metal heaters [85] may provide a reduction in thermal crosstalk and improved power efficiency at the cost of higher waveguide loss. Also, the designed heater geometry was relatively large to reduce the maximum temperature for 2π phase shift. Applying a higher maximum temperature to a smaller heater with less thermal capacity can provide more localized heating and less thermal crosstalk. However, one important consideration is how the maximum voltage swing changes, as this can limit further integration with electrical CMOS ICs [82]. The second option is improving the thermal isolation between the heaters. Thermal transfer from one heater to another can be reduced by adding a deep trench between the heaters [89] or using thick SOI wafers [90]. A final option involves integrating the thermo-electric module. Potential device-integrated micro thermo-electric coolers (μTECs) [86], would allow direct temperature control of individual heaters.

4.6 Conclusion

This paper has presented an automatic monitor-based filter calibration and reconfiguration scheme for silicon photonic APF-based pole/zero filters. Utilizing electrical information obtained from monitor photodetectors at the filters rings drop ports, the proposed tuning algorithm controls thermal phase shifters to calibrate severely degraded initial responses of both 2^{nd}- and 4^{th}-order elliptic filters. The information extracted during this initial calibration enables reconfiguration of bandwidth and center frequency. PIC substrate thinning is shown to dramatically reduce thermal crosstalk between the phase shifter heaters and allow for faster filter tuning times. Overall, leveraging the proposed automatic photonic filter calibration scheme can allow for robust operation of silicon photonic filters in future wideband communication systems.

(c) 2018 IEEE. Reprinted, with permission, from [Gihoon Choo, Automatic Monitor-Based Tuning of Reconfigurable Silicon Photonic APF-Based Pole/Zero Filters, Journal of Lightwave Technology, Volume: 36, Issue: 10, May15, 15 2018]

5. AUTOMATIC MONITOR-BASED TUNING OF RF SILICON PHOTONIC TRUE-TIME-DELAY BEAMFORMING NETWORKS

5.1 Introduction

Continuous growth in wireless data traffic makes millimeter wave (mm-wave) frequencies more attractive due to abundantly available spectrum, compact antenna size, and potential use in commercial 5G applications [5, 6]. An important part of a mm-wave 5G cellular communications transceiver is an antenna array that allows for power-efficient transmission, avoidance of overlap between communication cells, and modification of the coverage range of a single base station [91]. Within the antenna array system, the beamforming network plays a critical role by providing beam focusing and steering to a specific direction. Unfortunately, conventional electronic beamforming networks that operate in the mm-wave range face significant challenges in achieving the required instantaneous bandwidth and high beam steering resolution in a small form factor. Integrated microwave photonic circuits offer a potential solution due to their broadband operation, immunity to electromagnetic interference, and compact size.

Conventional electronic beamforming systems based on phase shifters display frequency dependent behavior, called beam squint [92, 51]. Thus, antenna array systems require true time-delay (TTD) beamforming to obtain wide instantaneous bandwidth and squint-free operation of the antenna array [93, 27, 94]. Several photonic approaches have been proposed to address this. An intuitive approach involves using a TTD network consisting of fixed-length optical fibers and sets of switchable fiber delay lines to create discrete delay differences [95]. Other fiber-based solutions include utilizing either a fiber optic prism [96] or fiber Bragg-gratings [97, 59, 98] to create variable delays for different source wavelengths. While these fiber-based systems perform well, they are relatively bulky. Integrated photonic beamforming networks offer a dramatic reduction in form factor. One integrated approach utilizes a TTD network with integrated waveguide delay lines and switch elements to provide discrete delay differences [99, 100, 101]. This allows for simple switch-

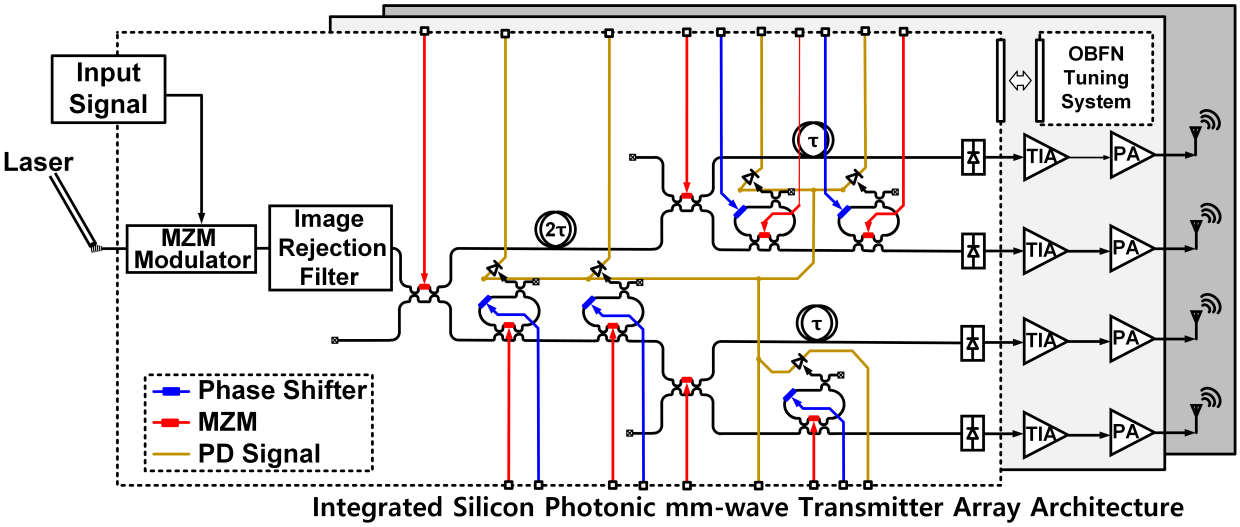

Figure 5.1: Conceptual integrated silicon photonic ORR-based mm-wave beamforming transmitter array.

ing control, but the discrete delays limit the beam scanning resolution. Another approach utilizes optical ring resonators (ORRs) as tunable delay elements, with a conceptual integrated silicon photonic mm-wave beamforming transmitter array that employs an ORR-based beamforming network shown in Fig. 5.1. ORR-based beamforming networks have been successfully demonstrated with different platforms [102, 103, 104, 105, 50, 106], and combinations of ORRs and switchable delay lines have also been shown to realize large delays with continuous tuning capability [107].

While ORR-based beamforming has the potential to allow for continuous tuning, this necessitates precise control of the ORRs. A major drawback of reported ORR-based beamforming networks is the difficulty of calibrating the original response in the presence of fabrication and temperature variations. Integrated heaters are most commonly utilized for tuning these structures via the thermo-optic effect. Current demonstrations are manually tuned and rely on output monitoring, which is time consuming and prone to human errors. Thermal crosstalk between phase shifters in the integrated photonic chips exasperate this process, often requiring simultaneous monitoring of each output with multiple optical vector network analyzers (OVNAs).

This paper presents a fully automatic monitor-based tuning algorithm for a 1X4 silicon photonic ORR-based asymmetric binary tree OBFN. Added drop ports and photodetectors in each ORR provide electrical information to automatically tune all OBFN outputs simultaneously. To the best of our knowledge, this is the first demonstration of automatic OBFN tuning with an integrated electrical monitoring approach. Building upon the scheme described in [108], this work demonstrates multiple successful calibrated results that correspond to different beam directions in a beamforming antenna array. Section II details the design of the ORR-based beamforming network that operates at 30GHz with 2GHz bandwidth and also introduces the automatic monitor-based tuning algorithm. Photonic device design and fabrication details are discussed in Section III. Section IV presents experimental calibration of the 1X4 silicon photonic ORR-based beamforming network and discusses the corresponding beam pattern of the antenna array. A discussion of thermal crosstalk, design optimization, and comparison with other silicon photonic beamforming networks is provided in Section V. Finally, Section VI concludes the paper.

5.2 True-time Delay Beamforming Network

5.2.1 Beamforming Network Design

As shown in Fig. 5.1, the proposed integrated silicon photonic beamforming system modulates a continuous-wave laser signal with the mm-wave signal, and the modulated optical signal propagates through the multiple-output optical circuit. Each optical output is then converted back to the electrical domain by a photodetector and transimpedance amplifier (TIA). Power amplifiers (PAs) follow to drive the antenna array to realize the desired transmit beam pattern. This beam pattern is determined by the group delay between the outputs, which is tuned in a continuous manner via the ORR-based photonic integrated circuit.

Fig. 5.2(a) shows a single ORR that has one phase shifter for resonance tuning and one MZI coupler for coupling ratio adjustment. Also, a 5% coupled drop port with a Germanium (Ge) waveguide photodetector (PD) is added to the ring for electrical monitoring purposes. Since a single ORR has one feedback path, it can be described as a digital infinite impulse response (IIR) filter whose response repeats with a free spectral range (FSR) period that is determined by the

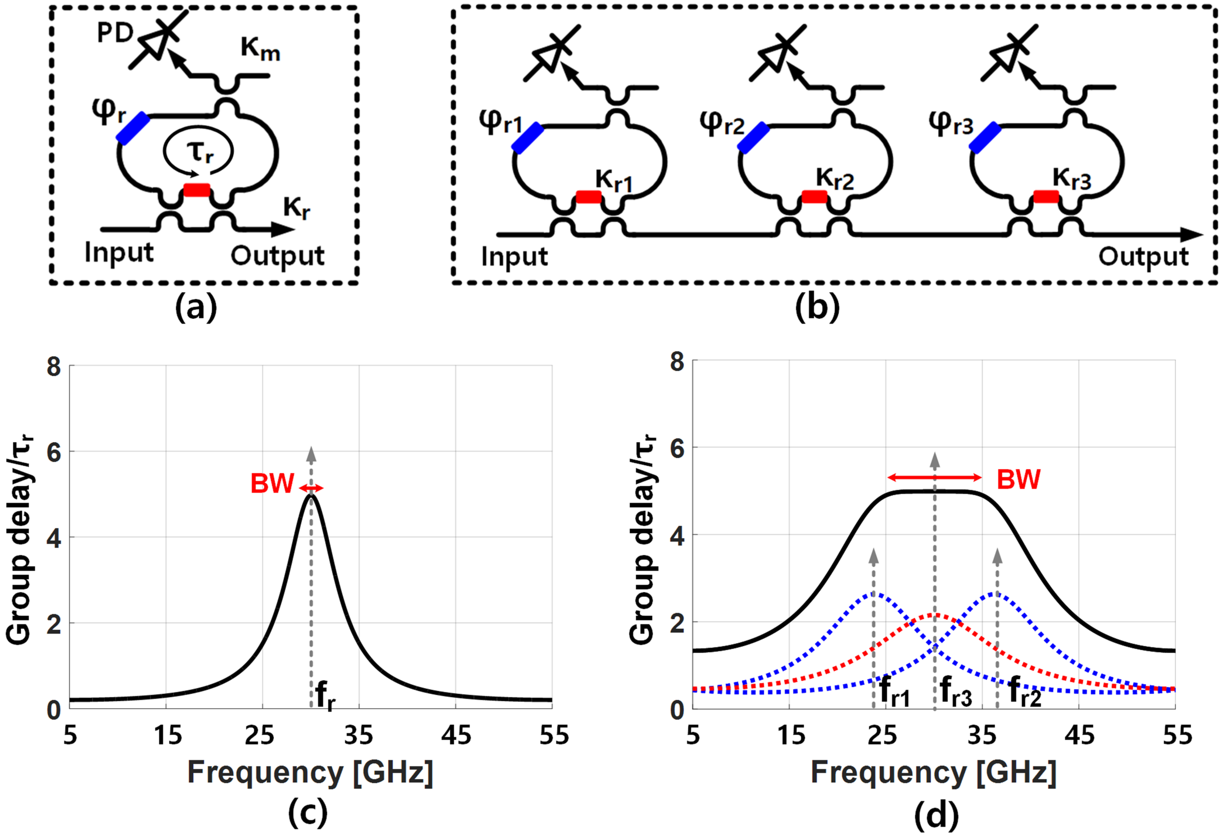

Figure 5.2: Schematic of (a) a single ORR and (b) three cascaded ORRs. Simulated normalized group delay responses of (c) a single ORR and (d) three cascaded ORRs centered at 30GHz. The rings have 50GHz FSR, 0.65dB round-trip waveguide loss, and 20ps round-trip delay.

ring circumference. The ORR output magnitude response shows a notch response that is centered at the resonance frequency (f_r), while the monitor magnitude response shows a complementary bandpass response. A single ORR group delay response (τ_g) is

$$\tau_g(f) = \frac{\kappa_r \tau_r}{r(2-\kappa_r) - (1+r^2)\sqrt{1-\kappa_r}\cos(2\pi f \tau_r + \phi_r)}, \tag{5.1}$$

where ϕ_r is the ring phase shift, κ_r is the ring MZI coupling ratio, τ_r is the round-trip delay, and r is the ring round-trip loss (RTL) [109]. The 2π phase shift limitation in one FSR period of a single ring resonator presents a strong trade-off where increased group delay results in dramatically reduced bandwidth, as shown in Fig. 5.3 [50]. Therefore, a single ORR can only provide a limited

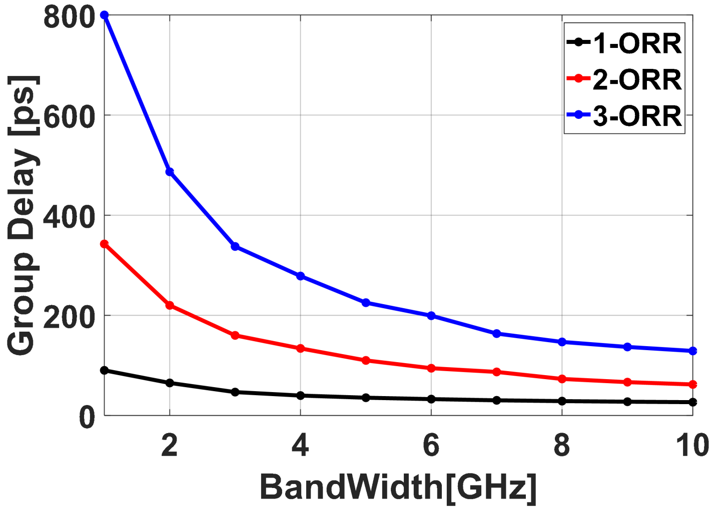

Figure 5.3: Simulated group delay versus bandwidth for a varying number of cascaded ORRs. Design conditions are group delay ripple<1.6ps, FSR=50GHz, and RTL=0.65dB.

bandwidth-group delay product, which limits its effectiveness for mm-wave signals (Fig 5.2(c)). This trade-off is broken by cascading multiple rings (Fig 5.2(b)), as the total group delay response ($\tau_{g,cascaded}$) is the summation of each ring's response ($\tau_{g,n}$).

$$\tau_{g,cascaded} = \sum_{n} \tau_{g,n} \tag{5.2}$$

Properly setting the coupling ratio ($\kappa_{r1,2,3}$) and resonance of each ring ($f_{r1,2,3}$) allows for an extended bandwidth with a large group delay (Fig. 5.2(d) and Fig. 5.3).

One issue with utilizing cascaded ORRs is that passband ripple is present in their combined group delay response, which can cause distortion in the mm-wave signal. Ripple reduction is achieved by adding more ORRs in a given bandwidth, such that their peaks are closer, or by reducing the peak delay [110]. By optimizing the coupling ratios and resonance frequency of each ORR, or by increasing the number of ORRs, this ripple can be reduced to arbitrarily small values [49]. The cascaded ORR group delay response for the targeted bandwidth, group delay, and ripple requirements can be optimized based on three criteria: delay, phase, or signal power [111]. This is done on a per-angle basis to set the optical component values, with the optimization that yields the

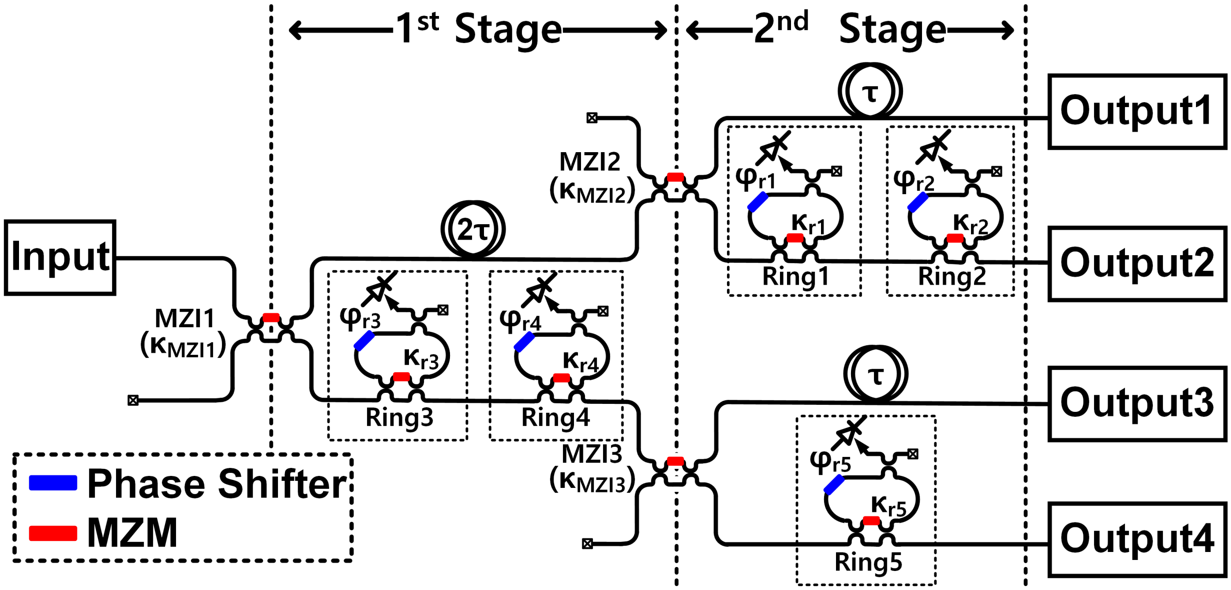

Figure 5.4: 1X4 ORR-based asymmetric binary tree OBFN schematic.

smallest mean-squared error (ε) from the ideal group delay response (D) utilized.

$$\varepsilon = \int_{BW} (\tau_g(f) - D)^2 df \tag{5.3}$$

The beamforming network presented in this paper optimizes the cascaded ring group delay response to allow 1.6ps ripple over a 2GHz bandwidth, which corresponds to a phase shift of $\pi/10$ for a 30GHz signal. This maximum $\pi/10$ phase error degrades array gain by less than 0.5dB [112].

Several ORR-based OBFNs have been reported, such as symmetrical and asymmetrical parallel structures and symmetrical and asymmetrical binary tree structures [113]. Parallel structures provide large degrees of freedom to generate arbitrary group delay responses. However, they have an increased ring resonator count relative to binary tree structures that share ORRs. Considering linearly increasing group delay requirements in an antenna array, binary tree structures are more efficient than parallel structures for similar group delay performance. Another consideration is symmetrical versus asymmetrical structures. Symmetric structures allow bi-directional beam-angle tuning that covers both negative and positive beam angles. However, they require twice the ORR count as asymmetric designs. A drawback with asymmetric structures is the requirement of

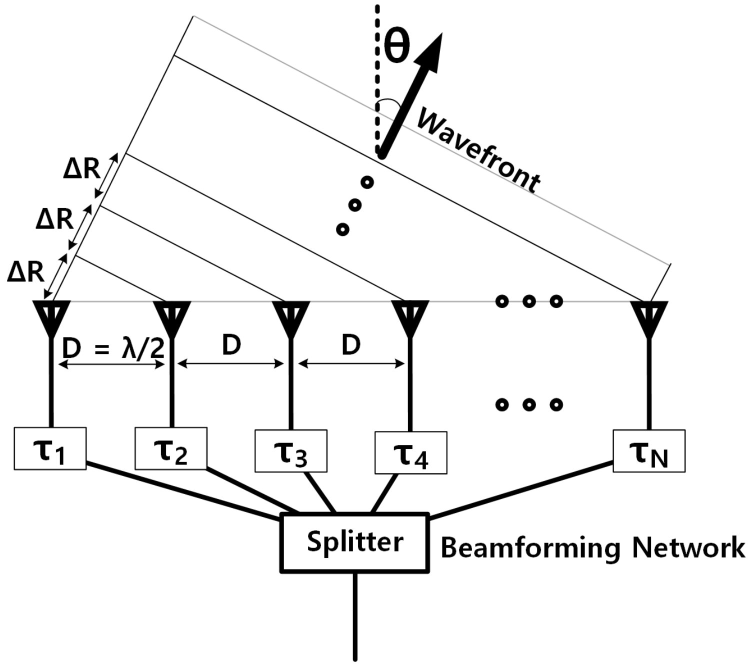

Figure 5.5: Conceptual transmitter antenna array with beamforming network.

an offset delay with additional waveguide length to cover the negative beam angles. However, the lower ORR count provides major reductions in automatic tuning algorithm complexity by reducing the number of tuning elements and the amount of thermal crosstalk. Thus, an asymmetrical binary tree OBFN structure that utilizes the minimum ring count is chosen for the automatic OBFN tuning demonstration.

Fig. 5.4 shows the 1X4 ORR-based asymmetric binary tree OBFN that was designed in this work. This structure saves ORRs by sharing Rings 3 and 4 in the Output 3 and 4 paths. Flexibility in beam tuning angle is achieved by utilizing waveguide delay lines in the design. In order to provide enough group delay response bandwidth, an additional Ring 2 is placed in the Output 2 path. One issue with this structure is that each ORR induces additional loss and each path experiences a different number of ORR, resulting in different output powers. This output power difference is compensated with tunable couplers (κ_{MZI1-3}) placed at each branch.

The OBFN is designed to work with a 30GHz ($\lambda \approx 1cm$) carrier frequency, have 2GHz bandwidth, and support a beam steering angle of 150° to 210°. Note, this is an identical pattern as -30°

Table 5.1: Output Group Delay (Wavegudie + ORR Delay) Requirements for Corresponding Radiating Angle at the Antenna Array

Radiating Angle (θ)	Output 1	Output 2	Output 3	Output 4
$\theta = 150^\circ$	0.0ps	25.0ps	50.0ps	75.0ps
	(0ps + 0ps)*	(-25.5ps + 50.5ps)	(-51.0ps + 101.0ps)	(-76.5ps + 151.5ps)
$\theta = 165^\circ$	0.0ps	29.0ps	58.0ps	87ps
	(0ps + 0ps)	(-25.5ps + 54.5ps)	(-51.0ps + 109.0ps)	(-76.5ps + 163.5ps)
$\theta = 180^\circ$	0.0ps	33.3ps	66.7ps	100.0ps
	(0ps + 0ps)	(-25.5ps + 58.8ps)	(-51.0ps + 117.7ps)	(-76.5ps + 176.5ps)
$\theta = 195^\circ$	0.0ps	37.6ps	75.3ps	112.9ps
	(0ps + 0ps)	(-25.5ps + 63.1ps)	(-51.0ps + 126.3ps)	(-76.5ps + 189.4ps)
$\theta = 210^\circ$	0.0ps	41.6ps	83.3ps	124.9ps
	(0ps + 0ps)	(-25.5ps + 67.2ps)	(-51.0ps + 134.3ps)	(-76.5ps + 201.4ps)

*Group delay (path delay + ORR delay)

to 30° for a linear isotropic antenna array with $\lambda/2$ separation (D) (Fig. 5.5). For a certain beam radiation angle (θ) at the antenna array, the distance between the same phase wavefront (ΔR) is defined as $\Delta R = Dsin\theta$ and the required delay between the two adjacent OBFN outputs ($\Delta\tau$) is $\Delta\tau = Dcos\theta/c$. In order to meet the specifications, the nominal unit path delay τ is 25.5ps for the 1X4 OBFN structure. Table 5.1 summarizes the delay requirements for the asymmetric binary tree OBFN outputs to cover the targeted beam steering angle range. Assuming 0.65dB ring round trip loss and designing for a 50GHz FSR relative to the 1550nm laser wavelength, Table 5.2 summarizes the optical component values extracted from the optimization procedure. A single ORR can provide enough bandwidth for the Output 2 response for radiating angles of 150° to 195°, and thus the Ring 2 coupling ratio is set to zero. However for a radiating angle of 210°, a single ORR with 67.2ps peak delay cannot provide the required 2GHz bandwidth. Thus, Ring 2 is activated in cascade with Ring 1 to expand the group delay bandwidth. The simulated OBFN output magnitude and group delay responses for the targeted radiating angles (θ) at the antenna array are shown in Fig. 5.6. Including $MZI1-3$ allows for equal output power over the 2GHz bandwidth for the entire beam angle range.

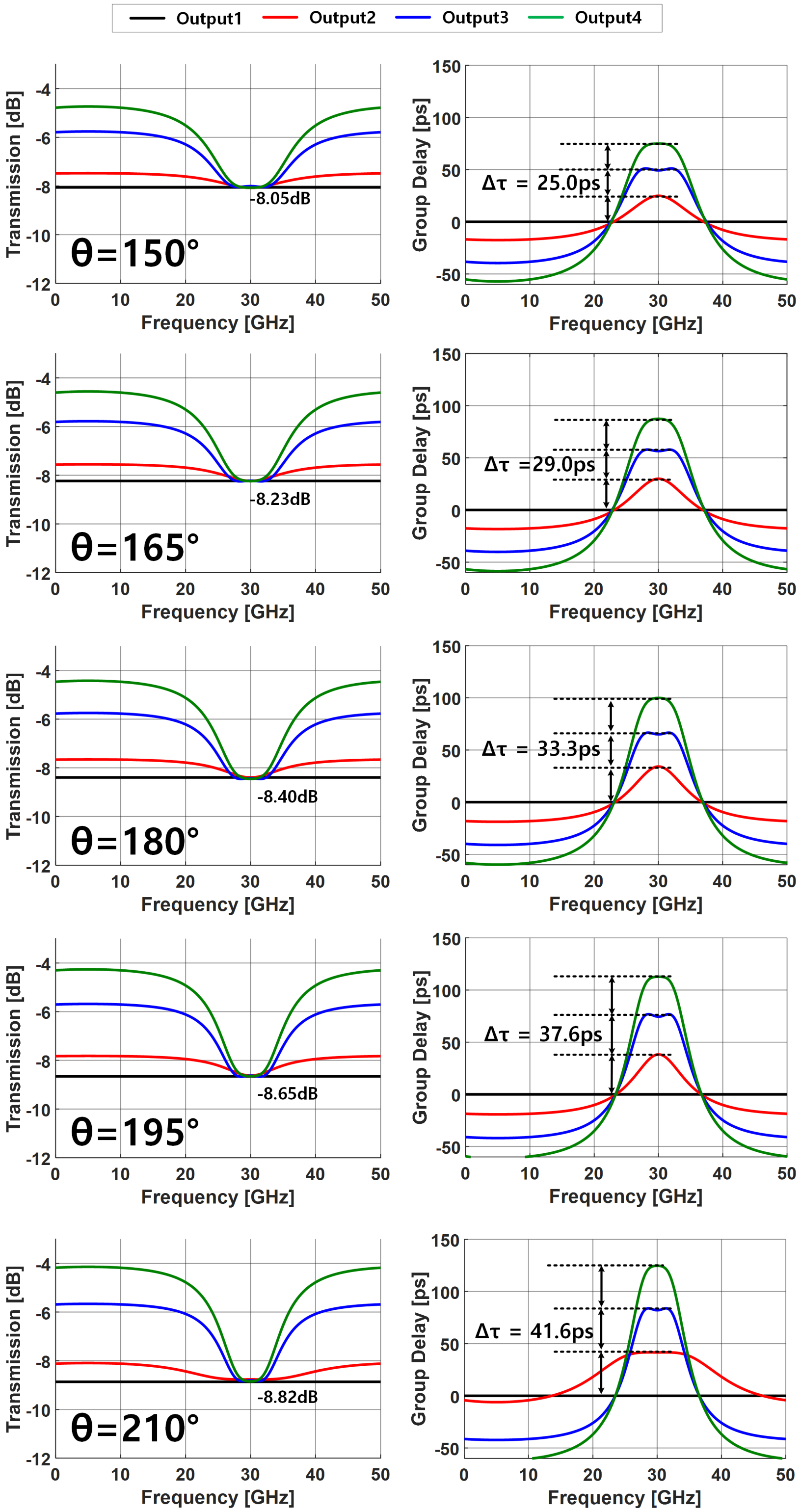

Figure 5.6: Simulated OBFN magnitude and group delay response as the radiating angle varies from 150°to 210°from the assumed linear antenna array with isotropic antenna elements.

Table 5.2: Designed OBFN Component Values for the Corresponding Radiating Angle (θ) at the Antenna Array

Radiating Angle (θ)	ORR Coupling Ratio				ORR Phase Shift (rad)					MZI Coupling Ratio		
	κ_{r1}	κ_{r2}	$\kappa_{r3,4}$	κ_{r5}	ϕ_{r1}	ϕ_{r2}	ϕ_{r3}	ϕ_{r4}	ϕ_{r5}	κ_{MZI1}	κ_{MZI2}	κ_{MZI3}
150°	0.810	0	0.680	0.810	3.769	3.769	3.386	4.152	3.769	0.660	0.540	0.570
165°	0.780	0	0.660	0.775	3.769	3.769	3.417	4.121	3.769	0.670	0.545	0.575
180°	0.753	0	0.630	0.750	3.769	3.769	3.445	4.093	3.769	0.680	0.548	0.580
195°	0.728	0	0.595	0.730	3.769	3.769	3.469	4.069	3.769	0.695	0.553	0.590
210°	0.859	0.859	0.580	0.703	3.191	4.347	3.490	4.048	3.769	0.705	0.556	0.595

5.2.2 Tuning Algorithm

5.2.2.1 Monitor-based single ring group delay tuning

Tuning of the OBFN involves adjusting each ORR's group delay, which is a function of the ring's coupling ratio and phase shift. Each ring employs a tunable MZI coupler and phase shifter to achieve this (Fig. 5.2(a)). As shown in Fig. 5.7, the ORR resonance frequency(f_r) is adjusted by tuning the phase shifter (ϕ_r) and the depth of the output port notch response is determined by the coupling ratio (κ_r). The ring's monitor port shows a complementary bandpass response with the peak at the same resonance frequency. This relationship is utilized in our previous monitor-based tuning work [65, 67, 68, 66] to set the desired ORR magnitude response in the presence of deviated coupling ratio and resonance frequency due to process and temperature variations. This approach is modified in this work to allow for monitor-based ORR group delay tuning.

In order to utilize monitor-based tuning, the group delay response should be mapped to the monitor response. As can be seen in Fig. 5.7, both the ORR group delay and monitor output display similar bell-shaped responses centered at the ORR resonance frequency. Thus, calibrating the monitor's peak output will also set the peak of the ORR group delay to the desired frequency. Since the monitor response is maximized when the ORR resonance frequency corresponds to the input laser frequency/wavelength, maximizing the monitor signal while tuning the phase shifter (ϕ_r) allows for tuning the ring to the targeted resonance frequency.

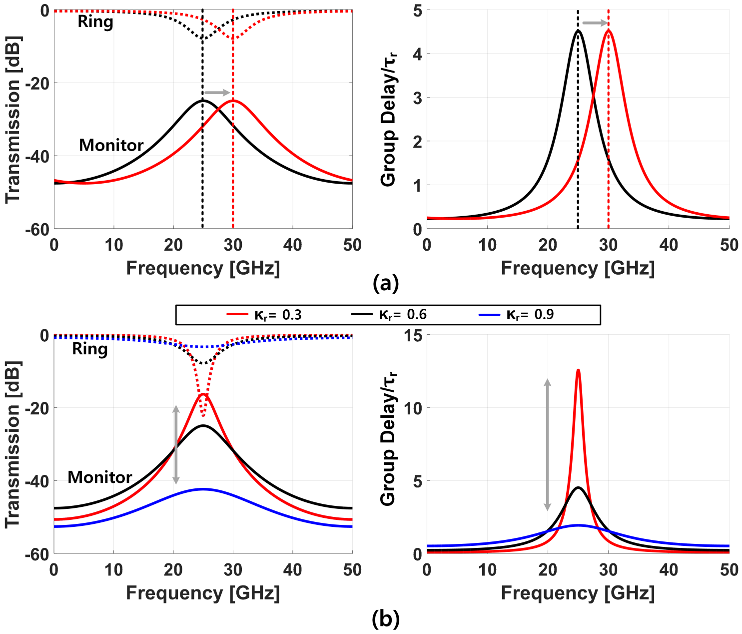

Figure 5.7: Simulated ORR output magnitude, monitor, and group delay responses with (a) phase shifter (ϕ_r) tuning and (b) MZI coupler (κ_r) tuning.

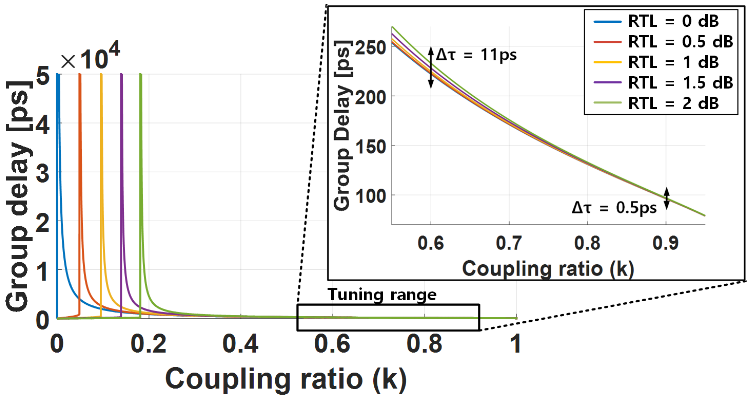

Figure 5.8: Simulated single ORR group delay response with different round trip loss values.

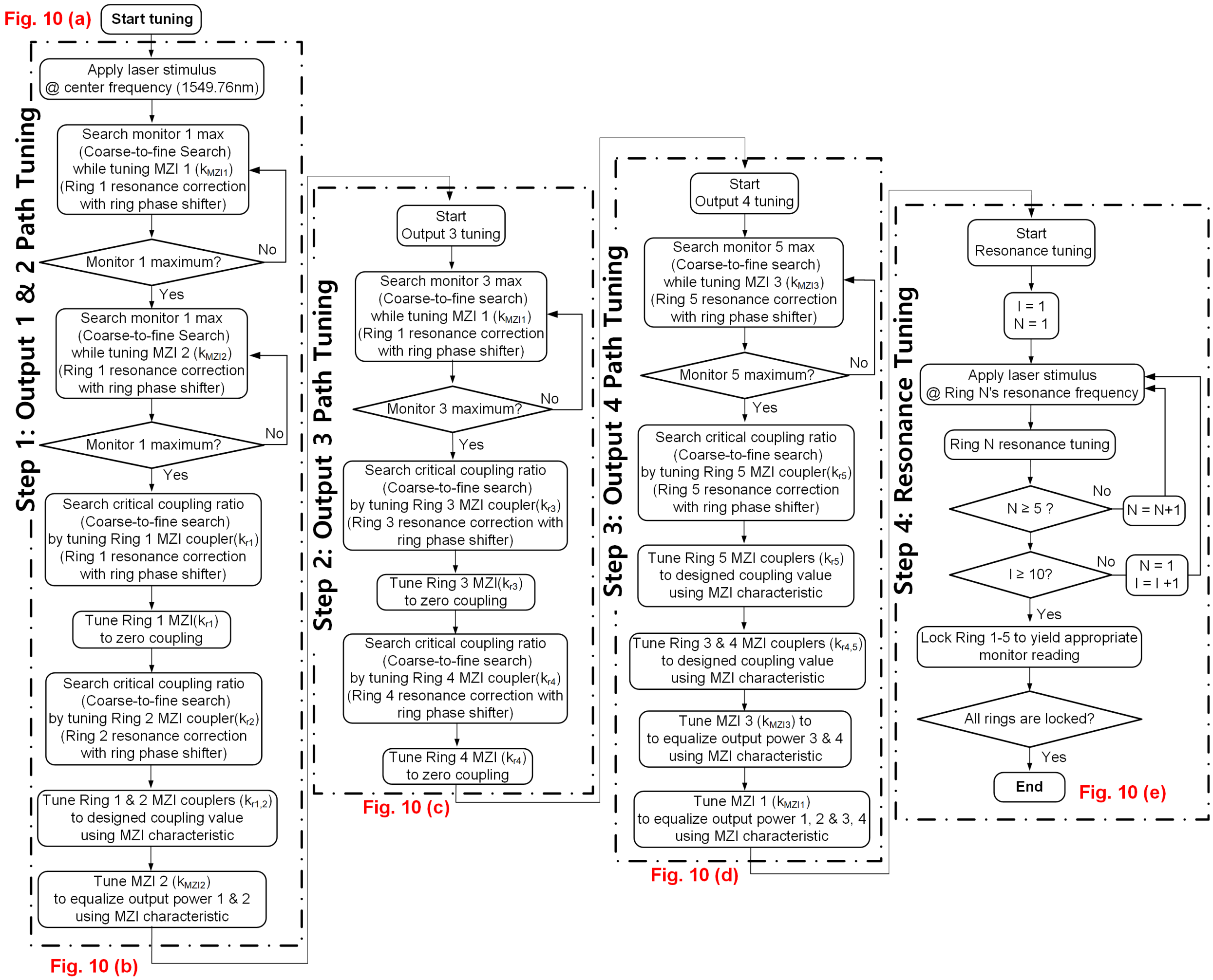

Figure 5.9: 1X4 OBFN calibration algorithm flowchart.

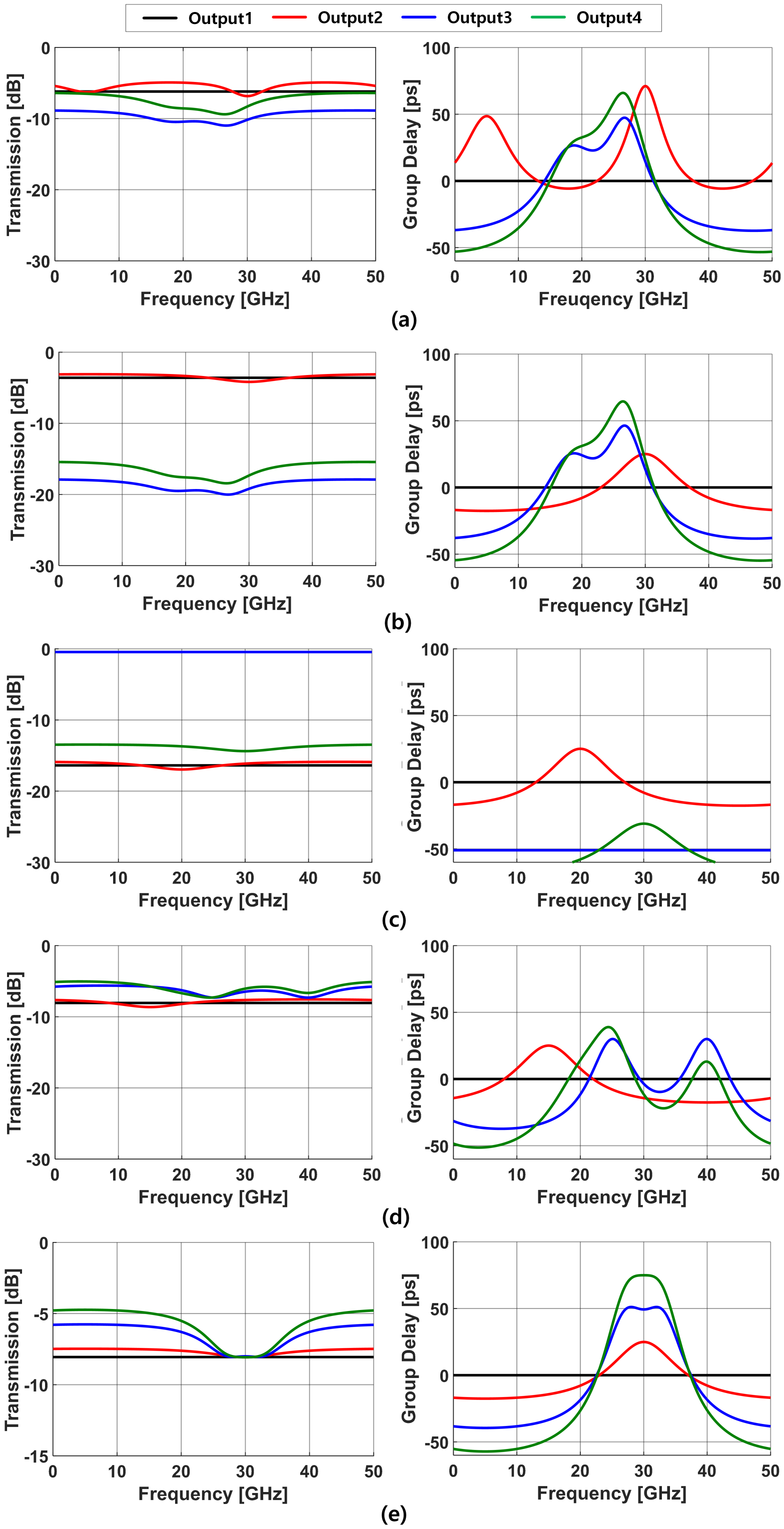

Figure 5.10: Simulated OBFN output transmission and group delay responses for a radiating angle of 150° at the antenna array: (a) the initial response with process variations, (b) after Output 1 & 2 tuning, (c) after Output 3 tuning, (d) after Output 4 tuning, and (e) after ring resonance tuning.

As shown in Fig. 5.8, decreasing the coupling ratio from a large value monotonically increases the maximum ORR group delay at the resonance frequency until critical coupling is achieved. The ring's RTL sets the critical coupling ratio and affects the group delay slope, such that a larger spread is observed as the group delay increases. This necessitates careful characterization of a ring's RTL. Note that this work lumps the 5% monitor coupling in the proposed ORR structure as part of the RTL. While the ORR coupling ratio can theoretically be tuned from 0 to 1, process variations of the directional coupler used in the MZI structure prohibit achieving a maximum coupling ratio of 1 and set a practical minimum ORR group delay. Also, the group delay experiences a very steep reduction for values less than critical coupling. Thus, the coupling ratio range is restricted to tune between 0.5 and 0.9 in the presented OBFN design.

Monitor-based ORR coupling ratio tuning [65, 67] is applied to achieve the targeted group delay. A tuning reference point is first set by finding the critical coupling ratio where the monitor response is maximized. The ORR sinusoidal MZI coupler response is then used to tune to the desired coupling ratio [65]. However, thermal crosstalk in the MZI coupler tuning process shifts the ORR's resonance frequency. This is compensated by adjusting the ring phase shift (ϕ_r) in parallel to correct the resonance frequency. This tuning procedure is valid for narrowband operation around a nominal center wavelength (1550nm). Also, due to the wavelength-dependency of the directional coupler, recalibration should be performed to operate at a different resonance frequency.

5.2.2.2 Complete Beamforming Network Tuning Procedure

Based on the single ORR group delay tuning principle, a monitor-based automatic tuning algorithm is proposed to calibrate the complete OBFN response. Fig. 5.9 shows the flowchart for automatic tuning of a 1X4 OBFN, where each output response is set by individual tuning of a specific ring through monitoring its drop port response. This algorithm is verified in MATLAB utilizing a 1X4 OBFN model and pre-characterized ORR RTL and MZI coupler V_π values.

Step 1 - Output 1 $\&$ Output 2 Path Tuning: Process variations cause the optical component values to initially deviate from the designed values in Table II, resulting in significantly distorted responses at the four output ports (Fig. 5.10(a)). Referring to Fig. 5.4, the Output 1 and 2 ($\kappa_{r1,2}$,

$\kappa_{MZI1,2}$) paths are calibrated first utilizing the desired center wavelength/frequency laser stimulus (1549.76 nm). This single laser input is split amongst the four outputs through MZI 1, 2 and 3 ($\kappa_{MZI1,2,3}$). Given that it is important to maximize the monitor SNR in order to improve the coupler tuning accuracy, MZI 1 and 2 are first tuned to maximize the Output 2 power. This is achieved by tuning MZI 1 and 2 to maximize the Monitor 1 response. A course-to-fine search algorithm is used to find this maximum point rapidly with 11-bit resolution. During MZI 1 and 2 tuning, the resonance of Ring 1 shifts due to the thermal crosstalk. To correct this error, Ring 1 resonance tuning is performed in parallel with MZI 1 and 2 coupler tuning. After maximizing the Output 2 power and storing $\kappa_{MZI1,2}$, the Ring 1 MZI coupler κ_{r1} is tuned to the critical coupling ratio by maximizing the Monitor 1 signal. A course-to-fine search algorithm is also used in this step, along with resonance tuning of Ring 1 being performed in parallel. After saving the Ring 1 critical coupling ratio, the Ring 2 critical coupling ratio is then obtained. Given that Ring 1 and 2 are cascaded in the Output 2 path, the Ring 2 monitor response is affected by the previous Ring 1 response. To address this issue, Ring 1 is tuned to zero coupling by using the saved critical coupling ratio and the MZI sinusoidal characteristic. Then, the Ring 2 MZI coupler is tuned to the critical coupling ratio by maximizing the Monitor 2 response. In parallel, resonance tuning of Ring 2 is performed. After finding both Ring 1 and 2 critical coupling ratios, this reference point and the MZI sinusoidal characteristic is utilized to tune both rings' MZI couplers to their desired ratios for a given beam angle. Finally, MZI 2 is tuned to equalize the Output 1 and 2 power using the MZI characteristic. Fig. 5.10(b) shows the simulated OBFN response after Step 1 for a 150° angle. While Outputs 1 and 2 are now close to the desired group delay and have near equal power, Outputs 3 and 4 are still highly distorted.

Step 2 - Output 3 Path Tuning: The critical coupling values of Rings 3 and 4 in the Output 3 path are obtained in this step. Following the same procedure as Step 1, MZI 1 is first tuned to maximize the Monitor 3 and 4 readings. Note that since Rings 3 and 4 are placed before MZI 3, the tuning of this MZI is not necessary. The Ring 3 and 4 MZI couplers are then tuned to find the critical coupling settings. Similar to Step 1, the Ring 3 MZI coupler is tuned to zero coupling temporarily during the Ring 4 coupler tuning. After obtaining the critical coupling values of Ring 3 and 4, both of the ORRs' coupling ratios are then tuned to zero coupling in order to tune Ring 5 in the next step. Fig. 5.10(c) shows the simulated OBFN response after this intermediate Step 2, with the Output 3 group delay response now showing a flat response due to both Rings 3 and 4 coupling ratios being set to zero coupling in preparation for Step 3. Also, note that the Ring 2 center frequency has shifted due to thermal cross-talk and must be corrected later.

Step 3 - Output 4 Path Tuning: The critical coupling values of Ring 5 in the Output 4 path are obtained in this step, along with setting the desired coupling ratios of Rings 3-5 and optimizing the MZI 1 and 3 coupling values. First, MZI 3 is tuned to maximize the Monitor 5 reading for accurate calibration. Then, the Ring 5 MZI critical coupling ratio is obtained by maximizing the Monitor 5 signal. Now that the critical coupling values of Rings 3-5 have been stored, these coupling ratios are then adjusted to the desired values using the MZI sinusoidal characteristic. Finally, MZI 1 and 3 are tuned to the desired values to equalize the whole OBFN output powers. Fig. 5.10(d) shows the simulated OBFN response after Step 3. While the output powers are now closer, they are not exactly the same and the group delays are still off due to the ring's resonance frequencies not being set to their final values.

Step 4 - Resonance Tuning: The final step is OBFN resonance tuning to set the group delay center frequency and bandwidth. Rings 1-5 are resonance tuned in order by adjusting the individual ring's phase shifter (ϕ_{r1-5}) to maximize the monitor reading with the laser input wavelength/frequency switched to the corresponding ideal f_r. Since resonance tuning is sensitive to thermal crosstalk, multiple iterations are performed across the rings. Fig. 5.10(e) shows that after this final tuning step the OBFN's four outputs have well-defined group delay responses and equalized power around the 30GHz center frequency.

5.3 Device Design and Fabrication

The presented automatic OBFN tuning algorithm is demonstrated using a 1X4 asymmetric binary tree structure fabricated in the IME A*STAR baseline Si photonics process that utilizes SOI wafers. As shown in the die micrograph of Fig. 5.11(a), the OBFN structure occupies 4575μm

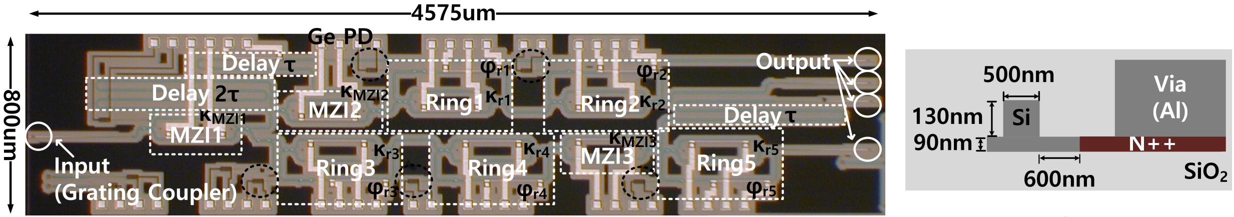

(a)

(b)

Figure 5.11: (a) OBFN chip micrograph of the OBFN. (b) Cross-section schematic of the rib waveguide with resistive heater.

× 800μm. Rib waveguides are employed to minimize propagation loss. They are designed with a 220nm total slab height, that has a 90nm thick partially-etched strip, and a 500nm width silicon core surrounded by SiO_2 cladding (Fig. 5.11(b)). In order to achieve a nominal unit delay (τ) of 25.5ps, 1981.4μm additional waveguide length is added to the appropriate paths. 1-D grating couplers with a center frequency around 1550nm are placed at the OBFN input and output ports. The OBFN's ORRs are designed with 1554μm ring circumference to achieve a 50GHz FSR and have a rounded rectangular shape with 25μm radius corners to minimize area and waveguide propagation loss. The ORR drop port monitors are designed for 5$\%$ coupling and are terminated with waveguide Ge p-i-n PDs. N-doped thermo-optic phase shifters are implemented 0.6μm away from the sidewall of the waveguide slab to minimize optical loss. These thermal phase shifters provide tunability over the full FSR range. Directional couplers with a 200nm gap are employed throughout the OBFN structure, with the couplers in the tunable MZI structures having a nominal 50$\%$ coupling ratio. Metal bondpads are placed at the top and bottom edges of the photonic integrated circuit (PIC) to electrically control the phase shifter heaters and provide the bias and electrically monitor the drop-port PD signals. In order to reduce the amount of thermal crosstalk between the thermo-optic phase shifters, the default silicon substrate thickness of 750μm is thinned to 75μm with an additional CMP process. This reduces the thermal time constant and results in a dramatic improvement in tuning speed [65].

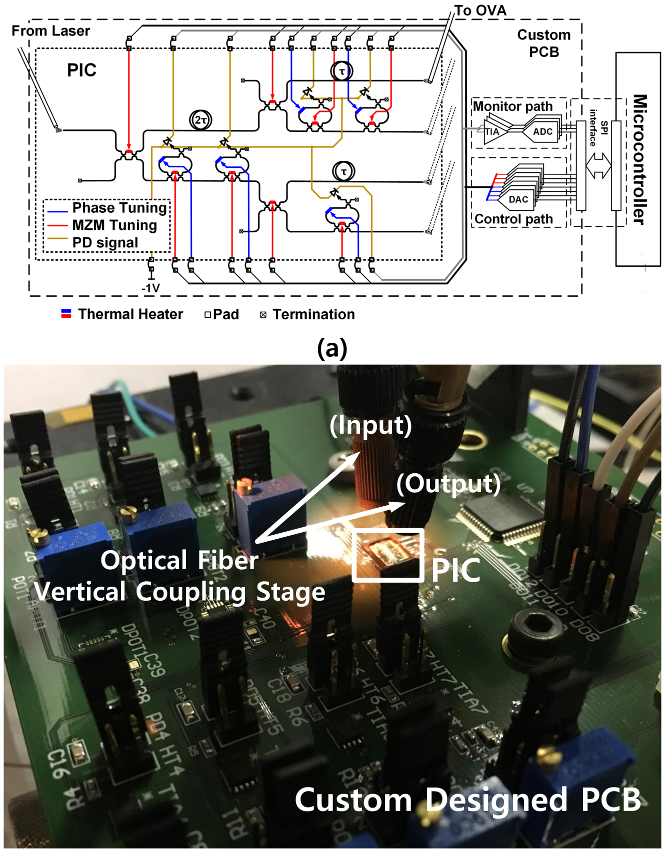

(a)

(b)

Figure 5.12: Automatic monitor-based tuning system: (a) block diagram with the OBFN and (b) photograph of the system with the optical fiber vertical coupling stage.

5.4 Experimental Results

5.4.1 Measurement Setup

The OBFN automatic monitor-based tuning system block diagram and a picture of the measurement setup is shown in Fig. 5.12. A free-space optical fiber coupling stage couples a tunable laser (Luna Phoenix 1400) into the PIC. This tunable laser generates the five wavelengths required for calibration that correspond to each ORR resonance. The PIC is wire-bonded to the custom-designed printed circuit board (PCB) that includes low-bandwidth transimpedance amplifiers (TIAs) using op-amps (OPA727) and 12-bit analog-to-digital converters (ADCs) (Arduino Due internal ADC) to sense the average photocurrent from the OBFN ORR's monitor waveguide Ge PDs that are biased at -1V. These ADCs interface with a microcontroller (Arduino Due) that implements the OBFN tuning algorithm by controlling 16-bit digital-to-analog converters (DACs) (LTC2668) through a serial peripheral interface (SPI). The DACs apply control voltages across the resistive heaters on the PIC to adjust the optical phase shifters. A fully-automated tuning system is achieved with the tunable laser also controlled by the same microcontroller. The PIC is placed on a large metal footprint with thermal vias down to the bottom layer of the PCB where a thermoelectric cooler (TEC) is placed with thermal grease passivation to provide temperature stabilization.

An optical vector network analyzer (OVNA) signal is coupled into the PIC for device characterization and verification of the calibrated OBFN group delay and magnitude responses. The OBFN output group delay responses are obtained using the OVNA time domain response at the corresponding outputs. Since group delay is sensitive to noise, digital filtering over 40 samples and time domain windowing are used [114]. Each ORR in the OBFN structure is characterized independently by configuring zero coupling for the other rings. A Jones matrix method that employs a time domain impulse response of the ORR and its corresponding transfer function is utilized to extract accurate RTL values. From the ORR's Jones matrix [83], a 0.65dB (± 0.1dB) RTL and 0.3963 nm (49.64GHz) FSR is determined. These characterized round trip loss measurements are used to determine the ORR critical coupling values and to model the group delay response.

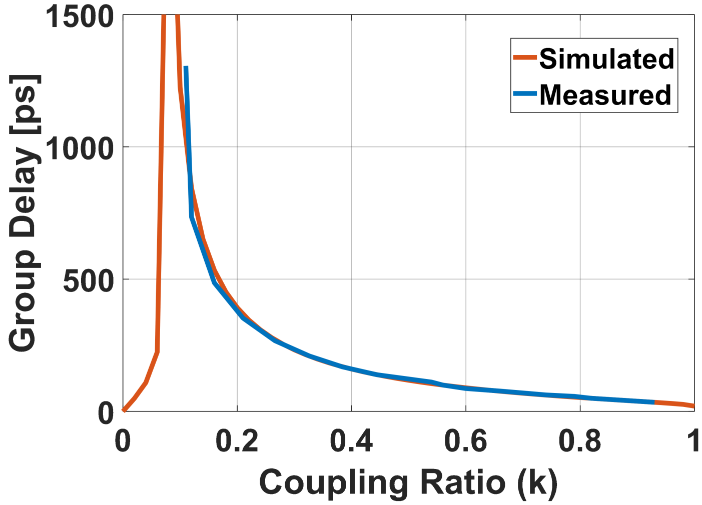

Figure 5.13: Measured single ORR group delay response vs coupling ratio.

5.4.2 Single ORR Measurement

Accurate OBFN automatic tuning requires initial characterization of the ORRs. To characterize a specific ring resonator, the other cascaded ring resonators' coupling ratio are set to zero to remove their response seen at the output. One issue is that the ORR resonance drifts slightly when tuning the coupler due to the varying phase shift of the MZI coupler and thermal crosstalk [106]. This is compensated by performing resonance tuning in parallel with the ORR coupler tuning [65]. Fig. 5.13 shows the measured ORR group delay response versus ORR coupling ratios, which shows good agreement with simulations utilizing 0.65dB round-trip loss. Theoretically, the ORR coupling ratio can vary from 0 to 1 by tuning the thermal phase shifter (κ_r) of the corresponding MZI coupler. However, fabrication variations of the 50$\%$ couplers present in the MZI coupler limit the coupling ratio tuning range to a maximum of 0.93. Neglecting the dramatically-changing group delay region with low coupling ratios, this limits the minimum achievable OBFN group delay response to 34.5ps. Overall, the good agreement between the measured and simulated group delay response versus coupling ratio validates that the monitor-based tuning approach can precisely set a desired group delay during the full OBFN tuning procedure.

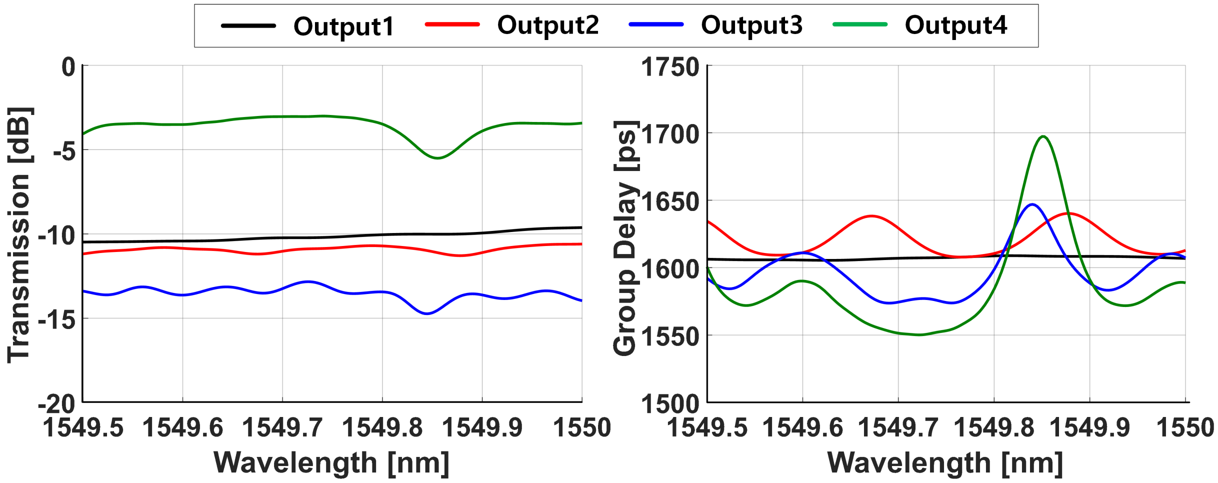

Figure 5.14: Measured 1X4 OBFN initial responses.

5.4.3 Full OBFN Tuning

The proposed OBFN tuning algorithm is demonstrated with the 1X4 asymmetric binary tree OBFN structure. Fig. 5.14 shows that the fabricated device's initial output responses have significant variation in output magnitude and severely deviate from the designed group delay responses. Before tuning to a specific angle, the OBFN path delays are first characterized by setting all the ORR coupling ratios to zero and maximizing the output power by tuning the MZI couplers ($\kappa_{MZI1,2,3}$). OVNA measurements show that, after normalizing for 9dB of input/output grating coupler insertion losses, the OBFN displays 1.1dB of combined tunable coupler and waveguide propagation loss (Fig. 5.15). This magnitude response varies by ±0.1dB due to grating coupler fabrication variations, fiber alignment error, and limitations in the achievable MZI coupler ratios. These MZI coupler limitations, which are due to the 50$\%$ directional coupler imperfections, are corrected through the coupler tuning algorithm [67, 68]. The measured group delays of the output paths display close to the nominal 25.5ps spacing.

Utilizing the 1549.76nm center wavelength (30GHz away from 1550nm) and four additional wavelengths (Table 5.3) derived from the tunable laser, the OBFN tuning algorithm is applied and well-defined group delay responses are observed as the angle is tuned from 150° to 210° (Fig.

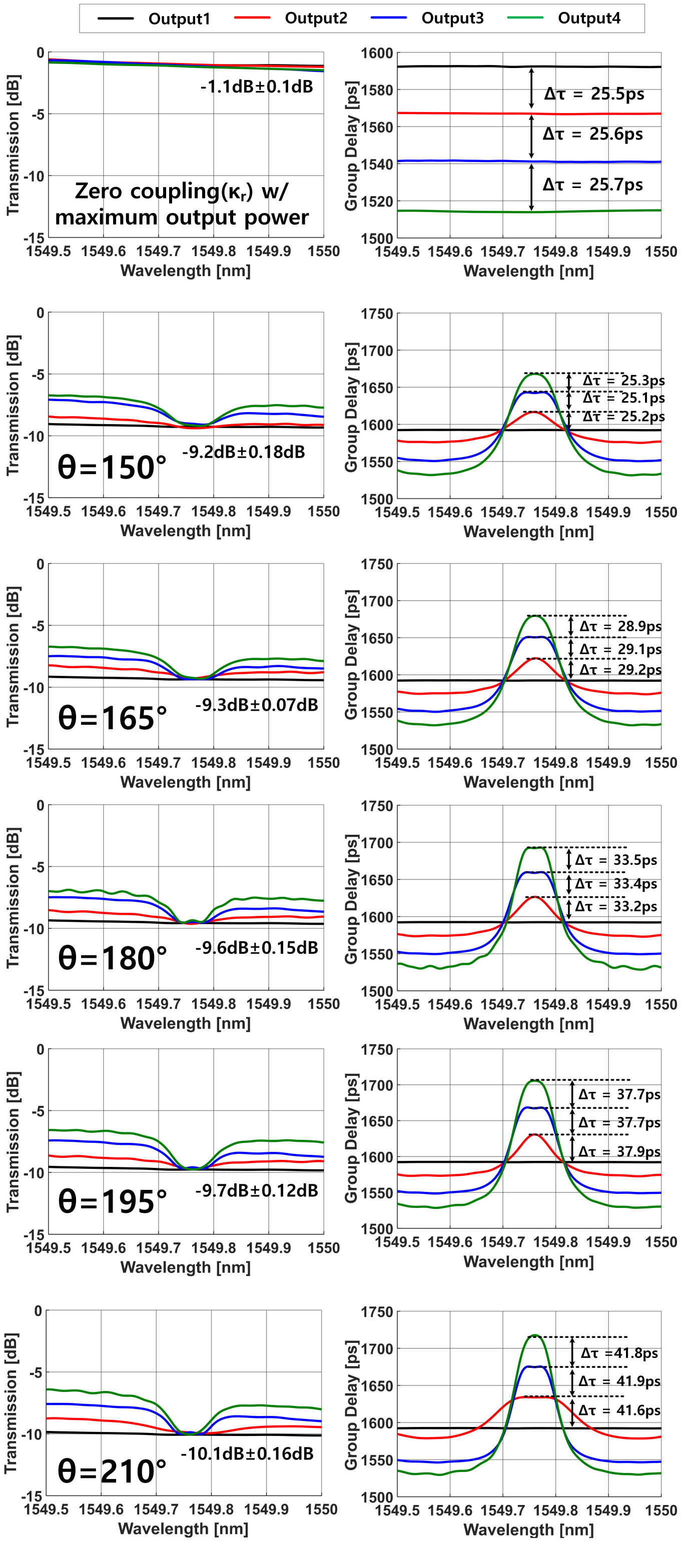

Figure 5.15: Measured automatically-tuned OBFN magnitude and group delay response for an initial flat configuration and as the radiating angle varies from 150° to 210°.

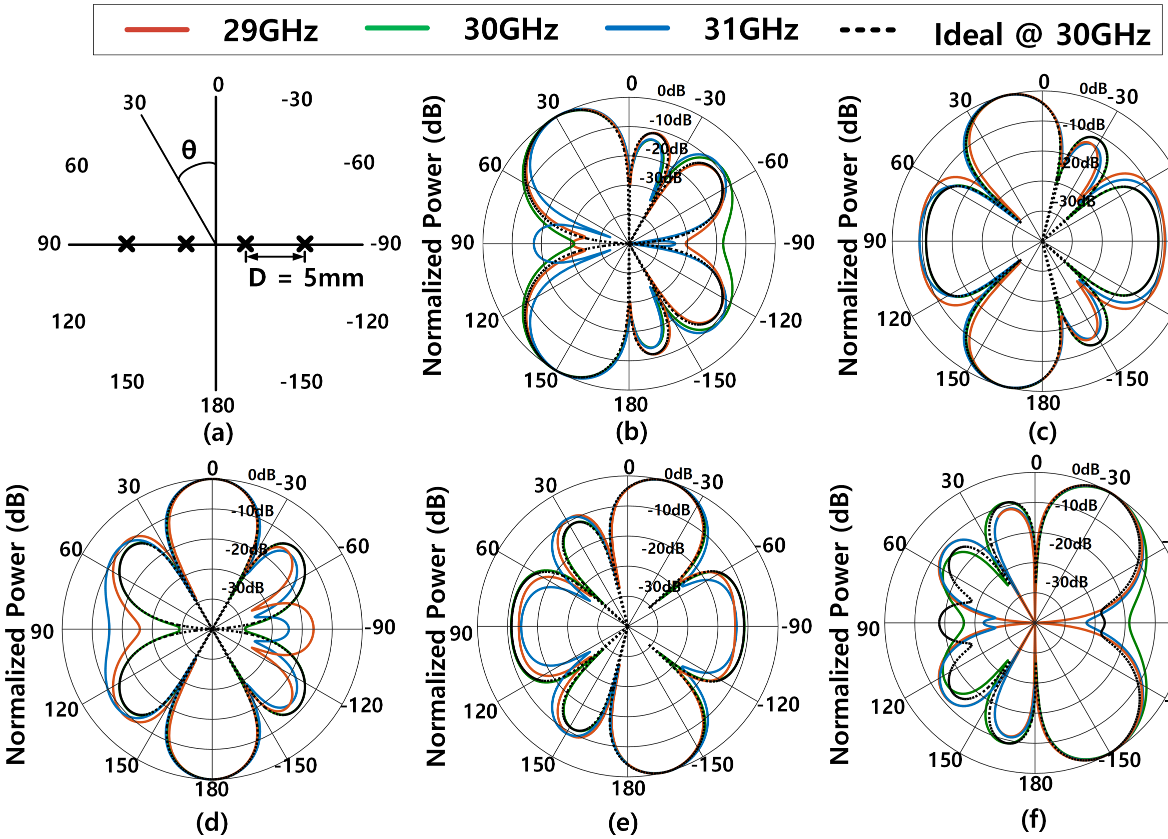

Figure 5.16: Simulated linear array beam patterns based on measured automatically-tuned OBFN output responses: (a) Assumed linear array. Radiating angles at (b) 150° (30°), (c) 165° (15°), (d) 180° (0°), (e) 195° (-15°), and (f) 210° (-30°).

Table 5.3: Input Laser Wavelengths Utilized in Full OBFN Tuning

Radiating Angle(θ)	Wavelength (nm)				
150°	1549.76	1549.784	1549.735		
165°	1549.76	1549.782	1549.737		
180°	1549.76	1549.781	1549.739		
195°	1549.76	1549.779	1549.740		
210°	1549.76	1549.775	1549.742	1549.797	1549.723

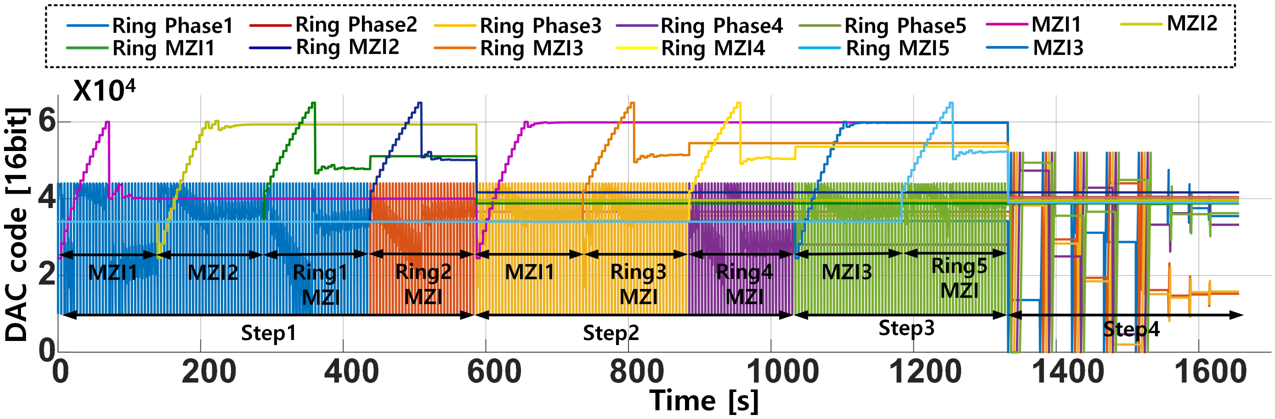

Figure 5.17: 1X4 OBFN automatic tuning convergence for a 210° radiating pattern.

5.15). The calibrated OBFN group delay responses show errors less than ±0.3ps, with the smallest 2.02GHz (16.2pm) bandwidth occurring at Output 2 with a 195° radiating angle. For a given angle, the proposed algorithm equalizes the output power levels to have less than ±0.2dB variation. Note that only the largest 210° angle requires all five input tuning wavelengths due to this angle's group delay values requiring activation of Ring 2. All the other angles have zero coupling for Ring 2 and only require three tuning wavelengths.

Further insight on the measured OBFN group delay responses is possible by simulating the radiating beam patterns of a 4 element linear isotropic antenna array in MATLAB. As shown in Fig. 5.16, the linear array has 5mm spacing and operates over a 29-31GHz frequency band with

Table 5.4: Integrated OBFN Comparison Table

	This work	[50]	[106]	[115]
Operating Frequency	29 - 31GHz	10.7 - 12.75GHz	75 - 100GHz	-
Platform	SOI	Silicon Nitride (TriPleX)	Silicon Nitride	Silicon Nitride
Laser Wavelength	1550nm	1550nm	1550nm	1550nm
OBFN Type	TX	RX	TX	TX
Input×Output	1×4	8×1	1×4	2×2
Delay Element	5 ORR	8 ORR	8 ORR	Delay line + Swtich
FSR	50GHz	15GHz	22GHz	-
Structure	Asymmetric binary tree	Asymmetric binary tree	Symmetric binary tree	Swtch matrix
Tuning Resolution	Continuous	Continuous	Continuous	4 bit
Delay Range	36 - 200 (ps)	40 - 600 (ps)	8.7 - 209 (ps)	0 - 12.35 (ns)
RF Bandwidth	2GHz	1GHz	6GHz	-
Automatic Calibration	Y	N	N	N

good agreement in main lobe directionality and power within 0.1dB of the ideal OBFN response. While the sidelobes are slightly increased relative to the ideal case due to the group delay ripple and residual magnitude error, the main lobe maintains at least a 9.5dB larger response over the maximum sidelobe for all angles. The true time-delay operation of the ORRs allows for squint-free operation, with the same radiating angle achieved over the 29-31GHz band.

For each radiating angle, the OBFN automatic tuning process involves the calibration of 13 heaters for ORR and MZI coupler tuning and takes 1617s to complete. As shown in the measured DAC plots for a 210° radiating pattern (Fig. 5.17), each of the four tuning steps show good convergence. This is achieved by tuning the corresponding ring phase shifter in parallel to track the monitor reading during the MZI coupler tuning procedure. The individual DAC codes are stored for each radiating angle during this initial calibration procedure. Subsequent rapid switching between the different angles is achieved by simply recalling these stored DAC codes, with this process only limited by the 300ms measured heater cooling time [65].

5.5 Discussion

Table 5.4 summarizes the integrated silicon photonic OBFN performance and compares it with other implementations. This work targeted a potential 5G application that utilizes a 30GHz carrier frequency and achieves a higher RF bandwidth than the other asymmetric binary tree design [50]. Relative to the ORR-based symmetric binary tree design [106], it utilizes fewer ORRs. Also, the proposed OBFN allows for continuous tuning at a much higher resolution than the 4-bit delay line implementation [115]. Overall, the presented approach is the first and only design to offer fully automatic calibration of the OBFN group delay response and output power.

There are several areas of improvement possible in future implementations of the proposed OBFN. The current design has a single ORR minimum achievable group delay response that is limited to 34.5ps, while the path delay is designed at 25.5ps. In order to achieve the -30 °to 30 °radiating angles at the antenna array, large group delay responses are set at the cost of some bandwidth. Considering the minimum group delay requirements, this can be improved by simply increasing the path delay to 43ps. This will extend the OBFN bandwidth by 36$\%$ by reducing the required ORR group delay from 201.5ps to 142.9ps. Another observation is that $\tau_{output4} > \tau_{output3} > \tau_{output2} > \tau_{output1}$ for the asymmetric binary tree OBFN structure to cover the same radiating angle at the antenna (Table 5.1). This design achieved this with more identical ORRs in a particular path to achieve a larger delay. In order to have a larger bandwidth, the ORRs can be further optimized by varying their size for the different output paths. Also, one practical limitation of the current demonstration is that the output grating couplers were not designed to accommodate an output fiber array. This resulted in inefficient measurement procedures and some output power variance due to alignment errors. Aligning the output grating couplers with a standard fiber array spacing will improve this and ease the electrical connection in a full transmitter demonstration.

Other important issues are OBFN insertion loss and thermal crosstalk amongst the tuning elements. In order to enable the monitor based tuning approach, 5$\%$ coupled drop port monitors are added in the OBFN structure. This increases the round trip loss of each ring resonator by an additional 0.2dB. Implementing transparent detectors, such as a contactless integrated photonic probe

(CLIPP) [36], can potentially remove this penalty. Thermal crosstalk between the heaters limited OBFN calibration time and resulted in complex tuning steps. Reduction in this thermal crosstalk is possible with more thermally-efficient heater designs utilizing graphene [116], tungsten[85], chromium [117], and resistive heaters directly doped on the waveguide [118, 85]. Also, optimizing the size and shape of the heaters, placing thermal isolation [89], or employing compact cooler packaging (μ-TEC) [86] can provide further improvements.

5.6 Conclusion

This paper has presented an automatic monitor-based calibration scheme for a silicon photonic ORR-based asymmetric binary tree OBFN. Utilizing electrical information obtained from monitor photodetectors at the ORRs' drop ports, the proposed tuning algorithm compensates fabrication variations and thermal crosstalk by controlling individual micro-heaters. Successfully calibration of a 1X4 OBFN from a severely degraded initial response to the well-defined group delay responses required for a targeted radiating angle over 60°in a linear beamforming antenna array is achieved. Overall, leveraging the proposed automatic calibration scheme can allow for robust operation of OBFNs in future wideband wireless communication systems.

6. CONCLUSIONS

6.1 Future works

6.2 Conclusions

To support exponentially increasing future mobile traffic, some of the disruptive technologies are necessary. Microwave photnoic technology can be used to help meet these goals. And emergence of silicon photonic technology makes possible to integrate microwave photonic technology in a small form factors. It is clear that silicon photonics may help realize the archiectures required to make the next-generation 5G network a reality.

The first part to the dissertation presented an automatic monitor-based filter calibration and reconfiguration scheme for silicon photonic APF-based pole/zero filters. To automate the calibration of the filter, drop port monitors with PD are added to the ring resonators. Utilizing electrical information obtained from monitor photodetectors, the proposed tuning algorithm controls thermal phase shifters. As a result of the calibration, severely degraded initial responses of both 2nd- and 4th-order elliptic filters are calibrated to the designed filter responses. The information extracted during this initial calibration enables reconfiguration of bandwidth and center frequency. During the automatic tuning thermal crosstalk issue severely dragged its performance interms of tuning time. PIC substrate thinning is shown to dramatically reduce thermal crosstalk between the phase shifter heaters and allow for faster filter tuning times. Overall, leveraging the proposed automatic photonic filter calibration scheme can allow for robust operation of silicon photonic filters in future wideband communication systems.

The second part of the dissertation presented an automatic monitor-based calibration for a silicon photonic ORR-based asymmetric binary tree OBFN. Utilizing electrical information obtained from monitor photodetectors are applied to this structure also. Unlike the filter tuning, beamforming network utilizes drop port monitor response to tune the group delay response at the output. As a result , severely degraded initial group delay response is calibrated using the proposed tuning algorithm, which ccontrols thermal phase shifters in the structure. Through the proposed calibration algorithm, fabrication variations and thermal crosstalk are compensated and well-defined full 1X4 calibrated output responses are demonstrated. Leveraging the proposed automatic OBFN calibration can allow for robust operation of OBFN in future wideband wireless communication systems.

REFERENCES

[1] P. K. Agyapong, M. Iwamura, D. Staehle, W. Kiess, and A. Benjebbour, “Design considerations for a 5g network architecture,” *IEEE Communications Magazine*, vol. 52, no. 11, pp. 65–75, 2014.

[2] M. Hochberg, N. C. Harris, R. Ding, Y. Zhang, A. Novack, Z. Xuan, and T. Baehr-Jones, “Silicon photonics: the next fabless semiconductor industry,” *IEEE Solid-State Circuits Magazine*, vol. 5, no. 1, pp. 48–58, 2013.

[3] J. M.Shea, “History of wireless communication: From the birth of telecommunications to the modern era of cellular communications and wireless local area networks,” December 2011. .

[4] J. Agrqwal, R. Patel, P. Mor, P. Dubey, and J. Keller, “Evolution of mobile communication network: From 1g to 4g,” *International Journal of Multidisciplinary and Current Research*, vol. 3, pp. 1100–1103, 2015.

[5] A. Ghosh, T. A. Thomas, M. C. Cudak, R. Ratasuk, P. Moorut, F. W. Vook, T. S. Rappaport, G. R. MacCartney, S. Sun, and S. Nie, “Millimeter-wave enhanced local area systems: A high-data-rate approach for future wireless networks,” *IEEE Journal on Selected Areas in Communications*, vol. 32, no. 6, pp. 1152–1163, 2014.

[6] R. Waterhouse and D. Novack, “Realizing 5g: microwave photonics for 5g mobile wireless systems,” *IEEE Microwave Magazine*, vol. 16, no. 8, pp. 84–92, 2015.

[7] K. C. Amy Nordrum and I. S. Staff, “Everything you need to know about 5g: Millimeter waves, massive mimo, full duplex, beamforming, and small cells are just a few of the technologies that could enable ultrafast 5g networks,” January 2017. .

[8] J. Yao, “Microwave photonics,” *Journal of Lightwave Technology*, vol. 27, pp. 314–335, Feb 2009.

[9] N. Dahad, "Radio over fiber paves way for future 5g networks," April 2018. .

[10] C. Liu, J. Wang, L. Cheng, M. Zhu, and G.-K. Chang, "Key microwave-photonics technologies for next-generation cloud-based radio access networks," *Journal of Lightwave Technology*, vol. 32, no. 20, pp. 3452–3460, 2014.

[11] B. Lannoo, A. Dixit, D. Colle, J. Bauwelinck, B. Dhoedt, B. Jooris, I. Moerman, M. Pickavet, H. Rogier, P. Simoens, *et al.*, "Radio-over-fibre for ultra-small 5g cells," in *Transparent Optical Networks (ICTON), 2015 17th International Conference on*, pp. 1–4, IEEE, 2015.

[12] L. Goldberg, H. Taylor, J. Weller, and D. Bloom, "Microwave signal generation with injection-locked laser diodes," *Electronics Letters*, vol. 19, no. 13, pp. 491–493, 1983.

[13] L. Goldberg, A. Yurek, H. Taylor, and J. Weller, "35 ghz microwave signal generation with an injection-locked laser diode," *Electronics Letters*, vol. 21, no. 18, pp. 814–815, 1985.

[14] R. Ramos and A. Seeds, "Fast heterodyne optical phase-lock loop using double quantum well laser diodes," *Electronics letters*, vol. 28, no. 1, pp. 82–83, 1992.

[15] A. Bordonalli, C. Walton, and A. J. Seeds, "High-performance phase locking of wide linewidth semiconductor lasers by combined use of optical injection locking and optical phase-lock loop," *Journal of Lightwave Technology*, vol. 17, no. 2, pp. 328–342, 1999.

[16] H. R. Rideout, J. S. Seregelyi, S. Paquet, and J. Yao, "Discriminator-aided optical phase-lock loop incorporating a frequency down-conversion module," *IEEE Photonics Technology Letters*, vol. 18, no. 22, pp. 2344–2346, 2006.

[17] J. O'reilly, P. Lane, R. Heidemann, and R. Hofstetter, "Optical generation of very narrow linewidth millimetre wave signals," *Electronics Letters*, vol. 28, no. 25, pp. 2309–2311, 1992.

[18] P. Shen, N. J. Gomes, P. A. Davies, W. P. Shillue, P. G. Huggard, and B. N. Ellison, "High-purity millimetre-wave photonic local oscillator generation and delivery," in *Microwave Photonics, 2003. MWP 2003 Proceedings. International Topical Meeting on*, pp. 189–192, IEEE, 2003.

[19] X. Chen, Z. Deng, and J. Yao, “Photonic generation of microwave signal using a dual-wavelength single-longitudinal-mode fiber ring laser,” *IEEE transactions on microwave theory and techniques*, vol. 54, no. 2, pp. 804–809, 2006.

[20] J. Capmany, J. Mora, I. Gasulla, J. Sancho, J. Lloret, and S. Sales, “Microwave photonic signal processing,” *Journal of Lightwave Technology*, vol. 31, no. 4, pp. 571–586, 2013.

[21] J. S. Fandiño, P. Muñoz, D. Doménech, and J. Capmany, “A monolithic integrated photonic microwave filter,” *Nature Photonics*, vol. 11, no. 2, p. 124, 2017.

[22] J. Capmany, B. Ortega, and D. Pastor, “A tutorial on microwave photonic filters,” *Journal of Lightwave Technology*, vol. 24, no. 1, p. 201, 2006.

[23] R. Soref, “The past, present, and future of silicon photonics,” *IEEE Journal of selected topics in quantum electronics*, vol. 12, no. 6, pp. 1678–1687, 2006.

[24] B. Jalali and S. Fathpour, “Silicon photonics,” *Journal of lightwave technology*, vol. 24, no. 12, pp. 4600–4615, 2006.

[25] D. A. Miller, “Optical interconnects to silicon,” *IEEE Journal of Selected Topics in Quantum Electronics*, vol. 6, no. 6, pp. 1312–1317, 2000.

[26] Z. Li, I. Shubin, and X. Zhou, “Optical interconnects: recent advances and future challenges,” *Optics express*, vol. 23, no. 3, pp. 3717–3720, 2015.

[27] D. Marpaung, C. Roeloffzen, R. Heideman, A. Leinse, S. Sales, and J. Capmany, “Integrated microwave photonics,” *Laser & Photonics Reviews*, vol. 7, no. 4, pp. 506–538, 2013.

[28] J. S. Rodgers, “Technologies for rf photonics in wideband multifunction systems,” in *Avionics, Fiber-Optics and Photonics Conference (AVFOP), 2013 IEEE*, pp. 7–8, IEEE, 2013.

[29] S. Pappert and B. Krantz, “Rf photonics for radar front-ends,” in *Radar Conference, 2007 IEEE*, pp. 965–970, IEEE, 2007.

[30] A. Safarian, A. Shameli, A. Rofougaran, M. Rofougaran, and F. De Flaviis, "Integrated blocker filtering rf front ends," in *Radio Frequency Integrated Circuits (RFIC) Symposium, 2007 IEEE*, pp. 13–16, IEEE, 2007.

[31] K. Entesari and G. M. Rebeiz, "A 12-18-ghz three-pole rf mems tunable filter," *IEEE Transactions on microwave theory and techniques*, vol. 53, no. 8, pp. 2566–2571, 2005.

[32] K. Entesari and G. M. Rebeiz, "A differential 4-bit 6.5-10-ghz rf mems tunable filter," *IEEE transactions on microwave theory and techniques*, vol. 53, no. 3, pp. 1103–1110, 2005.

[33] F. Dulger, E. Sanchez-Sinencio, and J. Silva-Martinez, "A 1.3-v 5-mw fully integrated tunable bandpass filter at 2.1 ghz in 0.35-/spl mu/m cmos," *IEEE Journal of Solid-State Circuits*, vol. 38, no. 6, pp. 918–928, 2003.

[34] Y. Wu, X. Ding, M. Ismail, and H. Olsson, "Rf bandpass filter design based on cmos active inductors," *IEEE Transactions on Circuits and Systems II: Analog and Digital Signal Processing*, vol. 50, no. 12, pp. 942–949, 2003.

[35] H. Darabi, "A blocker filtering technique for saw-less wireless receivers," *IEEE Journal of Solid-State Circuits*, vol. 42, no. 12, pp. 2766–2773, 2007.

[36] A. Balankutty and P. R. Kinget, "An ultra-low voltage, low-noise, high linearity 900-mhz receiver with digitally calibrated in-band feed-forward interferer cancellation in 65-nm cmos," *IEEE Journal of Solid-State Circuits*, vol. 46, no. 10, pp. 2268–2283, 2011.

[37] Z. Ru, N. A. Moseley, E. A. Klumperink, and B. Nauta, "Digitally enhanced software-defined radio receiver robust to out-of-band interference," *IEEE journal of solid-state circuits*, vol. 44, no. 12, pp. 3359–3375, 2009.

[38] A. Balankutty, S.-A. Yu, Y. Feng, and P. R. Kinget, "A 0.6-v zero-if/low-if receiver with integrated fractional-n synthesizer for 2.4-ghz ism-band applications," *IEEE Journal of Solid-State Circuits*, vol. 45, no. 3, pp. 538–553, 2010.

[39] M. E. Manka, “Microwave photonics for electronic warfare applications,” in *Microwave photonics, 2008. jointly held with the 2008 asia-pacific microwave photonics conference. mwp/apmp 2008. international topical meeting on*, pp. 275–278, IEEE, 2008.

[40] M. S. Rasras, K.-Y. Tu, D. M. Gill, Y.-K. Chen, A. E. White, S. S. Patel, A. Pomerene, D. Carothers, J. Beattie, M. Beals, *et al.*, “Demonstration of a tunable microwave-photonic notch filter using low-loss silicon ring resonators,” *Journal of Lightwave Technology*, vol. 27, no. 12, pp. 2105–2110, 2009.

[41] B. Guan, S. S. Djordjevic, N. K. Fontaine, L. Zhou, S. Ibrahim, R. P. Scott, D. J. Geisler, Z. Ding, and S. B. Yoo, “Cmos compatible reconfigurable silicon photonic lattice filters using cascaded unit cells for rf-photonic processing,” *IEEE Journal of Selected Topics in Quantum Electronics*, vol. 20, no. 4, pp. 359–368, 2014.

[42] K.-Y. Tu, M. S. Rasras, D. M. Gill, S. S. Patel, Y.-K. Chen, A. E. White, A. Pomerene, D. Carothers, J. Beattie, M. Beals, *et al.*, “Silicon rf-photonic filter and down-converter,” *Journal of Lightwave Technology*, vol. 28, no. 20, pp. 3019–3028, 2010.

[43] S. Onoe, “1.3 evolution of 5g mobile technology toward 1 2020 and beyond,” in *Solid-State Circuits Conference (ISSCC), 2016 IEEE International*, pp. 23–28, IEEE, 2016.

[44] Z. Pi and F. Khan, “An introduction to millimeter-wave mobile broadband systems,” *IEEE communications magazine*, vol. 49, no. 6, 2011.

[45] T. S. Rappaport, S. Sun, R. Mayzus, H. Zhao, Y. Azar, K. Wang, G. N. Wong, J. K. Schulz, M. Samimi, and F. Gutierrez, “Millimeter wave mobile communications for 5g cellular: It will work!,” *IEEE access*, vol. 1, pp. 335–349, 2013.

[46] S. Rangan, T. S. Rappaport, and E. Erkip, “Millimeter-wave cellular wireless networks: Potentials and challenges,” *Proceedings of the IEEE*, vol. 102, no. 3, pp. 366–385, 2014.

[47] W. Roh, J.-Y. Seol, J. Park, B. Lee, J. Lee, Y. Kim, J. Cho, K. Cheun, and F. Aryanfar, “Millimeter-wave beamforming as an enabling technology for 5g cellular communications:

Theoretical feasibility and prototype results," *IEEE communications magazine*, vol. 52, no. 2, pp. 106–113, 2014.

[48] F. Aryanfar, J. Pi, H. Zhou, T. Henige, G. Xu, S. Abu-Surra, D. Psychoudakis, and F. Khan, "Millimeter-wave base station for mobile broadband communication," in *Microwave Symposium (IMS), 2015 IEEE MTT-S International*, pp. 1–3, IEEE, 2015.

[49] A. Meijerink, C. G. Roeloffzen, R. Meijerink, L. Zhuang, D. A. Marpaung, M. J. Bentum, M. Burla, J. Verpoorte, P. Jorna, A. Hulzinga, *et al.*, "Novel ring resonator-based integrated photonic beamformer for broadband phased array receive antennasâĂŤpart i: Design and performance analysis," *Journal of Lightwave Technology*, vol. 28, no. 1, pp. 3–18, 2010.

[50] L. Zhuang, C. G. Roeloffzen, A. Meijerink, M. Burla, D. A. Marpaung, A. Leinse, M. Hoekman, R. G. Heideman, and W. van Etten, "Novel ring resonator-based integrated photonic beamformer for broadband phased array receive antennasâĂŤpart ii: Experimental prototype," *Journal of lightwave technology*, vol. 28, no. 1, pp. 19–31, 2010.

[51] K.-J. Koh and G. M. Rebeiz, "An x-and ku-band 8-element phased-array receiver in 0.18um sige bicmos technology," *IEEE Journal of Solid-State Circuits*, vol. 43, no. 6, pp. 1360–1371, 2008.

[52] M. Boers, B. Afshar, I. Vassiliou, S. Sarkar, S. T. Nicolson, E. Adabi, B. G. Perumana, T. Chalvatzis, S. Kavvadias, P. Sen, *et al.*, "A 16tx/16rx 60 ghz 802.11 ad chipset with single coaxial interface and polarization diversity," *IEEE journal of solid-state circuits*, vol. 49, no. 12, pp. 3031–3045, 2014.

[53] A. Natarajan, S. K. Reynolds, M.-D. Tsai, S. T. Nicolson, J.-H. C. Zhan, D. G. Kam, D. Liu, Y.-L. O. Huang, A. Valdes-Garcia, and B. A. Floyd, "A fully-integrated 16-element phased-array receiver in sige bicmos for 60-ghz communications," *IEEE Journal of Solid-State Circuits*, vol. 46, no. 5, pp. 1059–1075, 2011.

[54] S. Zihir, O. Gurbuz, A. Karroy, S. Raman, and G. Rebeiz, "A 60 ghz 64-element wafer-scale phased-array with full-reticle design," in *Microwave Symposium (IMS), 2015 IEEE MTT-S*

International, pp. 1–3, IEEE, 2015.

[55] H. Hashemi, X. Guan, A. Komijani, and A. Hajimiri, "A 24-ghz sige phased-array receiver-lo phase-shifting approach," *IEEE Transactions on Microwave Theory and Techniques*, vol. 53, no. 2, pp. 614–626, 2005.

[56] S. Kundu and J. Paramesh, "A compact, supply-voltage scalable 45–66 ghz baseband-combining cmos phased-array receiver," *IEEE Journal of Solid-State Circuits*, vol. 50, no. 2, pp. 527–542, 2015.

[57] S. Zihir and G. M. Rebeiz, "A 60 ghz 64-element phased-array beam-pointing communication system for 5g 100 meter links up to 2 gbps," in *Microwave Symposium (IMS), 2016 IEEE MTT-S International*, pp. 1–3, IEEE, 2016.

[58] R. Soref, "Optical dispersion technique for time-delay beam steering," *Applied optics*, vol. 31, no. 35, pp. 7395–7397, 1992.

[59] H. Zmuda, R. A. Soref, P. Payson, S. Johns, and E. N. Toughlian, "Photonic beamformer for phased array antennas using a fiber grating prism," *IEEE Photonics Technology Letters*, vol. 9, no. 2, pp. 241–243, 1997.

[60] J. Corral, J. Marti, J. Fuster, and R. Laming, "Dispersion-induced bandwidth limitation of variable true time delay lines based on linearly chirped fibre gratings," *Electronics Letters*, vol. 34, no. 2, pp. 209–211, 1998.

[61] M. A. Piqueras, G. Grosskopf, B. Vidal, J. Herrera, J. M. Martínez, P. Sanchis, V. Polo, J. L. Corral, A. Marceaux, J. Galière, *et al.*, "Optically beamformed beam-switched adaptive antennas for fixed and mobile broad-band wireless access networks," *IEEE Transactions on Microwave Theory and Techniques*, vol. 54, no. 2, pp. 887–899, 2006.

[62] S. Shakib, H.-C. Park, J. Dunworth, V. Aparin, and K. Entesari, "A highly efficient and linear power amplifier for 28-ghz 5g phased array radios in 28-nm cmos," *IEEE Journal of Solid-State Circuits*, vol. 51, no. 12, pp. 3020–3036, 2016.

[63] C. K. Madsen and J. H. Zhao, *Frontmatter and Index.* Wiley Online Library, 1999.

[64] M. Piels and J. E. Bowers, "Department of electrical and computer engineering, university of california santa barbara, santa barbara, ca, usa," 2016.

[65] G. Choo, S. Cai, B. Wang, C. K. Madsen, K. Entesari, and S. Palermo, "Automatic monitor-based tuning of reconfigurable silicon photonic apf-based pole/zero filters," *Journal of Lightwave Technology*, vol. PP, no. 99, pp. 1–1, 2018.

[66] G. Choo, C. Madsen, K. Entesari, and S. Palermo, "A reconfigurable silicon photonic 4 th-order filter for synthesizing butterworth, chebyshev, and elliptic responses," in *Avionics and Vehicle Fiber-Optics and Photonics Conference (AVFOP), 2017 IEEE*, pp. 15–16, IEEE, 2017.

[67] G. Choo, S. Cai, B. Wang, C. Madsen, K. Entesari, and S. Palermo, "Automatic monitor-based tuning of reconfigurable silicon photonic 2 nd-order apf-based pole/zero filters," in *CLEO: Science and Innovations*, pp. SF1H–3, Optical Society of America, 2017.

[68] S. Cai, G. Choo, B. Wang, K. Entesari, and S. Palermo, "Comprehensive adaptive tuning of silicon rf photonic filters," in *Wiireless and Microwave Circuits and Systems (WMCS), 2016 Texas Symposium on*, pp. 1–4, IEEE, 2016.

[69] P. Orlandi, F. Morichetti, M. J. Strain, M. Sorel, P. Bassi, and A. Melloni, "Photonic integrated filter with widely tunable bandwidth," *Journal of Lightwave Technology*, vol. 32, no. 5, pp. 897–907, 2014.

[70] E. J. Norberg, R. S. Guzzon, J. S. Parker, L. A. Johansson, and L. A. Coldren, "Programmable photonic microwave filters monolithically integrated in inp–ingaasp," *Journal of Lightwave Technology*, vol. 29, no. 11, pp. 1611–1619, 2011.

[71] K. Jinguji, "Synthesis of coherent two-port optical delay-line circuit with ring waveguides," *Journal of Lightwave Technology*, vol. 14, no. 8, pp. 1882–1898, 1996.

[72] M. J. Strain, S. Thoms, D. S. MacIntyre, and M. Sorel, "Multi-wavelength filters in silicon using superposition sidewall bragg grating devices," *Optics letters*, vol. 39, no. 2, pp. 413–416, 2014.

[73] A. Vorckel, M. Monster, W. Henschel, P. H. Bolivar, and H. Kurz, “Asymmetrically coupled silicon-on-insulator microring resonators for compact add-drop multiplexers,” *IEEE Photonics Technology Letters*, vol. 15, no. 7, pp. 921–923, 2003.

[74] J. Palací, G. E. Villanueva, J. V. Galán, J. Martí, and B. Vidal, “Single bandpass photonic microwave filter based on a notch ring resonator,” *IEEE Photonics Technology Letters*, vol. 22, no. 17, pp. 1276–1278, 2010.

[75] J. C. Mak, W. D. Sacher, T. Xue, J. C. Mikkelsen, Z. Yong, and J. K. Poon, “Automatic resonance alignment of high-order microring filters,” *IEEE Journal of Quantum Electronics*, vol. 51, no. 11, pp. 1–11, 2015.

[76] J. C. Mak, A. Bois, and J. K. Poon, “Programmable multiring butterworth filters with automated resonance and coupling tuning,” *IEEE Journal of Selected Topics in Quantum Electronics*, vol. 22, no. 6, pp. 232–240, 2016.

[77] Q. Li, A. A. Eftekhar, P. Alipour, A. H. Atabaki, S. Yegnanarayanan, and A. Adibi, “Low-loss microdisk-based delay lines for narrowband optical filters,” *IEEE Photonics Technology Letters*, vol. 24, no. 15, pp. 1276–1278, 2012.

[78] S. Ibrahim, N. K. Fontaine, S. S. Djordjevic, B. Guan, T. Su, S. Cheung, R. P. Scott, A. T. Pomerene, L. L. Seaford, C. M. Hill, *et al.*, “Demonstration of a fast-reconfigurable silicon cmos optical lattice filter,” *Optics express*, vol. 19, no. 14, pp. 13245–13256, 2011.

[79] C. Madsen, “Efficient architectures for exactly realizing optical filters with optimum bandpass designs,” *IEEE Photonics technology letters*, vol. 10, no. 8, pp. 1136–1138, 1998.

[80] M. S. Rasras, D. M. Gill, S. S. Patel, K.-Y. Tu, Y.-K. Chen, A. E. White, A. T. Pomerene, D. N. Carothers, M. J. Grove, D. K. Sparacin, *et al.*, “Demonstration of a fourth-order pole-zero optical filter integrated using cmos processes,” *Journal of Lightwave Technology*, vol. 25, no. 1, pp. 87–92, 2007.

[81] K. Takada, M. Abe, T. Shibata, and K. Okamoto, "1-ghz-spaced 16-channel arrayed-waveguide grating for a wavelength reference standard in dwdm network systems," *Journal of lightwave technology*, vol. 20, no. 5, p. 822, 2002.

[82] N. C. Harris, Y. Ma, J. Mower, T. Baehr-Jones, D. Englund, M. Hochberg, and C. Galland, "Efficient, compact and low loss thermo-optic phase shifter in silicon," *Optics express*, vol. 22, no. 9, pp. 10487–10493, 2014.

[83] J. Kim, W. J. Sung, O. Eknoyan, and C. K. Madsen, "Linear photonic frequency discriminator on as 2 s 3-ring-on-ti: Linbo 3 hybrid platform," *Optics Express*, vol. 21, no. 21, pp. 24566–24573, 2013.

[84] M. R. Watts, J. Sun, C. DeRose, D. C. Trotter, R. W. Young, and G. N. Nielson, "Adiabatic thermo-optic mach–zehnder switch," *Optics letters*, vol. 38, no. 5, pp. 733–735, 2013.

[85] A. Masood, M. Pantouvaki, G. Lepage, P. Verheyen, J. Van Campenhout, P. Absil, D. Van Thourhout, and W. Bogaerts, "Comparison of heater architectures for thermal control of silicon photonic circuits," in *Group IV Photonics (GFP), 2013 IEEE 10th International Conference on*, pp. 83–84, IEEE, 2013.

[86] R. Enright, S. Lei, G. Cunningham, I. Mathews, R. Frizzell, and A. Shen, "Integrated thermoelectric cooling for silicon photonics," *ECS Journal of Solid State Science and Technology*, vol. 6, no. 3, pp. N3103–N3112, 2017.

[87] S. Liao, Y. Ding, C. Peucheret, T. Yang, J. Dong, and X. Zhang, "Integrated programmable photonic filter on the silicon-on-insulator platform," *Optics Express*, vol. 22, no. 26, pp. 31993–31998, 2014.

[88] F. Morichetti, S. Grillanda, M. Carminati, G. Ferrari, M. Sampietro, M. J. Strain, M. Sorel, and A. Melloni, "Non-invasive on-chip light observation by contactless waveguide conductivity monitoring," *IEEE Journal of Selected Topics in Quantum Electronics*, vol. 20, no. 4, pp. 292–301, 2014.

[89] P. Dong, W. Qian, H. Liang, R. Shafiiha, N.-N. Feng, D. Feng, X. Zheng, A. V. Krishnamoorthy, and M. Asghari, "Low power and compact reconfigurable multiplexing devices based on silicon microring resonators," *Optics express*, vol. 18, no. 10, pp. 9852–9858, 2010.

[90] M. Asheghi, M. Touzelbaev, K. Goodson, Y. Leung, and S. Wong, "Temperature-dependent thermal conductivity of single-crystal silicon layers in soi substrates," *Journal of Heat Transfer*, vol. 120, no. 1, pp. 30–36, 1998.

[91] D. Jenn, Y. Loke, M. Tong, E. C. Yeo, and R. Broadston, "Distributed phased arrays with wireless beamforming," in *Signals, Systems and Computers, 2007. ACSSC 2007. Conference Record of the Forty-First Asilomar Conference on*, pp. 948–952, IEEE, 2007.

[92] D.-W. Kang, J.-G. Kim, B.-W. Min, and G. M. Rebeiz, "Single and four-element ka-band transmit/receive phased-array silicon rfics with 5-bit amplitude and phase control," *IEEE Transactions on Microwave Theory and Techniques*, vol. 57, no. 12, pp. 3534–3543, 2009.

[93] J. Capmany and D. Novak, "Microwave photonics combines two worlds," *Nature photonics*, vol. 1, no. 6, p. 319, 2007.

[94] J. Yao, "Microwave photonics," *Journal of Lightwave Technology*, vol. 27, no. 3, pp. 314–335, 2009.

[95] W. Ng, A. A. Walston, G. L. Tangonan, J. J. Lee, I. L. Newberg, and N. Bernstein, "The first demonstration of an optically steered microwave phased array antenna using true-time-delay," *Journal of Lightwave Technology*, vol. 9, no. 9, pp. 1124–1131, 1991.

[96] R. D. Esman, M. Frankel, J. Dexter, L. Goldberg, M. Parent, D. Stilwell, and D. Cooper, "Fiber-optic prism true time-delay antenna feed," *IEEE Photonics Technology Letters*, vol. 5, no. 11, pp. 1347–1349, 1993.

[97] A. Molony, C. Edge, and I. Bennion, "Fibre grating time delay element for phased array antennas," *Electronics Letters*, vol. 31, no. 17, pp. 1485–1486, 1995.

[98] J. Roman, M. Frankel, P. Matthews, and R. Esman, "Time-steered array with a chirped grating beamformer," *Electronics Letters*, vol. 33, no. 8, pp. 652–653, 1997.

[99] B. Howley, X. Wang, M. Chen, and R. T. Chen, "Reconfigurable delay time polymer planar lightwave circuit for an x-band phased-array antenna demonstration," *Journal of Lightwave Technology*, vol. 25, no. 3, pp. 883–890, 2007.

[100] W. Ng, D. Yap, A. Narayanan, and A. Walston, "High-precision detector-switched monolithic gaas time-delay network for the optical control of phased arrays," *IEEE photonics technology letters*, vol. 6, no. 2, pp. 231–234, 1994.

[101] I. O. Kohji Horikawa and H. O. Tsutomu Kitoh, "Silica-based integrated planar lightwave true-time-delay network for microwave antenna applications," in *Optical Fiber Communication Conference*, p. WB4, Optical Society of America, 1996.

[102] F. Xia, L. Sekaric, and Y. Vlasov, "Ultracompact optical buffers on a silicon chip," *Nature photonics*, vol. 1, no. 1, p. 65, 2007.

[103] J. Cardenas, M. A. Foster, N. Sherwood-Droz, C. B. Poitras, H. L. Lira, B. Zhang, A. L. Gaeta, J. B. Khurgin, P. Morton, and M. Lipson, "Wide-bandwidth continuously tunable optical delay line using silicon microring resonators," *Optics express*, vol. 18, no. 25, pp. 26525–26534, 2010.

[104] J. Xie, L. Zhou, Z. Zou, J. Wang, X. Li, and J. Chen, "Continuously tunable reflective-type optical delay lines using microring resonators," *Optics express*, vol. 22, no. 1, pp. 817–823, 2014.

[105] N. Tessema, Z. Cao, J. V. Zantvoort, A. Dubok, E. Tangdiongga, B. Smolders, and T. Koonen, "Radio beam-steering via tunable si 3 n 4 optical delays for multi-gbps k-band satellite communication," in *Optical Fiber Communication Conference*, pp. W3K–4, Optical Society of America, 2016.

[106] Y. Liu, A. Wichman, B. Isaac, J. Kalkavage, E. J. Adles, T. R. Clark, and J. Klamkin, "Tuning optimization of ring resonator delays for integrated optical beam forming networks," *Journal of Lightwave Technology*, vol. 35, pp. 4954–4960, Nov 2017.

[107] X. Wang, L. Zhou, R. Li, J. Xie, L. Lu, and J. Chen, "Nanosecond-range continuously tunable silicon optical delay line using ultra-thin silicon waveguides," in *Lasers and Electro-Optics (CLEO), 2016 Conference on*, pp. 1–2, IEEE, 2016.

[108] G. Choo, C. Madsen, S. Palermo, and K. Entesari, "Automatic monitor-based tuning of rf silicon photonic true-time-delay beamforming networks," in *IMS*, pp. TH1E–4, IEEE, 2018.

[109] O. Schwelb, "Transmission, group delay, and dispersion in single-ring optical resonators and add/drop filters-a tutorial overview," *Journal of Lightwave Technology*, vol. 22, no. 5, pp. 1380–1394, 2004.

[110] G. Lenz, B. Eggleton, C. K. Madsen, and R. Slusher, "Optical delay lines based on optical filters," *IEEE Journal of Quantum Electronics*, vol. 37, no. 4, pp. 525–532, 2001.

[111] R. Blokpoel, A. Meijerink, L. Zhuang, C. Roeloffzen, and W. van Etten, "Staggered delay tuning algorithms for ring resonators in optical beam forming networks," in *Proc. 12th IEEE/LEOS Symp. Benelux*, pp. 243–246, 2007.

[112] O. Bakr and M. Johnson, "Impact of phase and amplitude errors on array performance," *EECS Department, University of California, Berkeley, Tech. Rep. UCB/EECS-2009-1*, 2009.

[113] M. Burla, "Advanced integrated optical beam forming networks for broadband phased array antenna systems," 2013.

[114] L. Inovations, "Calculating group delay and chromatic dispersion from ova optical phase."

[115] R. L. Moreira, J. Garcia, W. Li, J. Bauters, J. S. Barton, M. J. Heck, J. E. Bowers, and D. J. Blumenthal, "Integrated ultra-low-loss 4-bit tunable delay for broadband phased array antenna applications," *IEEE Photon. Technol. Lett*, vol. 25, no. 12, pp. 1165–1168, 2013.

[116] D. Schall, M. Mohsin, A. A. Sagade, M. Otto, B. Chmielak, S. Suckow, A. L. Giesecke, D. Neumaier, and H. Kurz, "Infrared transparent graphene heater for silicon photonic integrated circuits," *Optics express*, vol. 24, no. 8, pp. 7871–7878, 2016.

[117] R. Amatya, C. W. Holzwarth, M. A. Popovic, F. Gan, H. I. Smith, F. Kartner, and R. J. Ram, "Low power thermal tuning of second-order microring resonators," in *2007 Conference on Lasers and Electro-Optics (CLEO)*, pp. 1–2, May 2007.

[118] J. E. Cunningham, I. Shubin, X. Zheng, T. Pinguet, A. Mekis, Y. Luo, H. Thacker, G. Li, J. Yao, K. Raj, and A. V. Krishnamoorthy, "Highly-efficient thermally-tuned resonant optical filters," *Opt. Express*, vol. 18, pp. 19055–19063, Aug 2010.